TESIS DE LA UNIVERSIDAD DE ZARAGOZA

2012

80

Edna Consuelo Corredor Vega

Preparation and characterization of epitaxial thin films and patterned nanostructures of Ni/Cu and Fe/Cu

Departamento

Física de la Materia Condensada

Director/es

Ciria Remacha, Miguel Angel

Arnaudas Pontaque, José Ignacio

ISSN 2254-7606

Prensas de la Universidad Universidad Zaragoza

Universidad Zaragoza
1542

Tesis Doctoral

PREPARATION AND CHARACTERIZATION OF EPITAXIAL THIN FILMS AND PATTERNED NANOSTRUCTURES OF NI/CU AND FE/CU

Autor

Edna Consuelo Corredor Vega

Director/es

Ciria Remacha, Miguel Angel
Arnaudas Pontaque, José Ignacio

UNIVERSIDAD DE ZARAGOZA

Física de la Materia Condensada

2012

Preparation and magnetic characterization of epitaxial thin films and patterned nanostructures of Ni/Cu and Fe/Cu

Thesis submitted for the Degree of Doctor in Physics.
University of Zaragoza, Spain (2012).

Author:

Edna Consuelo Corredor Vega

Advisors:

Dr. Miguel Ángel Ciria Remacha

Prof. Dr. José Ignacio Arnaudas

Preparation and magnetic characterization of epitaxial thin films and patterned nanostructures of Ni/Cu and Fe/Cu

Edna Consuelo Corredor Vega

Aragon Institute of Nanoscience and The Department of Condensed Matter Physics of the University of Zaragoza.

The Materials Science Institute of Aragon of the University of Zaragoza and the Spanish National Research Council.

Universidad Zaragoza

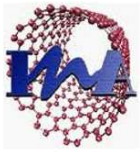

Instituto Universitario de Investigación
en Nanociencia de Aragón
Universidad Zaragoza

CSIC
Consejo Superior de Investigaciones Científicas

icma / Instituto de Ciencia de Materiales de Aragón

To my family.

Contents

I. Experimental Procedures 3

Growth of Ni/Cu thin films 3

Electron Beam Lithography (EBL) 8

References I 13

II. Perpendicular Anisotropy in Ni Multilayers 17

Introduction 17

X-ray characterization 18

Magnetic Properties 26

Discussion 32

Conclusions 33

Coercive force 34

Coercivity in thin films 37

Discussion 39

References II 45

III. Magnetic Domain Structure on a Fe Wedge 49

Introduction 49

Experimental Details 52

General features and magnetic contrast ($t_{Fe} < 4$ML) 53

Spin Reorientation Transition, Fe films ($t_{Fe} > 11$ ML) 57

Magnetoelastic Model 61

Conclusion 63

References III 65

IV. Struct. and Magn. Properties of Fe/Cu/Ni Films 69

Introduction 69

Growth and in-situ characterization 71

Ex-situ characterization 75

Magnetic Properties 79

Discussion 84

Conclusions 85

References IV 87

V. Transverse Magnetization in Ni rings 91

Introduction 91

Electron beam lithography 93

Magnetic Force Microscopy 95

Analysis 100

Discussion 105

Conclusions 107

References V 109

Chapter I

Experimental Procedures

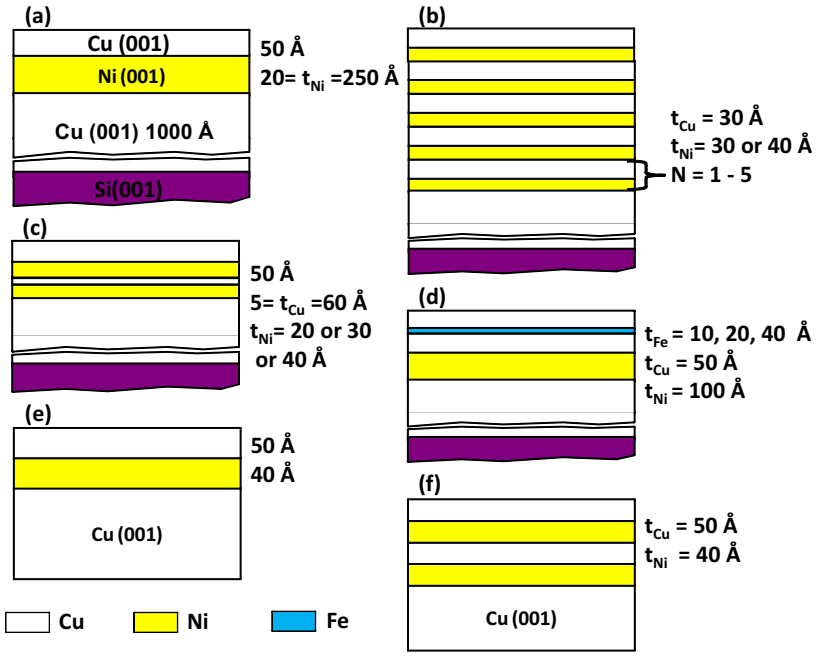

Figure 1: Schematic of Cu/Ni/Cu films grown by molecular beam epitaxy (MBE) along this thesis. Si(001) wafers and single crystals of Cu(001) substrates were used. A buffer layer of 1000 Å of Cu is always grown on the Si(001) substrate. (a) **[Cu(50Å)/Ni(t_{Ni})]** (20Å $\leq t_{Ni} \leq$ 250Å) films. (b) **[Ni(t_{Ni})/Cu(30Å)]x N** (t_{Ni} = 30 and 40 Å) multilayers with N = 1, 2, 3, 4, and 5 . (c) **[Cu(50Å)/Ni(t_{Ni})/Cu(t_{Cu})/Ni(t_{Ni})]** (t_{Ni}= 20, 30 and 40Å) (5Å $\leq t_{Cu} \leq$ 60Å) double Ni films. (d) **[Cu(50Å)/Fe(t_{Fe})/Cu(50Å)/Ni(100Å)]** (t_{Fe}= 10, 20 and 40 Å) films. (e) **[Cu(50Å)/Ni(40Å)]** films on Cu(001) single crystal. (f) **[Cu(50Å)/Ni(40Å)/Cu(30Å)/Ni(40Å)]** double Ni films on Cu(001) single crystal.

Growth of Ni/Cu thin films

Series of Cu(50Å)/Ni(t_{Ni})/Cu(1000Å)/Si(001)(20Å $\leq t_{Ni} \leq$ 250Å), Cu(50Å) /Ni(t_{Ni})/ Cu(t_{Cu}) /Ni(t_{Ni})/Cu(1000Å)/Si(001) (20Å $\leq t_{Ni} \leq$ 40Å) (5Å $\leq t_{Cu} \leq$ 60Å), [Ni(t_{Ni}) /Cu(30Å)]xN/Cu(1000Å)/Si(001) films, among others (see Fig. 1) were deposited by electron-beam evaporation in an ultra-high vacuum chamber. Film epitaxy was monitored by *in situ* reflection high energy electron

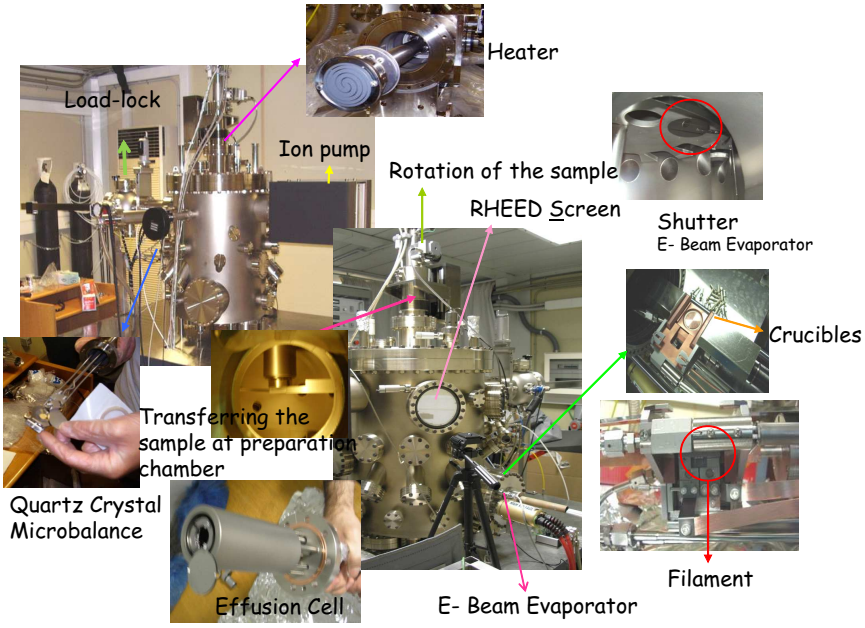

Figure 2: Photograph of the MBE equipment.

diffraction (RHEED). Film surface roughness was examined by RHEED and an *ex situ* x-ray reflectivity (XRR). The structural quality and the out-of-plane strain were measured using x-ray diffraction and high resolution transmission electron microscopy (HRTEM). TEM experiments were also used to study the type, spacing and orientation of dislocations by using plan-view and cross-sectional samples. The magnetic anisotropy of these films was characterized using a vibrating sample magnetometer(VSM).

Molecular Beam Epitaxy Deposition System

The Cu/Ni/Cu/Si(001) films were all deposited using a molecular beam epitaxy (MBE) M600 DCA system. The advent of MBE has made it possible to deposit high quality epitaxial films (i.e., high purity and crystallinity) in a controlled environment. The key factor of its success lies in the ultra-high vacuum (UHV) condition with base pressures less than 10^{-9} Torr. The good vacuum makes it possible for films to be grown at a slow rate, which is essential for obtaining good epitaxy (incoming atoms have sufficient time to migrate on the slow growing surface). Consequently, the surface of the grown film can be atomically smooth in many systems. Another advantage of MBE technique is many surface diagnostic tools (e.g., RHEED and Auger electron spectroscopy) that can be used *in situ* to study and characterize the growth. Thus, MBE is the method of choice for fabricating films whose structures must be tightly controlled. Therefore, the use of MBE for growing nickel epitaxial on Cu(001)

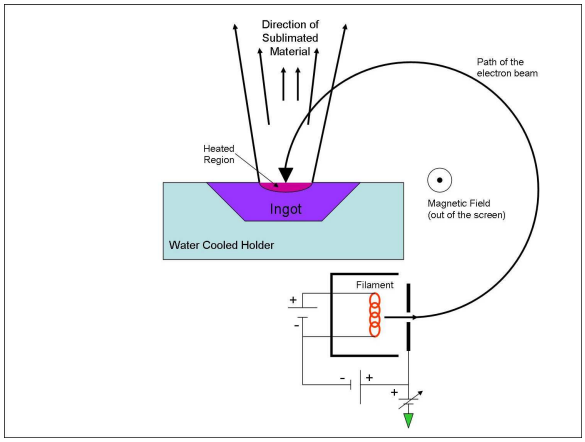

Figure 3: Diagram of a electron beam evaporation system where there is no direct line of sight from the filament to the material for evaporating. *Courtesy of Wikipedia.*

is important because it grows in an UHV environment where we can control with high precision the contamination level, rates of deposition and crystalline quality of the films during evaporation. Good epitaxy is essential for the observation of perpendicular magnetization in the nickel layer.

The vacuum in the main chamber is achieved by using a series of pumps, each of which has its own operative pressure range. The chamber is equipped with a load-lock provided with a Varian scroll pump and a Pfeiffer Vacuum turbo pump (60 l/s) that allows quickly reach pressure about 10^{-8} Torr. An ion pump (500 l/s) is then turned on to help bringing the pressure to about 10^{-9} after a few days of pumping. With a good bake (that is, the chamber is heated to about 150°C for a few days), the pressure of less than 5×10^{-10} Torr can be obtained.

Figure 2 shows a picture of the MBE system. The main chamber is equipped with a multi- pocket linear electron gun for four different materials (up to 6kW), two high temperature effusion cells, a RHEED set-up (15 keV), fast action linear shutters, a quartz crystal monitor thickness, sample heater up to 1000°C. During the Cu, Ni and Fe evaporations, the evaporation guns, the crystal monitor and the sample manipulator are water-cooled. The pressure does not rise above 10^{-8} Torr during the deposition of the films.

Figure 3 illustrates the evaporation process. Electron-beam evaporation makes use of a water-cooled crucible containing the desired metal, heated by an incoming beam of electrons from a tungsten filament. Typically the filament is located adjacent to the crucible, with the electron beam bent by magnetic fields to impinge upon the crucible contents, thus preventing evaporation of metal onto the filament itself.

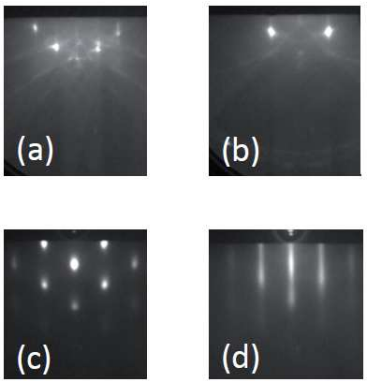

Figure 4: RHEED patterns obtained for the silicon with the electron beam along the (a) [100] and (b) [110] directions, and for the copper buffer layer along the [110] direction before (c) and after (d) the annealing process.

Substrate Preparation and Film Growth

Prior to the loading in the chamber, the Si(001) p-type substrate, which have 2 inches of diameter, are first dipped in a 10% hydrofluoric solution for twelve seconds and then rinsed with deionized water for above 20 seconds. This process removes the native silicon oxide and leaves the surface hydrogen passivated, which is inert for several minutes in air and several days in UHV at room temperature[1, 2]. The silicon wafers are then immediately transferred into the load-lock chamber to be pumped down.

After several hours in the load-lock, the substrate is transferred into the main chamber and heated at 150°C for 1 hour to eliminate the vapour of water that stay still on. Once the RHEED pattern shows sharp streaky diffraction lines and Kikuchi lines, which indicate a clean Si surface (see Fig. 4 (a) and (b)). Following these observations a Cu layer was evaporated at a rate of 0.5 /sec on the Si substrate at room temperature. The epitaxial relationships between the Si(001) and Cu were determined by *in-situ* RHEED observations and *ex-situ* with θ - 2 θ x-ray diffraction measurements. Comparing the lattice constants of Cu, 3.616 Å , and Si, 5.431 Å , a mismatch as large as 40% exists between the two. However, upon the rotation of 45° of the Cu (200) lattice, a much improved match is possible. This means a multiplication of the Cu lattice by a factor of $\sqrt{2}$, making it 5,113Å . Thus, the epitaxy of Cu (100) on the (100) Si, have been established with a 45° rotation.[3–6]. Then, the Cu [100] axis is parallel to the Si [110] axis.

The deposition rate and the final thickness of the films were monitored by a quartz crystal microbalance which was calibrated using x-ray reflectivity.

The copper buffer layers for all the samples were annealed *in situ* to about 120°C for 40 minutes and then cooled down to 20°C prior to the deposition

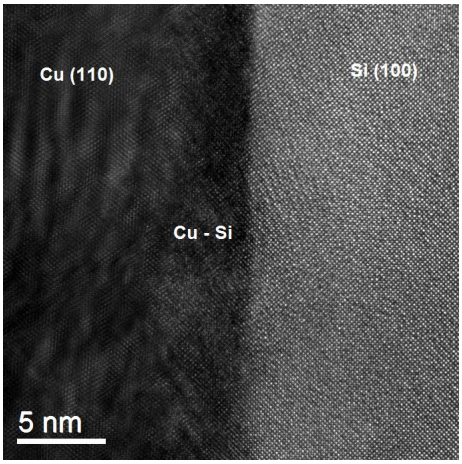

Figure 5: HRTEM image of the Si and Cu interface.

of the nickel layer. The annealing process improved the flatness of the buffer layer surface. Figure 4(c) shows the RHEED pattern of a 1000Å copper film on Si(001) before the anneal. The spottedness of the pattern indicates that the surface of the copper film was atomically rough. Figure 4(d) shows the RHEED pattern of the same film after the anneal. The streaky RHEED pattern suggests that the surface was atomically flat.

Additional HRTEM experiments have shown the formation of a ≈ 5 Å copper silicide layer at the Cu-Si interface (see Fig. 5). Previous studies have shown the copper-silicide forms slowly at room temperature after the epitaxial relationship between the Cu layers and Si substrate has been established since the Cu layer lying above the silicide remains a single crystal. [7, 8].

The copper and nickel layers were grown at room temperature and the substrates were rotating during deposition in order to get a good thickness uniformity. Following each deposition, the Ni/Cu/Si thin films were characterized by RHEED. RHEED reveals the growing in the (001) orientation of the Cu and Ni layers with the following in-plane epitaxial relationships between silicon, copper and nickel layers: Si[110] ∥ Cu[100] ∥ Ni[100]. The growth of Ni(001) on Cu(001) is more direct: the nickel lattice is totally or partially commensurate with the Cu. Since the lattice mismatch between them is about 2.6%, epitaxial growth of Ni is favourable and has been frequently observed[7, 22].

The critical thickness t_c (the thickness below which the nickel is totally commensurate with the Cu buffer layer) can be found by setting the equilibrium strain $\epsilon_{\|}^{e} = 2.6\%$ (which is the misfit strain of Ni on Cu), and it is computed to be about 16Å. This value agrees with the experimental result on Ni/Cu(001) system reported by Matthews and Crawford [1970] and Inglefield *et. al.* [1993]

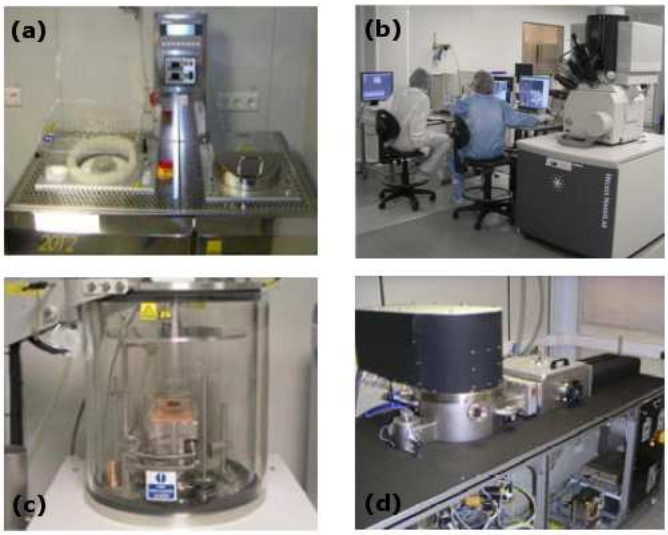

Figure 6: Pictures of the equipments used for patterning rings on Cu/Ni/Cu/Si(001) films. (a) Spin coater and hot plate. (b) Helios 600 dual beam equipment. (c) Electron gun evaporator from *Eduards*. (d) Ion milling equipment by *Sistec*.

using TEM technique.

ELECTRON BEAM LITHOGRAPHY (EBL)

A serie of Cu(5 nm)/Ni (t_{Ni})/Cu (100nm)/Si(001) (t_{Ni}= 10 - 16 nm) thin films were patterned by a subtractive process using electron beam lithography, electron beam evaporation, lift-off techniques and ion-milling. The lithography process was performed with a dual beam Helios 600 system equipped with Raith lithography hardware. The fabrication was carried out in the INA and LMA laboratories where the equipments are installed in a class 10.000 clean room, an image of the instruments used is shown in Fig. 6.

Rings in arrays with different external diameter and width were fabricated. The distribution of the elements in the matrices and number of structures per matrix were checked in different configurations in order to find the optimum preparation procedure improving the quality of the elements and to make the MFM experiments easier. Thus, before each experiment the starting point was to create the models to be designed by using the ELPHY program of Raith. The separate steps involved in the fabrication are detailed as follow:

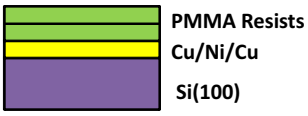

Figure 7: Schematic of Cu/Ni/Cu patterning layers, pre-lithography process.

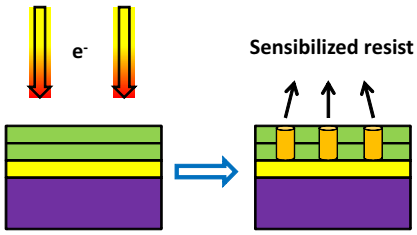

Figure 8: Schematic of exposure step by using a Dual Beam equipment provided with Raith lithography hardware.

- **Spin coating:** The Cu/Ni/Cu//Si thin films were covered with a double layer of e-beam resist. The spin coating of a film of 50 Kg/mol polymethylmethacrylate (PMMA) resin (Allresist AR-P 639.04) at 2000 r.p.m. for 20 seconds to form a $\approx$ 120 nm thick layer. The sample was then soft baked for 10 minutes at 120°C on hot plate. A second coated film of 950 Kg/mol PMMA (AR-P 679.04) at 4000 r.p.m. for 20 seconds to form a $\approx$ 270 nm thick layer. Once more, the sample was soft baked for 10 minutes at 120^oC on hot plate to remove excess solvents and prepare it for exposure.

- **Electron beam writing:** The designs are directly defined by the scanning electron beam, then the resist is chemically modified due to the energy deposited from the electron beam. As the resist used is positive, the rings areas are sensibilized. The delivered dose area was 99 μC/cm^2 at 10 kV accelerating voltage and beam current of $\approx$ 80 pA (see sketch in Fig. 8).

- **Develop:** The energy deposited during the exposure creates a latent image that is materialized during chemical development. For positive resists, the development eliminates the patterned area. The exposed sample was developed with AR 600-56 developer for 30 s with a soft agitation followed for stopping in isopropil alcohol for 30 seconds. A picture at this point process is shown in Fig. 9.

- **Hard mask evaporation:** After de development, a double metal layer was grown to protect the nanostructures of the ion-milling process. Both layers were grown by electron beam evaporation in a high vacuum chamber at a base pressure of 2×10^{-7} mbar. A chromium film of 5 nm is

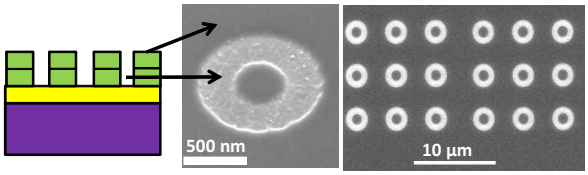

Figure 9: Schematic of the result of the development step (left) and corresponding SEM images of an example of a post-development sample (right).

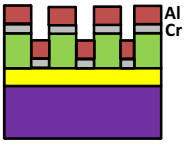

Figure 10: Schematic of the metal hard mask evaporation onto the patterned rings.

deposited for improving the adhesion followed by 14 nm of Aluminium, the rate of deposition of the two layers was 1.3 A^o/s (see Fig. 10).

- **Lift-off:** This procedure was carried out by submerging the sample in N-Methyl-2-pyrrolidone (NMP) solution at 75 ^{o}C for more than 2 hours and a quick ultrasonic bath. When the sample is immersed in NMP, the areas with resist behind the Cr/Al are removed.

- **Ion-milling:** The sample is introduced in an ion etching equipment where Argon ions impinge on the sample to remove the Ni unprotected areas with the Cr/Al hard mask. An electron neutralizer gun is used before arriving the ions at the sample, making this process softer to the surface. The Ar pressure was 4.7×10^{-4} mbar and the milling rate was 10 nm/min for 2 minutes.

Figure 13 shows examples of different patterned structures fabricated along this thesis. (a) AFM image of a row of a matrix with 3 μm external diameter and widths ranging from 130 to 540 nm. The topographic and magnetic images of a matrix of rings with 3 μm external diameter and width = 900 nm are shown in Figs. 13 (b) and (c), respectively. In Fig. 13 (d), a tridimentional AFM image of one of the rings plotted in pane (b) is shown. Finally, magnetic contrast is observed only on the surface of the ring indicating that the Ni layer out-side was removed with the ion-milling process.

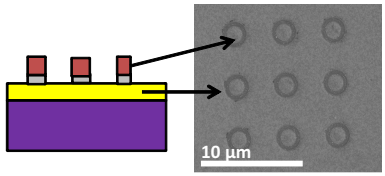

Figure 11: Schematic (left) and SEM image (right) of the Cu/Ni/Cu patterned rings covered with a Cu/Al double film.

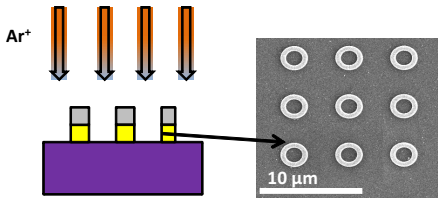

Figure 12: Schematic (left) and SEM image (right) of the Cu/Ni/Cu patterned rings with a well defined profile due to the lack of the magnetic layer in the surrounding area.

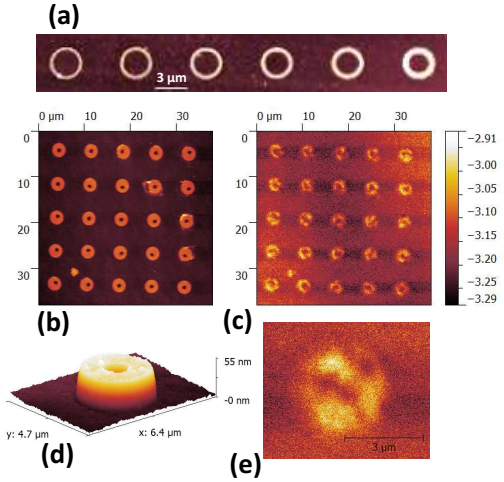

Figure 13: Examples of the patterned structures and MFM characterization. (a) Rings of 3μm external diameter and different widths. (b) and (c), Matrix of rings of 3μm external diameter and MFM images, respectively. (d) and (e), AFM and MFM image of a ring of the matrix shown in (b).

References I

[1] J. Echigoya, H. Enoki, T. Satoh, and T. Waki, Appl. Surf. Sci. **56**, 463 (1992).

[2] C. S. Liu, L. J. Chen, Appl. Surf. Sci. **92**, 84 (1996).

[3] Chin-An Chang, Joyce C. Liu, and Joseph Angilello, Appl. Phys. Lett. **57**, 2239 (1990).

[4] B. G. Demczyk, R. Naik, G. Auner, C. Kota, and U. Rao, J. Appl. Phys. **75**, 1956 (1994).

[5] I. Hashim, B. Park, and H. A. Atwater, Appl. Phys. Lett. **63**, 2833 (1993).

[6] R. A. Lukaszew, Y. Sheng, C. Uher, and R. Clarke, Appl. Phys. Lett. **76**, 724 (2000).

[7] E. Inglefield, Misfit accommodation in thin films of Ni/Cu as measured by magnetic anisotropy, Ph.D. Thesis MIT (1995).

[8] Chin-An Chang, J. Appl. Phys. **67**, 566 (1990).

[9] J. W. Mattews and J. L. Crawford, Thin solid films **5**, 187 (1970).

Chapter II

Perpendicular Anisotropy in Ni Multilayers

Introduction

The aim of this chapter is the study of the mechanism, either structural or magnetics, involved in the physics of magnetic quantities measured in multilayers that are modified with respect to the values found in single thin films. The coercive field H_c, the domain size D and magnetic anisotropy is studied in epitaxial [Ni/Cu]xN structures with t_{Ni}= 3 nm and 4 nm, two values for which the Cu/Ni/Cu structure show a remarkable perpendicular magnetization with large remanence and negative nucleation field.

It is well known that magnetic thin films present fundamental properties that change with respect to the bulk values because of the competition of magnetic and structural correlation length as well as the reduction of the space dimensions from 3 to 2. In structures with perpendicular magnetization, used in spintronic devices, many functional blocks may include several repetitions of a bilayer structure [1, 2], resulting in a class of synthetic magnetic materials. In this chapter, it is shown that important properties from a technological point of view, as H_c and D, can be controlled in functional blocks with perpendicular magnetic anisotropy.

The procedure used to grow the Cu/Ni/Cu systems has been described in the previous chapter. The RHEED images show patterns that correspond to epitaxial Ni can Cu layers growing on the (001) plane. Therefore the next series has been grown:

- A) Ni films with t_{Ni} ranging between 2 nm and 20 nm.
- B) Ni/Cu/Ni bilayers with t_{Ni}= 3 nm and the t_{Cu} ranging between 0 and 6 nm.
- C) [Ni/Cu] x N layers with t_{Ni}= 3 nm and t_{Cu} = 3 nm and N up to 4
- D) [Ni/Cu] x N layers with t_{Ni}= 4 nm and t_{Cu} = 3 nm and N up to 4

X-RAY CHARACTERIZATION

Ex situ characterization has been done by means of x-ray diffraction using several Cu Kα laboratory sources located at the LMA (Bruker D8) SAI Rigaku and synchrotron radiation X-ray radiation (photon energy hν =15 keV, λ = 0.826Å) at the BM25B beamline of the European Radiation Synchrotron Laboratory.

Grazing incidence diffraction experiment

The BM25 line has a six circle diffractometer that allow the realization of maps in the reciprocal space with high resolution of thin films with thicknesses lower than 12 nm, as can be observed in the reciprocal space map shown in Fig. 14 taken around the (420) Cu reflection for a 9 nm thick Ni film. Using laboratory sources maps for films thicker than 12 nm can be obtained although the ratio signal to noise is higher, see in Fig. 65b the map taken for 14 nm thick Ni film with the D8 Bruker diffractometer.

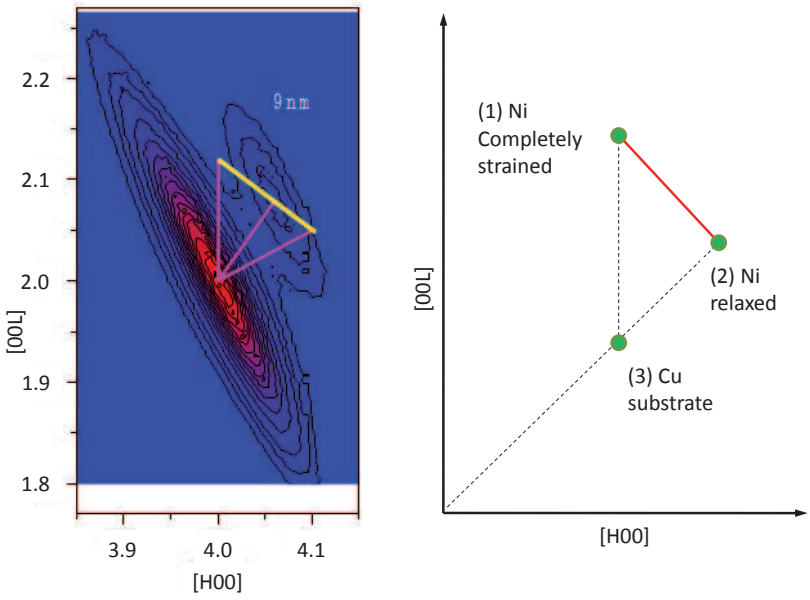

Figure 14: (Left) Reciprocal lattice map made on a Cu/Ni/Cu film with $t_{Ni} = 9$ nm. (right) Sketch of the location of the reciprocal lattice peaks of a thin film with respect to the substrate.

The in-plane lattice parameter has been measure by means of grazing in-

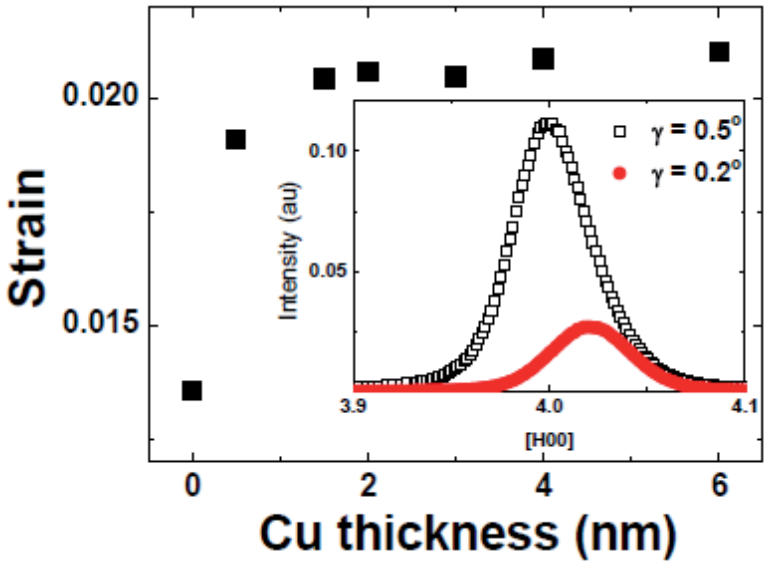

Figure 15: Strain in the Ni/Cu/Ni structure as a function of t_{Cu}, the inset shows grazing incidence diffraction from the (400) Bragg planes of the copper and nickel layer in the $t_Cu = 2$ nm structure at two incident angles 0.2 ^{o} and 0.5 ^{o}, units of the scattering vector are related to the primitive cell of the bulk copper.

cidence diffraction (GID) at the BM25B beamline of ESRF for the series B. Using this technique the incident and diffracted beams form an angle with the surface less than 1^o therefore the radiation only scans the outer layers of the structure and the measured peaks correspond to planes perpendicular to the film surface (in a similar fashion to the RHEED technique). The insert in Fig. 15 show the variation of the signal around the 400 reflection as a function of incident angel. The in-plane strain, estimated with the in-plane lattice parameter, has been obtained from for the series B as a function of t_{Cu} as is shown in Fig. 15.

Symmetric diffraction experiments

Symmetric diffraction experiment has been carried out to obtain information about the out-of-plane lattice parameter and the bilayer period in Cu/Ni structures.

The X-ray diffraction experiments were performed using Rigaku Dmax 2500 diffractometer. The system consists of a rotating anode generator operating at 40 kV and 100 mA. The diffraction spectra were measured in the symmetric reflexion geometry around the Cu(002) Bragg peak as it is shown in Figs. 16 and 17 for series C and D, respectively. The intensities from the (002) plane

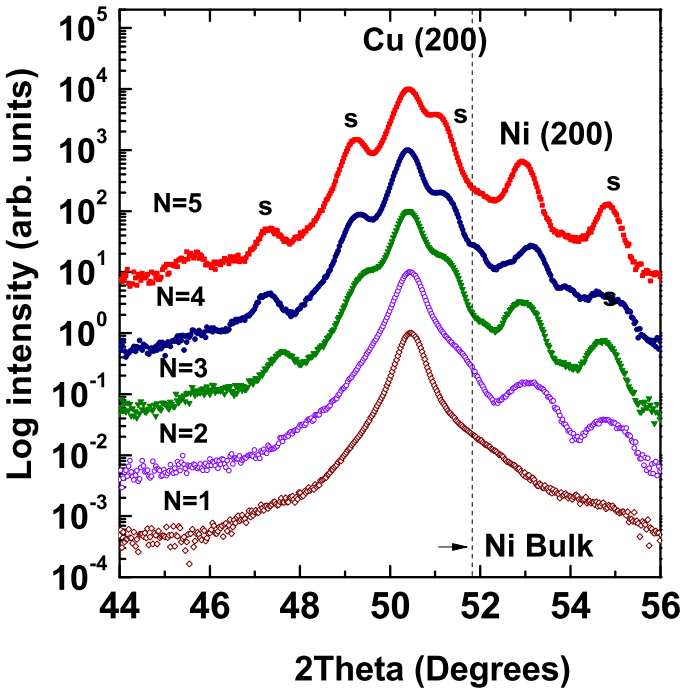

Figure 16: X-ray diffraction scans as a function of the number of Ni blocks for [Ni(3 nm)/Cu(3 nm)]xN structures. The superlattice peaks are marked with s.

show a large peak that correspond with the Cu buffer layer ($2\theta_{Cu}$= 50.44) and gives the bulk lattice parameter. Also Ni (for single thin films), and superlattice peaks are located for 2θ larger that $2\theta_{Cu}$. A comparison between the N = 2 data for the samples with t_{Ni} = 3 nm and 4 nm show clearly that the separation between the superlattice peaks increases for as t_{Ni} decreases. We note that the the number of peaks observed increases with N and that in both series the location of these peaks remain at relative fixed positions, and the peak width tend to decrease with N.

The fitting procedure has been done using an interactive peak fitter program of Matlab (Peakfit.m[3]) using Person shape peaks. An example is shown in Fig. 18 for a structure with t_{Ni} = 4 nm and N = 2. The fit provide the value of the θ, height, width and area of the peaks.

The period of the superlattice is the thickness of one double layer, i. e., Ni/Cu, and is defined as:

$$\Lambda = n_{Cu}p_{Cu} + n_{Ni}p_{Ni} \tag{1}$$

where p_{Cu} and p_{Ni} are the perpendicular to the plane Cu and Ni lattice parameters, respectively, and n_{Cu} (n_{Ni}) is the number of planes of Cu (Ni) layer.

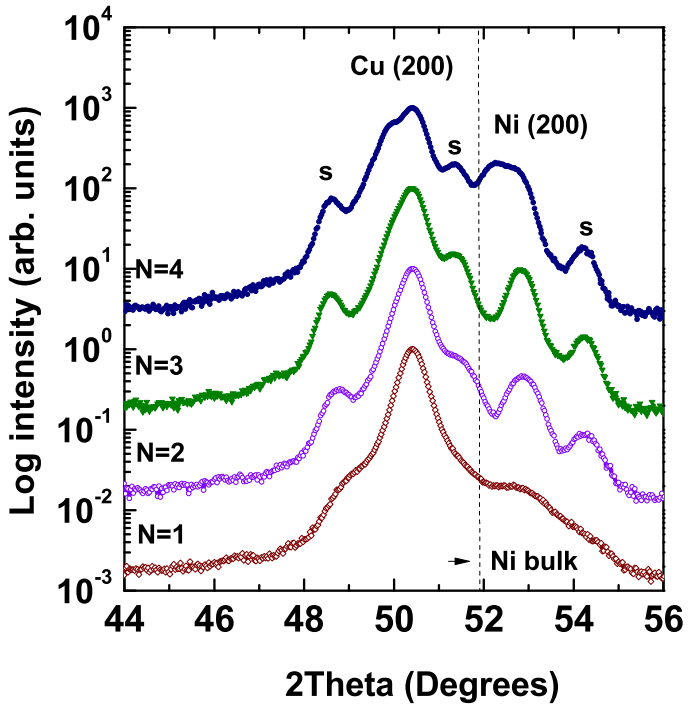

Figure 17: X-ray diffraction scans as a function of the number of Ni blocks for [Ni(4 nm)/Cu(3 nm)]xN structures. The superlattice peaks are marked with s.

The lattice periodicity give rise to satellites accompanying the reflections of the average lattice parameter at positions in reciprocal space determined by the length Λ of the repetition unit [4]. The Λ value can be directly measured from the distance in the reciprocal space between the low-k satellite at $\frac{-2\pi}{\Lambda}$ (k_1) and its high-k satellite at $\frac{+2\pi}{\Lambda}$ (k_2) around the main Bragg peak, so that[4]

$$\Lambda = \frac{4\pi}{k_2 - k_1} \tag{2}$$

with

$$k = \frac{4\pi \sin\theta}{\lambda} \tag{3}$$

Then, the total number of planes in one bilayer is given by

$$n = \frac{\Lambda}{p} = \Lambda \times \frac{k_{Bragg(200)}}{2\pi} \tag{4}$$

where p is the averaged lattice parameter.

By considering the Ni layers, the measured and calculated 2θ positions, k Bragg values, period and number of planes of a bilayer for the two structures studied are presented in Table 1.

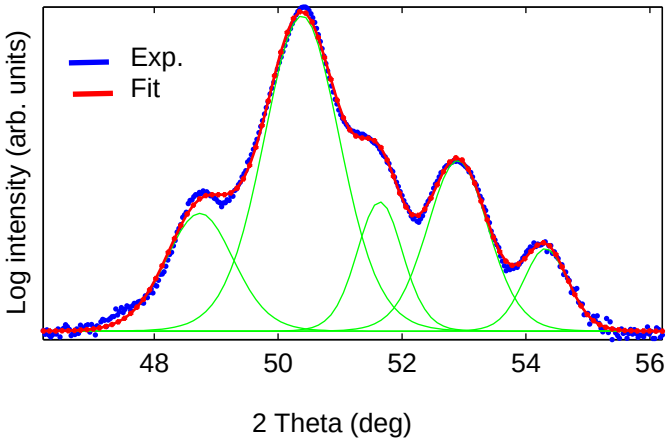

Peaks = 5 Shape = Pearson Error = 1.3868

Peak	X position	Peak height	Peak width	Peak area
1	48.737	2.25652	2.54887	3.18218
2	50.3845	6.04154	2.86111	9.56534
3	51.6412	2.47684	1.72703	2.3671
4	52.8986	3.27123	2.29808	4.16
5	54.3174	1.58241	1.68218	1.47294

Figure 18: Example of using an interactive peak fitter program on a x-ray diffraction pattern for a sample with t_{Ni}= 40 Åand N=2. The conditions used for the adjustment are presented too.

N	$2\theta(k_{Bragg})$ (deg)	$2\theta(k_1)$ (deg)	$2\theta(k_2)$ (deg)	k_{Bragg} (Å^{-1})	k_1 (Å^{-1})	k_2 (Å^{-1})	Λ_{Exp} (Å)	Λ_{Cal} (Å)	n
1	53.3								
2	53.15	51.04	54.79	3.65	3.51	3.75	60	52.58	30.54
3	52.95	51.17	54.72	3.63	3.52	3.74	60	55.55	32.15
4	53.14	51.21	54.71	3.64	3.52	3.74	60	56.35	32.72
5	52.93	51.07	54.82	3.63	3.51	3.75	60	52.59	30.42
				Ni=40 Å					
1	52.86								
2	52.85	51.3	54.2	3.63	3.53	3.71	70	67.94	39.25
3	52.83	51.85	54.23	3.62	3.53	3.71	70	68.43	39.52
4	52.71	51.36	54.21	3.62	3.53	3.71	70	69.15	39.85

Table 1: Experimental 2θ positions of the Ni(200) Bragg peaks and parameters calculated by using Eqs. 2, 3, 4. N is the number of bilayers, n is the total number of planes, Λ experiment or calculated.

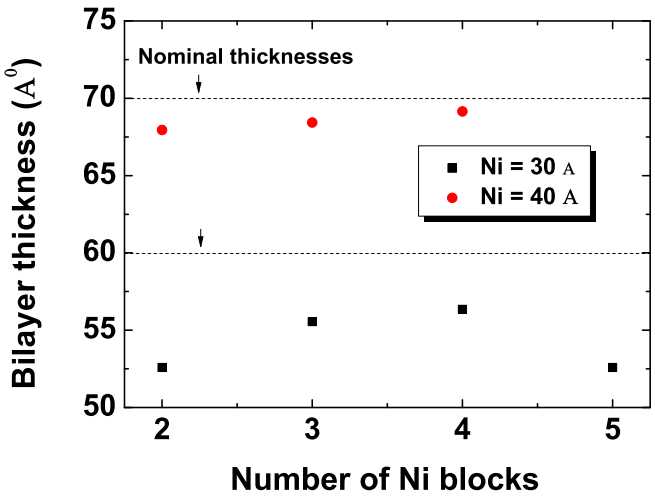

Figure 19: Bilayer thicknesses as a function of the number of Ni blocks for multilayer with t_{Ni} = 30 and 40 Å. The nominal thickness values for both system are indicate with the dash lines.

Thus, from the values presented in Table 1, it is observed that the period of the superlattice with [Ni(3 nm)/Cu(3 nm)] blocks is in average $\approx 9\%$ smaller that the nominal value. This difference is smaller for the [Ni(3 nm)/Cu(4 nm)] structure, where Λ has an average value of the $\approx 2\%$ lower than the nominal one. The data are plotted in Fig.19. Note that these deviation between the experimental and the nominal values of Λ translated to monolayer units means a variation in the average thicknesses of around 1 or 2 monolayers.

Finally, in both series satellite peaks looks to be present at 2θ values smaller that the $2\theta_{Cu}$ peaks. For example by comparing N = 1 and 3 spectra of Figs. 16 and 17, the additional reflections around 2θaround 48 degrees becomes more defined for N = 3. Large order satellites appear if the variation of the composition of the bilayer is sharp because more higher orders in the Fourier coefficients are necessary in reproducing compositionally abrupt profiles. We note the large background due to the Cu buffer layer precludes a full fit of the superlattice experimental profile.

Now the average perpendicular strain is obtained by using the approximation that the value of the lattice parameters in the nickel and copper layers is homogeneous and follow a step function. Therefore the scattering amplitude due to the copper and nickel lattice do not interfere and, for structures with a low number of repeats, the maximum due to a single layer of Ni is very close to the maximum obtained after multiplying that function with the term due to the superlattice period. Therefore the out-of-plane lattice parameter and the average strain values, using the Ni bulk lattice parameter as reference, is calculated by using the 2θ positions of the peaks in the XRD patterns with the following expressions:

$$a_{\perp ave} = \frac{2\lambda}{\sin\theta} \tag{5}$$

and the Ni out-of-plane strain:

$$\epsilon_{\perp} = \frac{a_{\perp ave} - a_{Nibulk}}{a_{Nibulk}}, \tag{6}$$

The $a_{\perp ave}$ and $\epsilon_{\perp}$ values obtained for both structures are listed in Table 2. In addition, in Fig. 20 the results for $\epsilon_{\perp}$ are plotted. In general, $\epsilon_{\perp}$ increases with the number of bilayers indicating that the Ni lattice is getting relaxed. For the t_{Ni}= 3nm structures there is a lineal dependence up to N = 3 and the $\epsilon_{\perp}$ values change from -2.5% to -1.9% while for the series with t_{Ni}= 4 nm the deformation is stable up to N = 3 with values around -1.7% and then at N = 4 it increases to -1.5%. These results also reveal that the in-plane strain for structures with t_{Ni}= 3 nm is larger than for the structures with t_{Ni}= 4 nm.

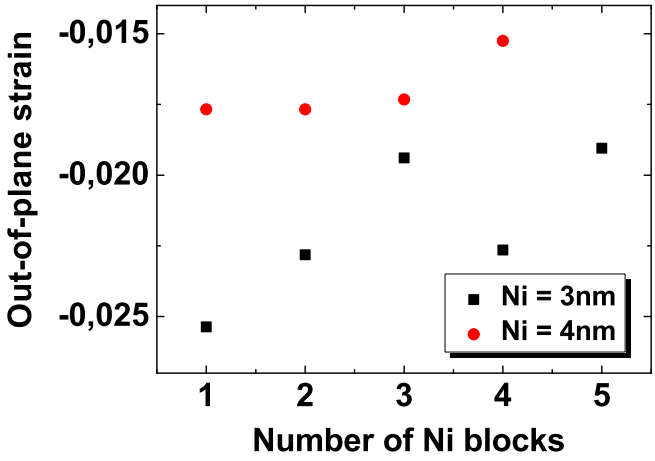

Figure 20: Out-of-plane strain as a function of the number of Ni blocks for multilayers with t_{Ni} = 30 and 40 Å.

N	$a_{\perp ave}$(Å) Ni 3 nm	$a_{\perp ave}$(Å) Ni 4 nm	$strain_{\perp}$ Ni 3 nm	$strain_{\perp}$ Ni 4 nm
1	3.43	3.46	-0.025	-0.017
2	3.44	3.46	-0.022	-0.017
3	3.45	3.46	-0.019	-0.017
4	3.44	3.47	-0.022	-0.015
5	3.45		-0.019	

Table 2: Average perpendicular lattice parameters and the calculated perpendicular strain values for [Ni(t_{Ni})/Cu(3 nm)]xN structures with t_{Ni}= 3 nm and 4 nm.

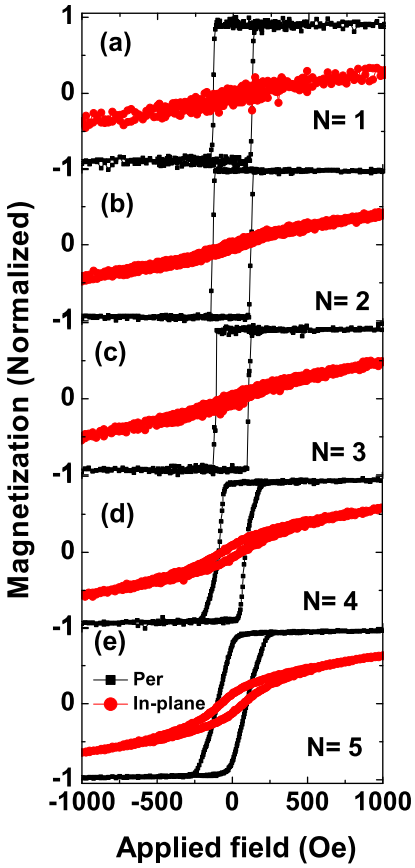

Figure 21: Perpendicular and in-plane magnetization loops for Cu(1000Å)/[Ni(30Å)/Cu(30Å)]xN structures. The magnetization has been normalized to the saturation value M_s = 480 kA/m. The applied field range is ± 15 kOe.

MAGNETIC PROPERTIES

Volume Averaged Magnetometry

The magnetic properties have been studied by means magnetometry and magnetic force microscopy (MFM). Hysteresis loops with the magnetic field applied parallel and perpendicular to the plane were measured for [Ni(3 nm)/Cu(3 nm)]xN and [Ni(4 nm)/Cu(3 nm)]xN structures, the results are plotted in Figs. 21 and 22, respectively. In both cases the superlattices show a clear perpendicular magnetic anisotropy with a large remanence of the out-of-the plane loops. For the structures with t_{Ni} = 3 nm, at N = 1 and N = 2 the remanence (M_r) and the saturation (M_s) magnetization are equivalent, then

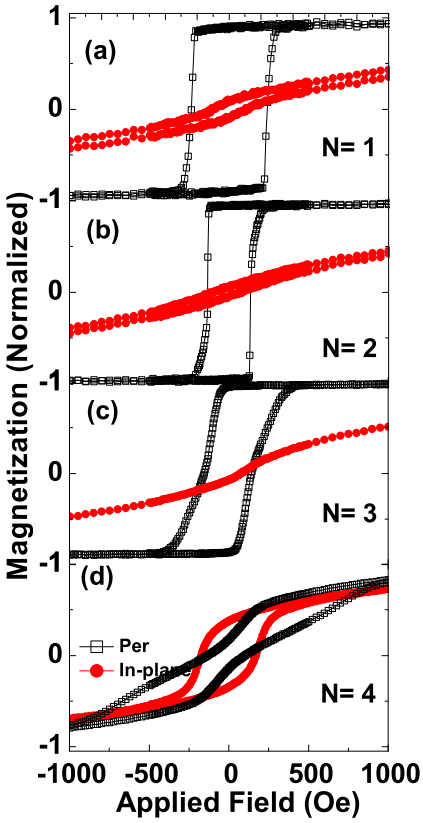

Figure 22: Perpendicular and in-plane magnetization loops for Cu(1000Å)/[Ni(40Å)/Cu(30Å)]xN structures. The magnetization has been normalized to the saturation value M_s = 480 kA/m. The applied field range is ± 15 kOe.

for N = 3 $M_r = 0.97M_s$, for N = 4 $M_r = 0.9M_s$ and, for N = 5 M_r= $0.78M_s$. On the other hand, the structures with t_{Ni}= 4 nm up to N = 3 have similar M_r= $0.95M_s$ values while for N = 4 M_r= $0.17M_s$.

The effective magnetic anisotropy constant, K_{eff} is estimated from the difference between the free energy of magnetization loops carried out in the film plane and perpendicular to the film surface. The in-plane loops were taken with H applied along the Ni[010] in-plane direction. To eliminate the effect of hysteresis in the M(H) loops, we have used the anhysteretic M(H) curve: for a value of M, the two corresponding values of H, taken from the increasing and decreasing field branches of the M(H) loop, are averaged. Thus, K_{eff} is positive in all cases and decreases as the number of layers N. For the structures with t_{Ni}= 3 nm the calculated values are: for N = 1 K_{eff}= 89 kJ/m^3, for N = 2 K_{eff} = 73 kJ/m^3, for N = 3 K_{eff} = 44 kJ/m^3, for N = 4 K_{eff}= 44 kJ/m^3, and for N = 5 K_{eff} = 39 kJ/m^3. On the other hand, for the structures

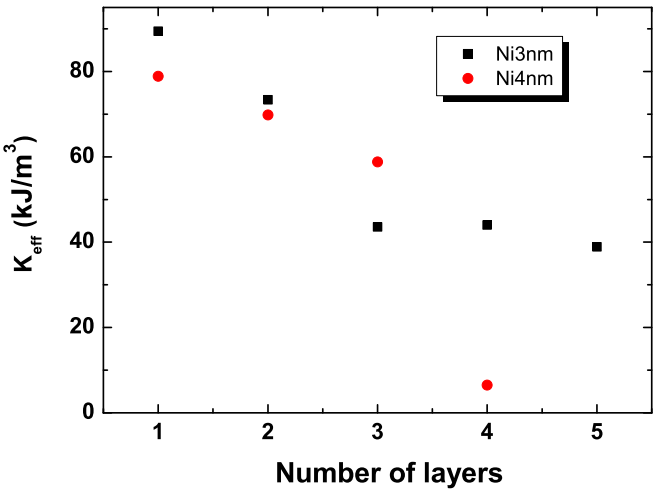

Figure 23: Effective magnetic anisotropy constants estimated from the anhysteretic magnetization curves as a function of the Ni blocks number for multilayers with t_{Ni}= 3 nm and 4 nm.

with t_{Ni}= 40 Å the calculated values are: for N=1 K_{eff}= 79 kJ/m^3, for N = 2 K_{eff}= 70 kJ/m^3, for N = 3 K_{eff}= 59 kJ/m^3, and for N = 4 K_{eff}= 6.5 kJ/m^3. Figure 23 displays these values so that both structures with different Ni thicknesses can be compared.

The loops show that the coercive field, H_c, also decreases as the number of layers increase, this dependence is shown in Fig. 24. The larger values of the reverse and coercive field are observed for the single Ni block structures.The measured values for the superlattices with t_{Ni}= 3 nm are: N = 1 H_c = 130 Oe, N = 2 H_c = 128 Oe, N = 3 H_c = 105 Oe, N = 4 H_c = 85 Oe and N = 5 H_c = 97 Oe. For the superlattices with t_{Ni}= 4 nm are: N = 1 H_c = 237 Oe, N = 2 H_c = 135 Oe, N = 3, H_c = 148 Oe and N = 4 H_c = 131 Oe.

Magnetic Domain Structure

A deeper analysis of the magnetic domain configurations involved in the hysteresis loops is obtained by means of magnetic force microscopy. Figure 25 shows MFM images taken at the virgin state for the [Ni(t_{Ni})/Cu(3 nm)]xN (t_{Ni}= 3 nm and 4 nm) structures with N = 2, 3, 4 and 5. The images were taken at constant height scans over the film surface. The samples were demagnetized by applying a perpendicular magnetic field. The distance between tip and film was reduced to improve the signal noise ratio up to a value where the topography signal did not overcome the magnetic one or the magnetic tip did not modifies the domain structure. An estimation of the period of the MFM images (i.e.,twice the domain size) was obtained from the profile of the self-correlation transform of the MFM images[23]. The set of images show clearly

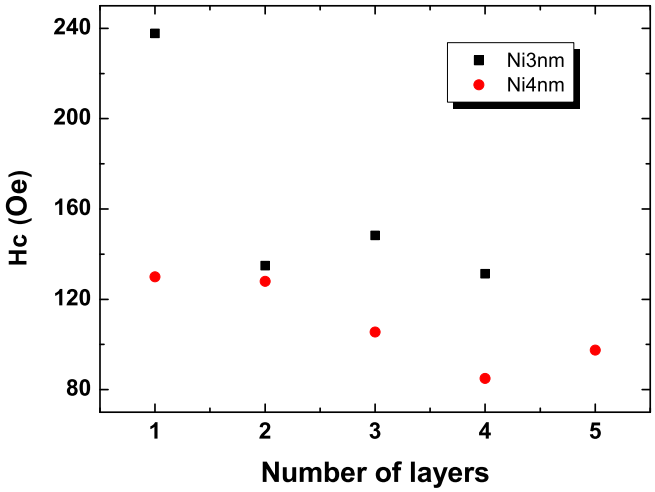

Figure 24: Coercive field for [Ni(t_{Ni})/Cu(30 nm)]xN structures with t_{Ni}= 3 nm and 4 nm structures vs the number of Ni blocks.

that the mean domain size D decreases as N increases and thus D is virtually infinity for N = 1 but becomes measurable for the rest of films being 1.5, 1, 0.45 and 0.3 μm for the N = 2, 3, 4 and 5, respectively, and Ni blocks with t_{Ni}= 3 nm. For the blocks with t_{Ni}= 4 nm, the average sizes are: 1.1, 0.7 and 0.3 μm for N = 2, 3 and 4, respectively. Notice that the N = 4 and 5 structures show the formation of a maze domain structure. This transition from a state of virtual monodomain state to a multidomain state can be explained by the decrement of the demagnetization energy due to the dipolar interaction between the Ni blocks, therefore a larger number of domain walls can be generated in the films resulting in smaller value of D.

Figure 27 shows field dependent MFM images taken in the structure [Ni(3 nm)/Cu(3 nm)]x4 with the magnetic field applied perpendicular to the film plane. The domain pattern for each H value is marked with an arrow on the perpendicular hysteresis loop. Notice that the inversion magnetization process is taken place through the nucleation of small bubbles and stripes (Fig. 27(b)), then they grow up (from Fig. 27(c) to Fig. 27(h)) and at the end near the saturation, some bubble domains are observed (Fig. 27(i)).

In order to quantify the magnetic energy of the domain structures observed, two contributions to the total energy are consider: the magnetostatic energy, e_{ms}, originating from the poles at the interfaces between the Ni layers and the Cu layers, and the wall energy of the domain walls between neighbouring domains, e_w. Thus, we have used the expression of e_{ms} given by H. J. G. Draaisma and W. J. M. de Jonge[14]:

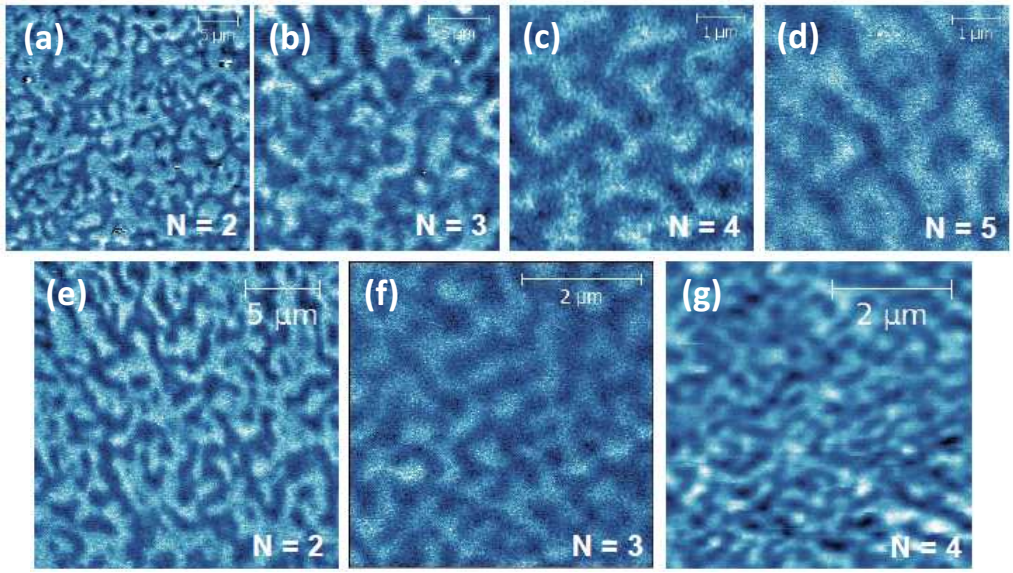

Figure 25: MFM images for [Ni(t_{Ni})/Cu(3 nm)]xN structures. In (a - d) t_{Ni}= 3 nm and (e - g) with t_{Ni}= 4 nm, for different N values. Notice that the scales are not the same.

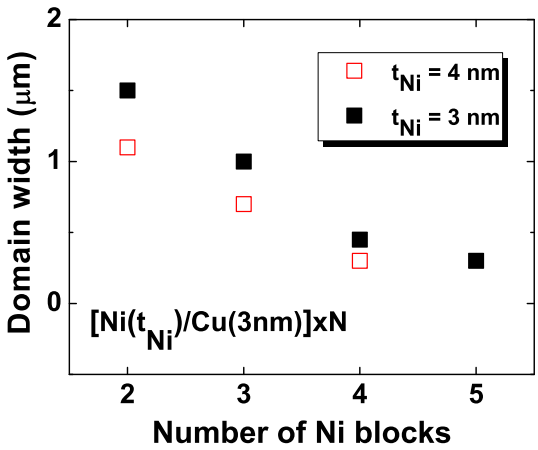

Figure 26: Average domain size vs. N dependence for the series with t_{Ni} = 3 nm and 4 nm.

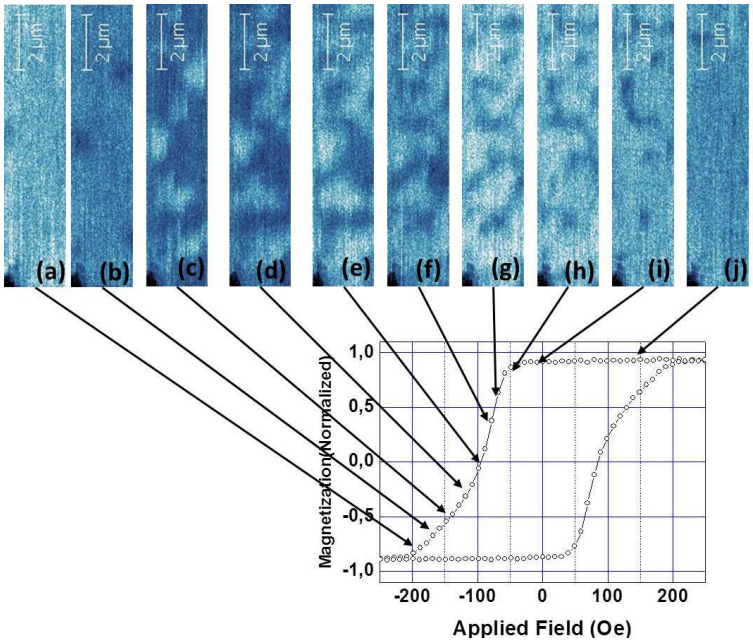

Figure 27: MFM images taken for the [Ni(nm)/Cu(3nm)]x3 sample with H applied along the normal direction.

$$e_{ms,n} = \frac{E_M}{\frac{1}{2}\mu_0 {M_s}^2} = m^2 + \sum_{n=1}^{\infty} \frac{4}{n\pi^3} \frac{D}{t_{Ni}} \times \sin^2\left[\frac{1}{2}\pi n(m+1)\right] f(D) \qquad (7)$$

with

$$f(D) = \quad 1 - exp\left(-2\pi n \frac{t_{Ni}}{D}\right) + \frac{\sinh^2\left[\pi n(\frac{t_{Ni}}{d})\right]}{\sinh^2\left[\pi n(\frac{\Lambda}{D})\right]} \times \left\{\frac{1}{N}\left[1 - exp\left(-2\pi n N \frac{\Lambda}{D}\right)\right] - \left[1 - exp\left(-2\pi n \frac{\Lambda}{D}\right)\right]\right\} \qquad (8)$$

where M_s is the saturation magnetization of Ni, D is the domain size, Λ is the bilayer thickness, N is the number of bilayers and m = $\frac{d_1 - d_2}{d_1 + d_2}$ with d_1 and d_2 the domain lengths up and down, respectively. In our case $d_1 = d_2 = D$, then m = 0.

The normalized wall energy can be written as:

$$e_{w,n} = \frac{\sigma_w}{d(\frac{1}{2}\mu_0 {M_s}^2)} \qquad (9)$$

here σ_w is the wall energy per unit area.

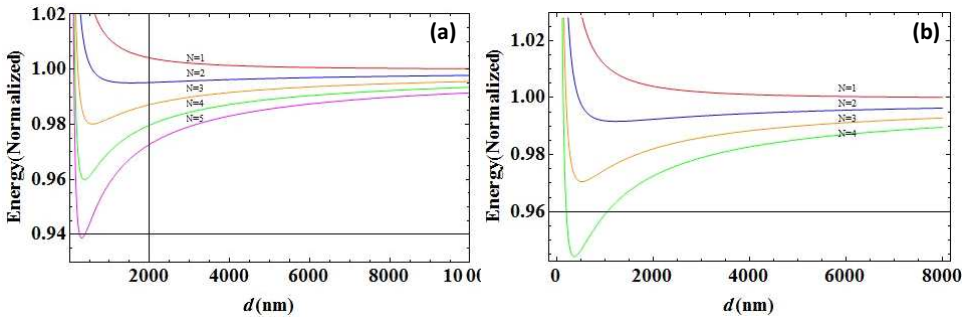

Figure 28: Energy of the system as a function of the domain width d for Cu(1000Å)/[t_{Ni}/Cu(30Å)]xN structures. (a) t_{Ni}= 3 nm, (b) t_{Ni}= 4 nm.

Therefore, the total energy is given by:

$$e_{T,n} = e_{ms,n} + e_{w,n} \tag{10}$$

The dependence of the total energy (Eq. 10) with the domain size as a function of the number of Ni blocks for multilayers with t_{Ni} = 3 nm and 4 nm is shown in Fig. 28. The same σ_w= 5×10^{-3} J/m^2 value has been used to calculated the total energy. Well defined minima of the energy are observed as the number of the Ni blocks increases. The calculated domain sizes are similar to those found by MFM in Fig. 25.

DISCUSSION

From the hysteresis loops in Figs. 21 and 22 it is deduced that the easy magnetization direction is perpendicular to the plane for all the samples. The remanent magnetization decreases as N increases, specially for the structures with t_{Ni}= 4 nm. Thus, the effective anisotropy constant behaviour show relevant differences between the structures with t_{Ni}= 3 nm and 4 nm. In the first case, we observe a strong reduction of K_{eff} from N = 2 (73 kJ/m^3) to N = 3 (43 kJ/m^3), followed by a stabilization up to N = 5. On the other hand, for Ni thicknesses bigger, K_{eff} decreases in steps $\leq$11 kJ/m^3 up to N = 3 and rapidly drops at N = 4 to a situation where the in-plane and out-of-the plane magnetization are balanced out. These features are very significant since the perpendicular magnetic anisotropy in Ni thin films disappear around 12 nm, but if the total Ni thicknesses is consider in both kind of multilayers, that value is extended to 15 nm (for the t_{Ni} = 3 nm structures) and 16 nm (for the t_{Ni}

= 4 nm structures), meaning that the growth of blocks of Ni layers separated by a Cu interlayer stabilize the range of perpendicular anisotropy to larger Ni thickness. These important results can be related with the structural properties discussed before since the calculated average out-of-plane strain values of the Ni blocks reveled that the structures with t_{Ni}= 3 nm are able to maintain a large strain in Ni layer and therefore, the magnetoelastic anisotropy responsible of the perpendicular anisotropy in this system overcome other anisotropy contributions up to larger values of nickel thickness that the value of the nickel single film, whereas the structures with t_{Ni}= 4 nm present a lower strain value with a significant decrement for the N = 4 stacking.

The coercive field also decreases with the number of Ni blocks in both structures. The strongest variation is observed between N = 1 and N = 2 for t_{Ni}= 4 nm, where the reduction correspond with 100 Oe. Then, we observe that the values tend to stabilize with the number of structures. This results will be discussed in detail latter.

In addition, we observe that for N = 1 and N = 2 structures, $M_s \approx M_r$, indicating that the inversion of the magnetization vector takes place through a process that involves the nucleation and expansion of the domains. Structures with larger values of N show larger differences between M_s and M_r, indicating that the transition between the single domain states occur in a larger interval of magnetic field. MFM images show that the domain size decreases as the stack of Ni films increases. In agreement with the strong perpendicular anisotropy at N = 1, the perpendicular domains tends to higher values than 5 μm, images not shown here. The domain sizes are smaller for t_{Ni}= 4 nm than for t_{Ni}= 3 nm, this fact is correlated with the reduction of the K_{eff} values favouring for the first thickness the creation of domain walls. For this purpose the minimization of the total energy calculated by considering the magnetostatic energy and the domain walls energy show the same reduction of the average domain sizes at the experiment.

CONCLUSIONS

The x-ray diffraction data show that the alternating layers of Cu and Ni are coherent and, therefore constitute one single crystal with its unit cell large along the growth direction. The periodic lattice distortion gives rise to satellite peaks close to the Bragg reflections of the Cu buffer layer and Ni Bragg peak. The variation of the Ni Bragg peaks positions depends on the number of Ni

blocks showing that the Ni lattice tends to get relaxed at higher thicknesses than a single film with equivalent thickness. Thus, the structural properties are strongly correlated with the perpendicular magnetic anisotropy behaviour observed for the stacks of Ni separated by a Cu layer.

In spite of the strong perpendicular anisotropy of the Ni/Cu systems presented, a reduction the domain size can be controlled by the variation of thicknesses of the Ni and Cu layers, and therefore doing possible the control of the domain microstructure desired regarding to the application, i,e., maze, bubble, stripes domain patterns.

COERCIVE FORCE

In this section the reduction of the values of H_c as N increases is discussed in term of structural and magnetic parameters, and a model based on the propagation of misfit dislocations is proposed.

Introduction

H_c is defined as the field at which **M** is reduced for remanence to zero. Thus, coercivity measures the resistance of a ferromagnetic material to become demagnetized. In a M-H loop with remanent magnetization M_r, $4M_rH_c$ gives the order of magnitude of the loop area, which shows that H_c is a measure of the energy dissipation accompanying the magnetization process. H_c values can span an amazingly wide interval as function of the composition and microstructure of the material and the preparation procedure. Very soft materials used in transformers, $H_c \sim 1$ A/m, have been fabricated by alloying Ni and Fe or fabricating amorphous alloys to obtain a compound with zero magnetostriction and magnetic anisotropy values. On other extreme, hard magnetic materials with $H_c \sim 10^7$ A/m, used in motors are obtained alloying rare earths and 3d metals. The high impact that structural factors have in H_c for the same material can be observed in iron: for pure and high purity iron $H_c \sim 1$ A/m, for commercial polycrystalline pieces $H_c \sim 100$ A/m, while for single domain particles $H_c \sim$ even larger than 10^4 A/m.

That variation of H_c with the structure of the material has fueled the consideration of a wide number of mechanisms to model the problem of the magnetization process: coherent rotation, curling, bucking, buckling and domain wall nucleation has been invoked to explain the reversal of **M** in particles as function of their diameter. The creation of a domain wall introduces the

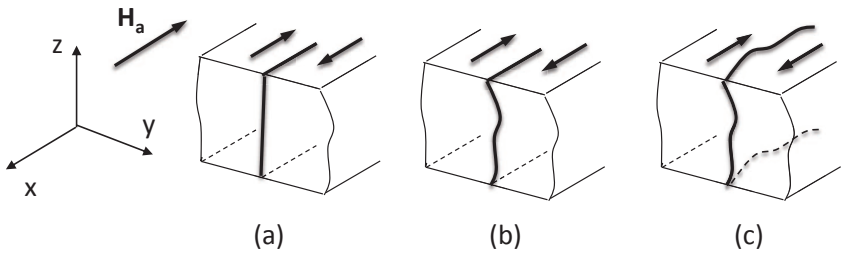

Figure 29: Increasing degree of wall distortion under progressively stronger interaction (pinning)(a) Rigid wall and low interaction, (b) one dimensional and (c)two dimensional bowing. The one dimensional bowing does not create charges in the DW.

concept of magnetic domain, that is a uniformly magnetized region created to minimize the magnetostatic energy. The inversion of the magnetization is carried out by discontinuous or Barkhausen jumps [7]; the jump, as explained by Langmuir [2], is a spatially inhomogeneous process: the propagation of a boundary between domains of opposite **M**. Domain walls can be pinned by defects in the material and are moved under the pressure of the external field. The physical picture of the term *wall pinning* corresponds to the impediments to wall motion arisen from structural disorder: non-magnetic inclusions, grain boundaries, residual stresses, etc.

In the description of these mechanisms, there are two points that deserve attention: the treatment of the wall as a rigid or flexible surface, see Fig. 29 and the dimensionality of the perturbation responsible for pinning. Thus, several models distinguish two regimes based on the ratio of the defect size to the wall thickness. A general statement of the problem introduces in the free energy terms due to the wall energy, that indicate the amount by which the energy stored in the distorted wall surface increases above the energy of a flat wall. The magnetostatic energy term indicates the presence of free poles on the wall surface. The interaction energy with pinning centers, that are assumed to be a random distribution of defects with average volume density ρ; the presence of a random pinning term introduces many local minima corresponding to slightly different wall surface configurations. The last considered term responds of the coupling between the defect and the applied field. This energy has to be minimized, and because the energy represents a stochastic, non-local and non-linear problem, and there is a large number of solutions, the most stable yielding the coercive force value.

When the wall is located in one of these minima, then, increasing the magnetic field will produce an adjusting of the DW surface through reversible distortions and Barkhausen jumps. General properties of the coercive field can be found on the basis of dimensional considerations and scale-invariance

arguments [8] and analytically [9, 10]. For the rigid wall approximation, the wall is a plane surface moving rigidly; the wall energy and magnetostatic energy are always at a minimum while the interaction with the defects will be high. The other extreme to deal with the problem is to consider a fully distorted wall that is corrugated to minimize the pinning energy at the expense of extra domain wall and magnetostatic energy. The first case implies that the pinning energy is small with respect to the wall and magnetostatic energies and the coercive field is obtained as the result of the interaction of a domain wall with a random pinning field, obtaining:

$$H_c = \frac{C}{\mu_0 M_s}\left(\frac{\rho}{L_x L_z \delta_p}\right)^{1/2} E_p \tag{11}$$

with C a constant, L_x and L_z the area of the domain wall, E_p the energy interaction of the DW with the defect and δ_p the DW - defect interaction length, typically of the order of the domain wall. To deal with the domain wall pinning mechanism that control the value of H_c the wall internal structure is neglected.

In the case of domain wall bowing the H_c [11] is given by:

$$H_c = \frac{C}{\mu_0 M_s}\left(\frac{\rho}{L_x}\right)^{2/3} \frac{E_p^{4/3}}{\gamma_w^{1/3}\delta_p} \tag{12}$$

where σ_w is the domain wall energy. The relation of the bowing of the DW with the interaction strength with the defect has been also shown by computer simulations [9]

Now the pinning mechanism for rigid DW is considered [8]. The relaxation of the strain in the nickel films occurs through the formation of misfit dislocations, see Fig. 30, so this source is assumed as the main factor determining the value of H_c. The dislocation core generates a local strain distortion which, through the magnetoelastic interaction, is coupled with the magnetic spins of the DW. The pinning energy due to the interaction of the DW with a single dislocation segment is of the order of $\mathrm{G}\lambda_s \mathrm{b}l\delta_p$, where G is the shear modulus, λ_s is the saturation magnetostriction constant, b is the amplitude of the Burgers vector and ℓ is the typical length of the dislocation segment that the wall encounters parallel to its plane. The dislocation density ρ_d can be related with the volume density ρ of dislocation segments of typical length ℓ are related being $\rho \sim \rho_d/3\ell$, then Eq. (11) becomes:

$$H_c = C\frac{G\lambda_s b}{\mu_0 M_s}\left(\frac{\rho_d \delta_p \ell}{3L_x L_z}\right)^{1/2} \tag{13}$$

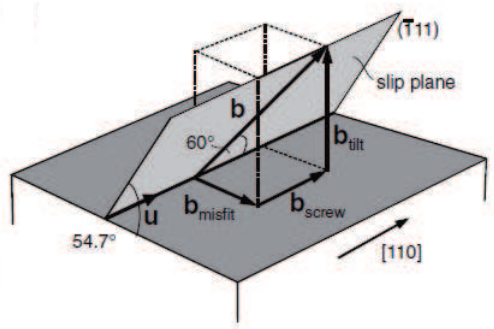

Figure 30: Burger vector of one 60^o misfit dislocation.

COERCIVE FORCE

The mechanisms involved in the inversion of the M in nanostructures that consist of magnetic blocks separated by a non magnetic spacer systems have manifold effects in their magnetic properties. In structures with in-plane magnetization, the dipolar coupling between DW survive large distances because the magnetic field generated by the domain walls can be large and favours a coupling between blocks in the nanostructure. The result is the decreasing of H_c [12] in multilayers with respect to the single film, the decreasing of the remanence of the hard magnetic layer by repeated switching of the soft magnetic layer [13], sharp drops in resistance at H_c in trilayers [14] and dynamics of magnetic domain wall motion in the soft electrode of a trilayer [15].

Therefore, the mechanisms involved in the inversion of the magnetization in nanostructures which may be forming one of the functional blocks in a magnetic structure show up as an important issue because the DWs interact with a spin-polarized current. Besides the technological relevance of the knowledge of H_c, basic issues are behind the displacement of the DWs since they are an example of force-driven transitions that includes charge-density waves in electric field, superconductors with large currents, plastic-forming process or earthquakes [16].

Coercive force in Ni/Cu/Ni bilayers

In this section the dependence of H_c with the t_{Ni} is presented for several series of Ni/Cu/Ni bilayers and Ni films.

Figure 31 shows the variation of H_c with t_{Ni} in a series of Cu/Ni/Cu films. A strong increment for t_{Ni} ranging from 1.5 to 3.5 nm is observed, with H_c changing from 100 Oe for t_{Ni} = 2 nm up to about 220 Oe for t_{Ni}= 4nm, while

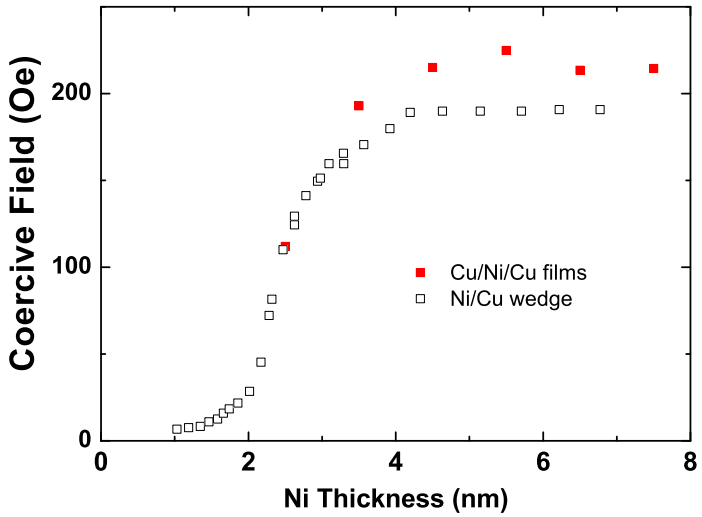

Figure 31: Coercive force as a function of t_{Ni} in a Ni wedge and in a series of Cu/Ni/Cu films

for larger thicknesses H_c remains roughly constant. The same trend has been observed previously [17] in Ni films grown on Cu single crystal. The larger values of H_c found in the Cu/Ni/Cu trilayers can be associated with the larger number of defects that are present in the 100 nm thick Cu seed layer compared with a Cu single crystal after a standard preparation (ion milling and annealing cycles) for thin film grown in ultra high vacuum environment.

The variation of H_c with the t_{Cu} spacer in the double films with $t_{Ni} = 3$ nm is shown in Fig. 32. From t_{Cu}= 0 to t_{Cu}= 1 nm, $H_{c,s}$ decreases from $\sim$ 220 Oe to 125 Oe while for $t_{Cu} > 1$ nm, $H_{c,s}$ does not depend of t_{Cu} and looks to take a value $\sim$ 130 Oe. A similar trend is observed for the in-plane strain measured by grazing incidence X-ray diffraction. Since the anisotropy constant K is proportional to the film strain state, after Eq. (13) the generation of misfit dislocation can modify H_c directly as a defect that pin the domain wall, and indirectly by modifying the domain wall size $\delta_p \sim (K/A)^{1/2}$.

Thus, H_c is compared in structures with similar values of perpendicular magnetic anisotropy. Figures 21 and 22 display out-of-plane M(H) loops taken for films and double films with $t_{Ni} = 3$ and 4 nm and $t_{Cu} = 3$ nm. All the loops show large remanence indicating that the Ni structures have an out-of plane easy axis. For these structures, the perpendicular anisotropy constant K_p is positive with $K_{p,s}(4nm) = 2.2\ 10^5$ J/m^3 and $K_{p,d}(4nm) = 2.0\ 10^5$ J/m^3; $K_{p,s}(3nm) = 2.3\ 10^5$ J/m^3 and $K_{p,d}(3nm) = 2.1\ 10^5$ J/m^3. This fact suggests that δ_p should be approximately constant.

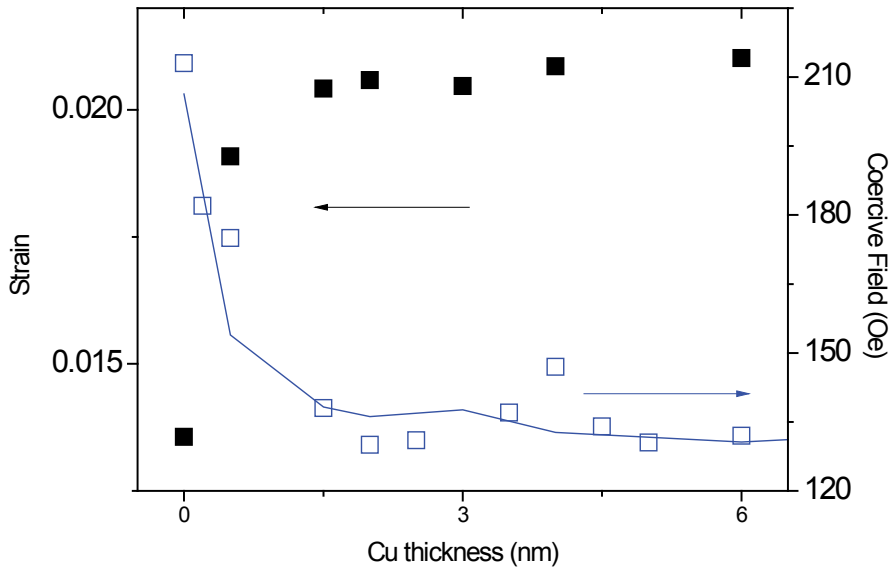

Figure 32: H_c and in-plane strain for a series of Ni/Cu/Ni layers as a function of t_{Cu}

H_c shows remarkable differences: for the structures with $t_{Ni} = 3$ nm $H_c \approx$ 120 $\pm$ 5 Oe, while if $t_{Ni} = 4$ nm, H_c is much larger for the single film (H_c =220 $\pm$ 20 Oe) than for the double film (H_c = 130 $\pm$ 5 Oe). The lack of increment of a quantity usually associated to the increment of the density of defects (threading dislocations) suggests that the preparation process inhibits the propagation of dislocations through the second Ni block. On the other side, the presence δ_p appears in Eq. (12) and (13) may also reveal the presence of a magnetic mechanism that modifies the interaction range between defect and domain wall.

DISCUSSION

To justify the use of the rigid wall approximation and Eq. 13, it is consider that the small value of the nickel layers preclude the formation of significant bowing perpendicular DW plane. Also, in plastically deformed single crystal of Ni [18], it has been shown that in the low defect range investigated in this paper, $H_c \propto \rho^{1/2}$ holds. Thus, the expression given in Eq. 13 is used to discuss the observed behaviour of H_c.

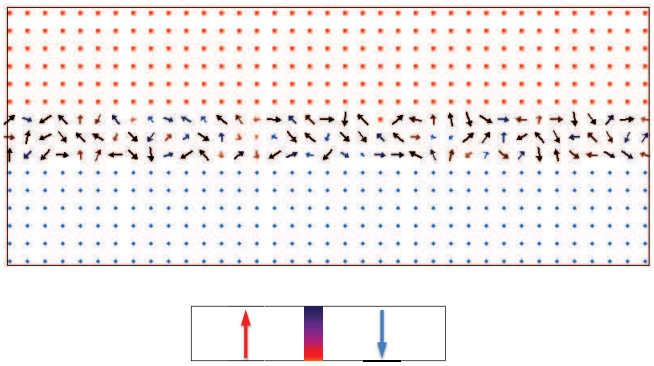

Figure 33: Geometry and initial configuration used to calculate the DW width

Domain Wall Width

First, we discuss the variation of δ in single and double films to determine H_c. The reduction of H_c in permalloy-silicon multilayers with respect to the value observed in the thin films [12] has been qualitatively explained attending to the nucleation of coupled Néel DW in double films, with lower energy and larger width than the Bloch DW existing in single films [19, 20]. The domain walls structure in Ni nanostructures is estimated using a Landau-Lifshitz-Gilbert micromagnetic solver [21]. A rectangular element (with dimensions $L_x = 1000$ nm and $L_y = 400$ nm) with periodic boundary conditions along the x direction. Typical Ni material parameters were used: saturation magnetization M_s= 4.90 10^5 A/m and A = 0.8 10^{-5} J/m, while K_p = 2.2 10^5 J/m^3, a value within the range of the experimental values obtained for the structures studied here. The element, divided in two domains with perpendicular M and a central strip, corresponding to the DW, is set with random orientations of M, see Fig. 33. This configuration is used as the starting point in the simulation. Since the DW volume is small compared with volume of the simulation specimen and does not move from the initial position, the decreasing magnetic energy δE can be assigned to a change in the domain wall energy. Once the DW is stable Δ, we define its thickness as $\delta = 2\ \Delta$, where Δ is the distance from the center of the DW to the points at which M_z is 90% of the saturation value in each domain. Figure 34.(a) shows the variation of δ for Ni and Ni/Cu(3 nm)/Ni structures as a function of nickel block thickness.

The domain wall width decreases as t_{Ni} increases for films and tends to a constant value in the case of the double films. The calculation of δ shows differences for single and double films: δ is larger for the double films than for the single films above $t_{Ni} \approx 3$ nm, although the change is size is minute, 2 nm for $t_{Ni} = 4$ nm, less than 5%. The energy of these DWs for structures with nickel blocks thicknesses smaller than 4 nm is in the range of 4.5 mJ/m^2,

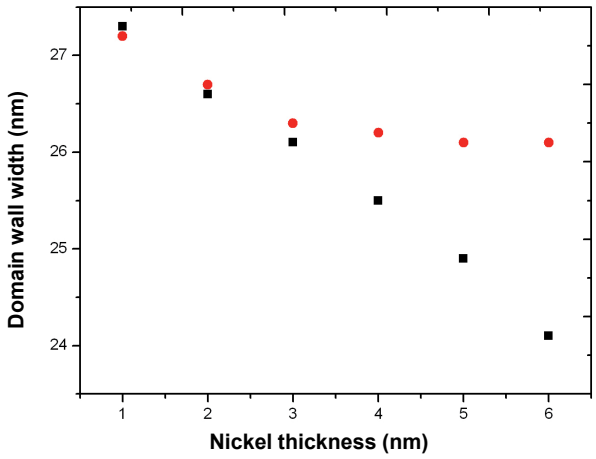

Figure 34: Domain wall width for Ni films (squares) and Ni/Cu/Ni structures (circles)

smaller that the theoretic value obtained for a Bloch wall (~ 6 mJ/m^2). Thus, although the domain width decreases in double films with respect to the single film values, that variation looks to be small to justify the observed decrement of H_c.

Dislocations in thin films

In thin films, the relaxation of the epitaxial strain is associated to the glide of threading dislocations at the interface between two materials: existing dislocations of the substrate initially moves to the surface without altering the seed structure and lattice parameter, but above a critical thickness t_c the dislocation line moves parallel to the interface, adding or taking out a plane of the thin film that faces a substrate plane, see Fig. 35. As a result, the averaged elastic energy of the film decreases and a linear defect is introduced into the thin film [22].

Magnetically, increasing the density of linear dislocations brings about an increasing of the coercivity. In Fig. 31 the dependence of the coercive field *vs.* the thickness of a nickel film grown on a Cu(001) single crystal shows that above t_c, H_c clearly increases reaching a relatively stable value; the low value of H_c for $t_{Ni} < t_c$ indicates the high perfection of the Cu(001) substrate.

For the system under study, a heteroepitaxial Cu-Ni structure with a misfit $\eta = 0.025$, the critical thickness for the generation of misfit dislocations is 1.3 nm for uncapped Ni films and about 2.7 for films with a capping layer. Therefore, ℓ in Eq. (13) includes misfit ℓ_m and threading ℓ_{th} segments and

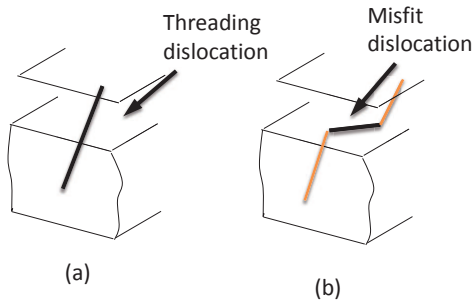

Figure 35: Generation of a misfit dislocation segment from a dislocation line that initially extends from one specimen surface to the other.

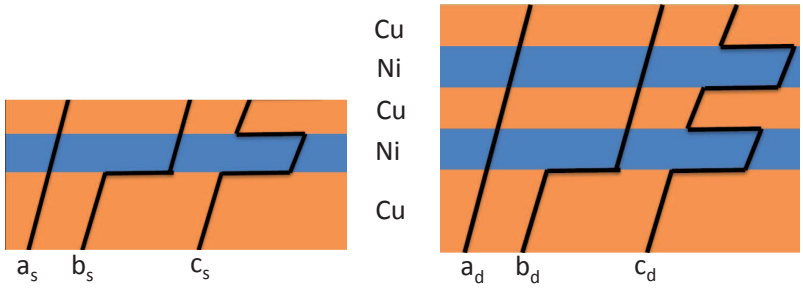

Figure 36: Sketch for the three different scenarious for the propagation of a threading dislocation in single and double Ni films.

both of them can pin the domain wall. While ℓ_{th} goes with the total film thickness, L_z because the dislocation has to end at the film surface, ℓ_{th} may be different depending on the layer structure:

- Large strain without misfit dislocations (see Fig 36 case a). If the strain relaxation is small, $\ell_{th} >> \ell_m$ and the ratio ℓ_{th}/L_z will not change if the film structure is doubled. Therefore H_c remains with the value due to defects existing in the copper buffer layer and transmitted to the Ni/Cu/Ni structure and H_c(single) = H_c(double).

The generation of misfit dislocations to relax the elastic energy of the film is a complex issue. Here we only introduce the extreme situations.

- Relaxation by single kinks (see Fig 36 case b). In this case MD appear only in the first Ni-Cu interface. The interfaces of the second Ni films does not undergoes the propagation of the dislocation along the interface, see Fig. 35, also if $\ell_{md} >> \ell_{th}$ the pinnig of the wall in the single and double film is done by the same defect, and because the domain wall in two times larger in the double film we have H_c(single)=H_c(double)/$\sqrt{2}$.

If ℓ_{th} is different at the interfaces of the second Ni block by a factor γ <2, $\rho_s = \gamma\rho_d$ and the H_c ratio will be equal to $\sqrt{\gamma}$.

- Relaxation by double kinks (see Fig 36 case c). Here symmetric distributions of MD are at the Cu-Ni interfaces. In this case, segments in both films are identical and doubling the domain area also doubles the dislocation length, H_c(single)=H_c(double).

The single-kink model implies the capping layer acquires some strain (of the opposite sign to the layer) whereas the double-kink model implies the capping block remains unstrained. We note that the 4 nm thick Ni film is strongly distorted, the copper grown on top of a layer with a lattice parameter quite close to the Cu bulk value implying small gain in elastic energy that may be not large enough to favors the formation of double kinks. Thus, the next layer of Ni grows onto a Cu layer with smaller lattice parameter than the bulk value, because this layer of copper is not completely relaxed, and the critical thickness for the formation of MD increases.

Comparing this model with with the experimental values, for t_{Ni}= 3nm, H_c(single)/H_c(double) = 1 while for t_{Ni}= 4 nm H_c(single)/H_c(double) = 1.5, close to $\sqrt{2}$. This model yields that for the latter structures the distribution of MD is asymmetric and dominates the pinning mechanism while for the structures with 3 nm thick Ni blocks the dislocation segments have similar structure for the Ni block.

References II

[1] H. Hellwig, T. L. Kirk, J. B. Kortright, A. Berger, and E. E. Fullerton, Nature Mater. **2**, 112 (2003).

[2] S. Mangin, D. Ravelosona, J. A. Katine, M. J. Carey, B. D. Terris, and E. E. Fullerton, Nature Mat. **5**, 210 (2006).

[3] *Mathlab Reference Guide* (Math lab, 2010).

[4] A. Segmüller and A. E. Blakeslee, J. Appl. Cryst. **6**, 19 (1973).

[5] D. Navas, C. Nam, D. Velazquez, and C. A. Ross, Phys. Rev. B **81**, 224439 (2010).

[6] H. J. G. Draaisma and W. J. M. de Jonge, J. Appl. Phys. **62**, 3318 (1987).

[7] H. Barkhausen, Phys. Z **20**, 401 (1919).

[8] G. Bertotti, *Hysteresis in Magnetism* (Academic press, 1998).

[9] H. Hilzinger and H. Kronmüller, J. Mag. Mag. Mat. **2**, 11 (1976).

[10] L. J. Dijkstra and C. Wert, Phys. Rev. **79**, 979 (1950).

[11] R. Labusch, Crys. Latt. Def. **1**, 1 (1969).

[12] H. Clow, Nature **194**, 1035 (1962).

[13] L. Thomas, M. G. Samant, and S. S. P. Parkin, Phys. Rev. Lett. **84**, 1816 (2000).

[14] W. S. Lew, S. P. Li, L. Lopez-Diaz, D. C. Hatton, and J. A. C. Bland, Phys. Rev. Lett. **90**, 217201 (2003).

[15] K. Fukumoto, W. Kuch, J. Vogel, F. Romanens, S. Pizzini, J. Camarero, M. Bonfim, and J. Kirschner, Phys. Rev. Lett. **96**, 097204 (2006).

[16] D. S. Fisher, Phys. Rep. **301**, 113 (1998).

[17] W. L. O'Brien, T. Droubay, and B. P. Tonner, Phys. Rev. B **54**, 9297 (1996).

[18] H. Rieger, Phys. Stat. Sol. **8**, 755 (1965).

[19] J. C. Slonczewski, J. Appl. Phys. **37**, 1268 (1966).

[20] E. Feldtkeller, J. Appl. Phys. **39**, 1181 (1968).

[21] M. Donahue and D. Porter, *OOMMF Users Guide, Version 1.0* (National Institute of Standards and Technology, Gaithersburg, 1998).

[22] J. H. Matthews, Phil. Mag. **13**, 1207 (1966).

Chapter III

Magnetic Domain Structure on a Fe Wedge

Introduction

Ultrathin epitaxial ferromagnetic films have shown a rich variety of magnetic properties that are extremely sensitive to the crystallographic structure, temperature, contamination level, and surface quality [1]. One of their unconventional features is the film thickness dependence of the spin reorientation transitions between in-plane and perpendicular to the plane directions [2, 3, 5]. In these systems, the easy magnetization direction is the result of the competition between the large perpendicular uniaxial anisotropy (originated by the film surface [5]) or the magnetoelastic coupling [6], and the shape anisotropy [3].

Fe is a complex and widely studied magnetic material. Because of the magnetic interaction, at room temperature bulk Fe crystallizes in a ferromagnetic body centered cubic (bcc) structure (α-Fe) and exhibits a phase transition to a face centered cubic (fcc) phase (γ-Fe) at 1184 K, which is stable up to 1665 K. Above this temperature, iron transforms back to the bcc phase (δ-Fe), which remains stable up to the melting temperature (See Fig. 37). The preparation of Fe thin films on fcc substrates as Ag(100) and Cu(100) due to the similar values of their lattice constants (a_{Cu} = 3.615 Å, a_{Ag} = 4.09 Å) with the extrapolated value of the fcc Fe lattice parameter at room temperature (a_{fcc-Fe} = 3.58 Å) favors the epitaxial growth of the γ phase at low thickness of iron. For Fe/Cu(001) films grown at room temperature (RT), three different regimes have been identified regarding the structural and magnetic properties. Firstly, a ferromagnetic (FM) phase with perpendicular magnetization (Regime I) for iron thicknesses below $\approx$ 4 monolayers (ML) occurs. Secondly, an antiferromagnetic (AF) phase covered by a FM surface *live layer* with a magnetization direction normal to the film plane (Regime II) for t_{Fe} between 5 and 10 ML appears. For these regimes tetragonally distorted fcc (fct) is present mainly in regime I and fcc(100) in regimen II. Finally, films thicker than 11 ML show in-plane magnetization (regime III) at the same time that a martensitic phase transition from fcc to bcc [5, 7–9].

In addition, four different complex surface reconstructions have been found for the different regimes with increasing film thickness [10–12]: In the regime I, a (4×1) structure around 2 ML and a (5×1) structure around 4 ML were observed. Then, correlated with the structure change to the regime II, a (2×1) structure above 5 ML appears. Finally, at 11 ML (regime III) there

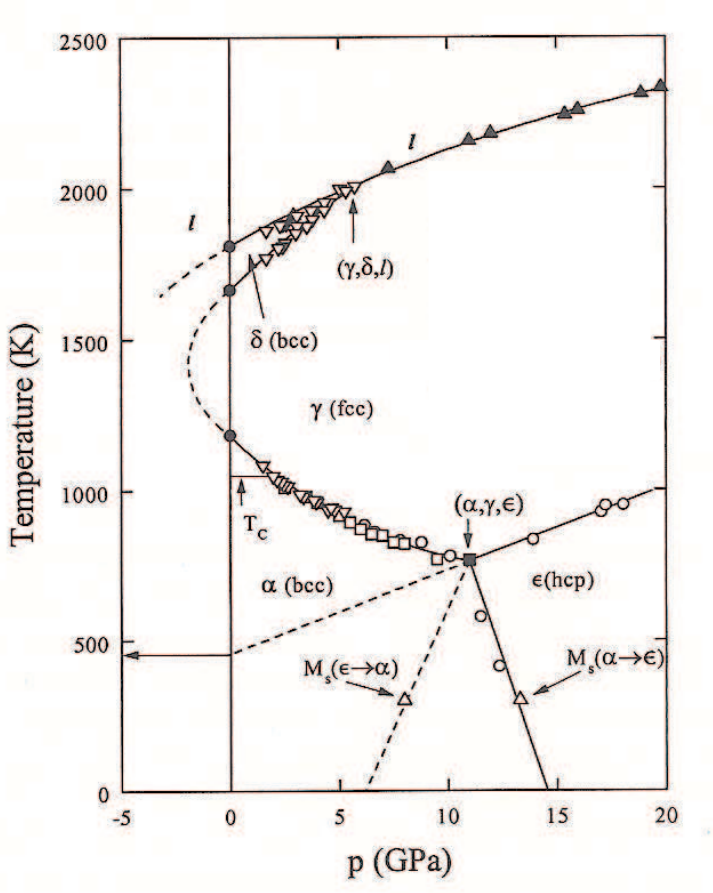

Figure 37: Phase diagram as a function of the temperature and pressure for bulk iron.

are four symmetrically equivalent arrangements of the bcc(110) structure on the fcc(100) substrate, see Fig 38.

It is worth mentioning that the magnetism and structure of Fe films have been extensively studied using techniques such as: low energy electron diffraction (LEED) - Auger [7, 11–14], scanning tunneling microscopy (STM) [11, 15], spin-resolved secondary-electron emission spectroscopy (SPSEES) [5], reflexion high energy electron diffraction (RHEED) [9, 16], surface magneto-optic Kerr-effect (SMOKE) [5, 9, 17], ion beam triangulation [7] and scanning electron microscopy with polarization analysis (SEMPA) sensitive to the perpendicular magnetization component [18]. However, as far as I know, studies of the domain structure in films grown at room temperature have not been reported.

Below, the in plane domain microstructure in Fe/Cu(001) system is presented. Wedge-like films with varying Fe coverage have been prepared by using electron beam evaporation in ultra high vacuum and afterward measured by

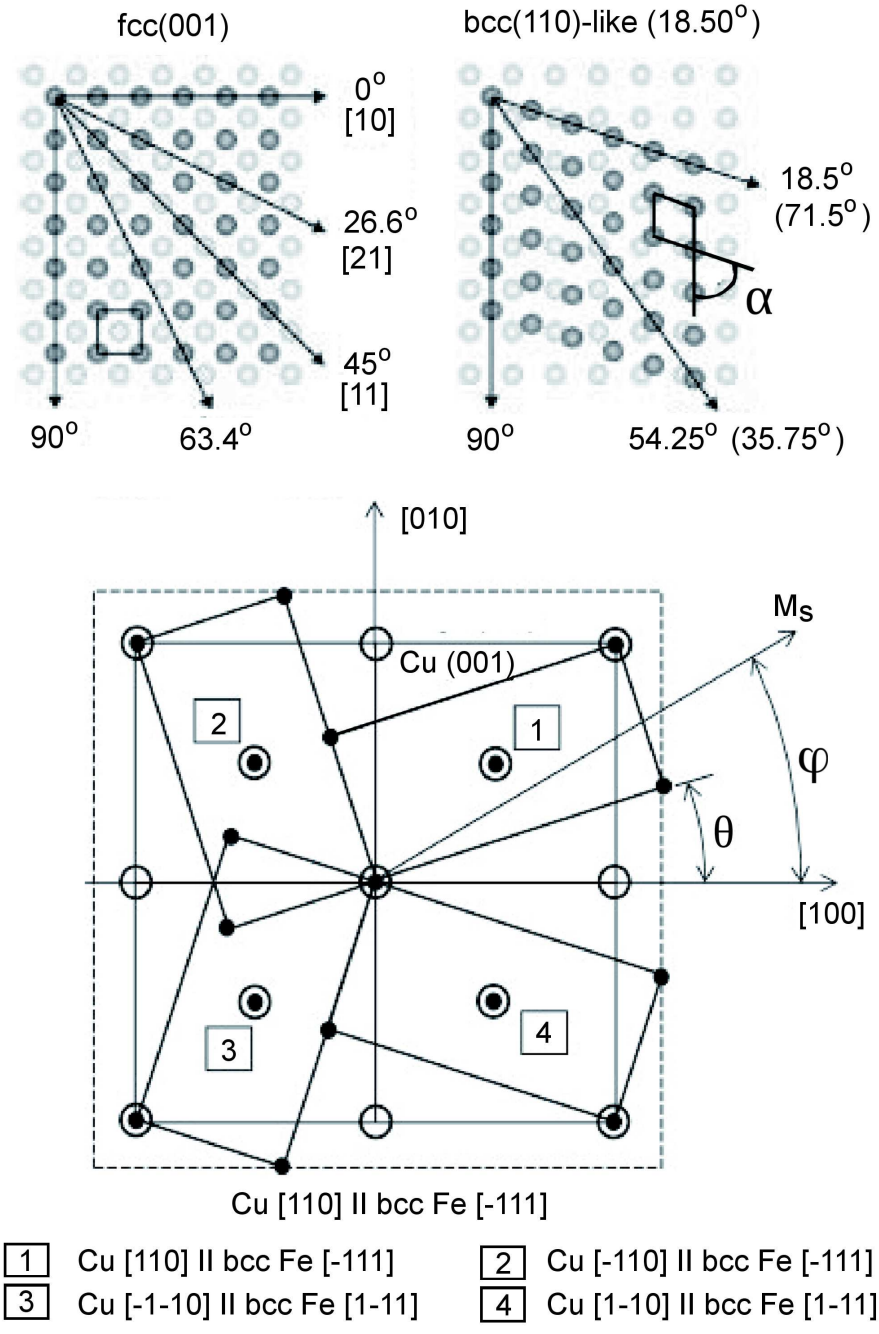

Figure 38: At top: Pictorial representation of the distribution of Fe atoms on a Cu(100) crystal forming a fcc and bcc layer. At bottom: Sketch of the four possible orientations of a Fe(110) crystallite on a Cu(100) surface with the Fe<111> Cu <110> directions parallel to each other.

SEMPA. Two different behaviors were found: On the one hand, for t_{Fe} lower than about 11 ML, a strip was observed in a region without magnetic contrast, and the other hand, above 11 ML of iron the transition from fcc(100) to bcc(110) phases is related to the magnetic domain structure.

EXPERIMENTAL DETAILS

Ultrathin Fe films with thicknesses between 0 and 22 ML have been grown by e-beam evaporation onto a Cu(100) single crystal at room temperature in ultra-high vacuum. The base pressure was in the range of 2×10^{-10} mbar and during the deposition raised to 6×10^{-10} mbar. Before each experiment, the Cu(100) substrate was cleaned by repeated low energy (500 eV, 1μA) Ar^+ ion bombardment at room temperature and annealing at 700 ^{o}C for 20 minutes cycles until sharp spots representing a (1×1) surface were observed by low energy electron diffraction (LEED), see Fig. 40(a). Fe was evaporated from a high purity rod at rate of 0.7 ML/min at room temperature. In order to provide a global picture of the Fe system, we use wedge-shaped samples to study the domain structure as a function of the film thickness, as is shown in Fig. 39(a). Scanning electron microscopy with polarization analysis (SEMPA) was used to image the orthogonal in-plane magnetization components at the film surface. The growth chamber is connected to the SEMPA apparatus (working at pressures less than 5×10^{-11}). Therefore, immediately after the Fe growth the samples were transferred and the domain pattern visualized.

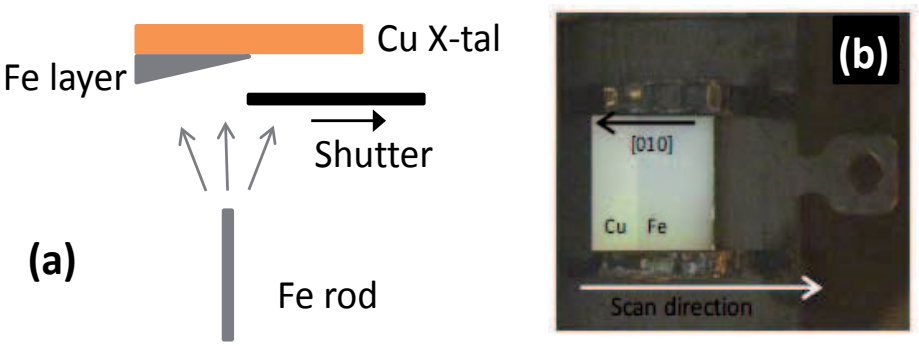

Figure 39: (a) Simplified illustration of the deposition setup. (b) Photograph of the Cu single crystal marked with the crystalographic directions after the deposition of the Fe layers.

General features and magnetic contrast for $t_{Fe} < 4$ML

The LEED patterns shown in Fig. 40(b) and (c) were taken at different positions of the iron wedge. The patterns in Fig. 40(a) and (c) correspond to fcc and bcc phases, while the pattern displayed in Fig. 40(b), taken at an intermediate distance, shows a mix of bcc(110) and fcc(100) structures revealing that the electron beam recovered information from different thicknesses on the wedge because the width of the LEED e-beam (typically 1μm). The complexity of the pattern shown in Fig.40(c) has been explained as the result of the arrangements of the bcc structure on fcc (110) substrates [10, 11, 13] with the Pitsch orientational relationship in which rows of nearest-neighbor atoms are matched between {011} bcc and {001} fcc planes [10]. Thus, it is found that the Fe<111> direction matches the <110> Cu axis and four different variants can be observed. Fig. 38 shows the corresponding variants for the (110)Fe plane on (001)Cu: $[110]_{bcc} \parallel [1\bar{1}1]_{fcc}$, $[1\bar{1}0]_{bcc} \parallel [\bar{1}11]_{fcc}$, $[1\bar{1}0]_{bcc} \parallel [\bar{1}11]_{fcc}$ and $[110]_{bcc} \parallel [\bar{1}11]_{fcc}$. Figure 40 displays a sketch of the reciprocal lattice of a Fe film on a Cu(001) surface showing the $[110]_{bcc}\|[1\bar{1}1]_{fcc}$ variant as it was reported by M. Wuttig *et al* [11]. The ellipses represent the positions of the LEED beams. Open and filled ellipses distinguish the remaining variants. Moreover, in the LEED images the contrast background indicates a low range order of the surface.

Figure 41 shows the SEM image and SEMPA vertical and horizontal polarization component images for the whole Fe wedge. The SEMPA images show no contrast on the left half of the image except for a wire in the vertical channel. The lack of contrast in this region indicates perpendicular magnetization of the iron film. The thickness of the iron film, t_{Fe}, along the wedge was calculated based on the magnetic contrast observed and taken into account a constant flux of deposition of iron on the copper. Thus, based on previous results for the onset of the out-of-plane to in-plane spin reorientation [7, 9, 10], we have taken 11 ML for the x coordinate where the magnetic contrast shows up in Fig. 41(b) and (c). Another interesting fact is the observation of different contrast in the SEM images parallel to the shutter edge (see Fig. 41(a) and Fig. 45). Those differences in the contrast could correspond to the onset of the iron layer and the existence of bcc and fcc crystal structures which will be

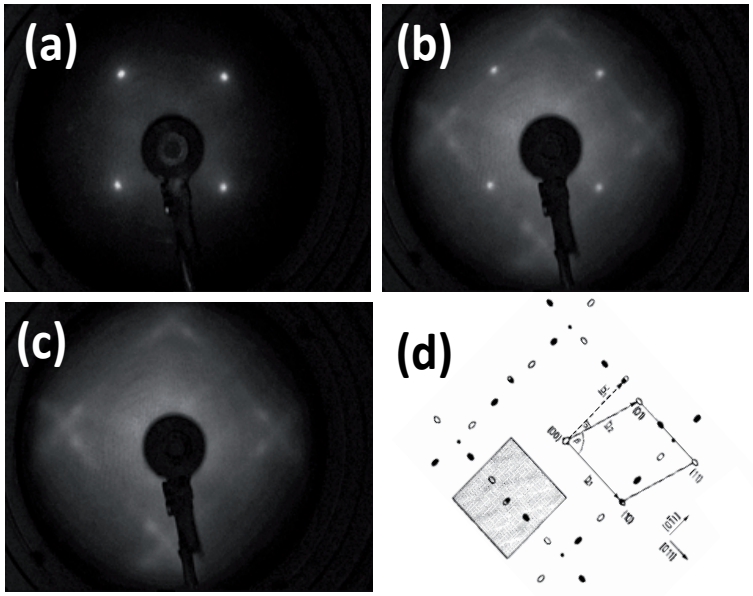

Figure 40: LEED patterns for clean Cu (100)(a) and Fe (b) and (c) films with increasing thickness. The diffraction patterns correspond with a mix of a fcc (100) and bcc (110) phases, and a more defined bcc (110) phase, in (b) and (c) respectively. (E= 233 eV).(d) Sketch from the Wuttig's article.

discussed later.

A strip with magnetic signal inside a non-magnetic area is observed only in the vertical polarization component, see Fig. 41(b), for t_{Fe} between $\approx$ 1.6 and 2.3 ML forming a single domain structure. The domain is along one of the in-plane <001> directions, which is the easy axis of magnetization in Fe bulk. The width of the line is $5\mu m$. We note that, for iron films in this range of thicknesses, in-plane magnetization has not been reported for Fe films grown by thermal deposition (TD), although the magnetic phase diagram as a function of the growth temperature reported by D. Liu *et al* [5] shows a weakening of the perpendicular anisotropy for temperatures larger than room temperature.

The presence of that strip can be understood considering the work of O. Portmann *et al.* [18]. This group has reported an anomalous variation of T_c with t_{Fe} for small values of t_{Fe}: T_c peaks at t_{Fe} = 2.1 ML with a value of $\approx$ 320 K, being 1.8 ML the threshold of thickness for with which $T_c >=$ 300 K (see Fig. 2(a) of Portmann's reference). We note that the interval of t_{Fe} for which T_c is larger than room temperature reported in the above reference is in excellent agreement with the values calculated for the strip observed in Fig. 41.

However, an important fact in the magnetic behavior of this system is related with different regimes regarding the structural properties for Fe films

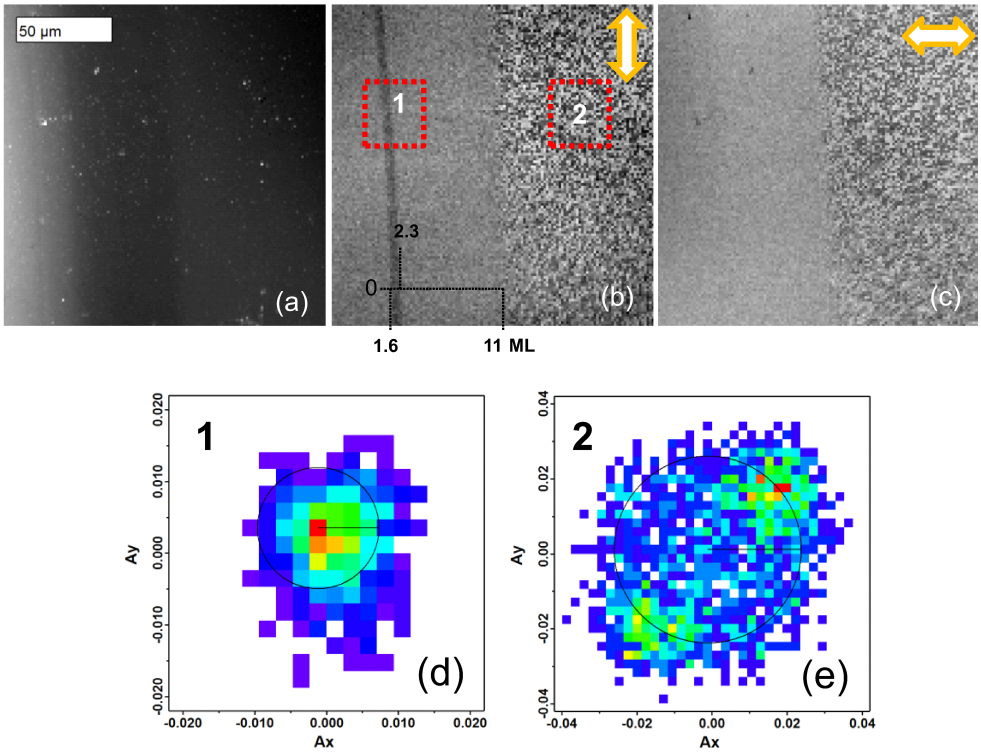

Figure 41: Magnetic domain structure on a Fe wedge. (a) SEM image on the same region as in (b) and (c). The SEMPA images show the distribution of the (b) vertical and (c) horizontal polarization components. (d) and (e) display the histogram of polarization of the strip region (1) and in-plane domains region (2), respectively. The polarization values are 1% in (d) and 2.6% in (e).

grown at room temperature [7, 9, 12]. Although in general there is a consensus about the crystallographic structure for films thicker than 4ML, for thinner Fe films the structural properties seem to be strongly dependent on the growing conditions and technique used, providing films with different magnetic behavior [16, 20]: **M** in-plane for films grown by PLD and perpendicular for films with grown by thermal evaporation. Therefore, the occurrence of a ferromagnetic island with in-plane contrast inside of a paramagnetic sea could be explained for small variations of the structural properties of the Fe films.

We observe a reduction of the spin polarization on the iron films, thus, the SEMPA polarization value of the strip is 1% [see Fig. 41 (d)] increasing up to 2.6% at larger thickness [see Fig. 41 (e)]. These values are comparable with those obtained by T. Bernhard *et at* [7] for equivalent thickness. In fact, it was found that the polarization value saturates at $\approx$ 17 ML of Fe thickness. The loss of spin polarization has been observed for Fe films with in-plane magnetization by D. P. Pappas et al. [5], and Allenspach et al. [3]. In both

cases, the in plane magnetization in Fe/Cu (001) films saturates at $\approx 35\%$ of the bulk value, which is considerably lower than the perpendicular polarization of about $\approx 50\%$ [5].

On the one hand, Pappas et al., have argued that the decrement of the spin polarization would be consistent with a reduction of $\approx 25\%$ of the magnetic moment in this range of t_{Fe}, where the value of T_c is considerably smaller that the bulk value. On the other hand, Allenspach et al. disagree with the last claim and suggest that the reduced remanence magnetization, M_r, is a consequence of the structural transition from a tetragonally distorted to a more complex phase.

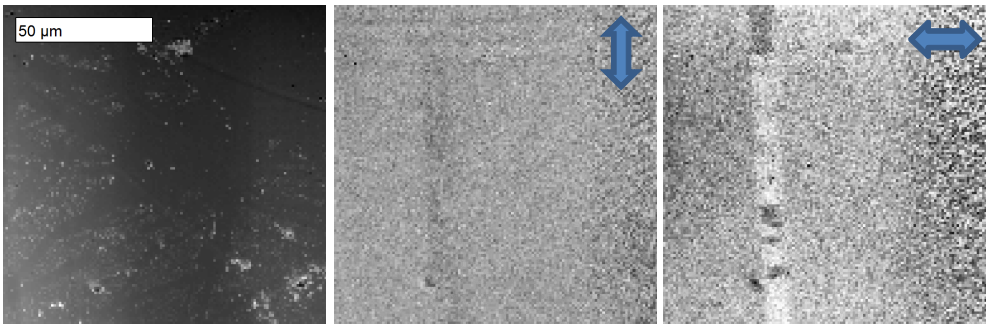

Figure 42: SEMPA domain images after three days on the same region as in Fig. 41. The strip breaks into big domains oriented on the [010] direction.

In addition, after three days, the stripe in Fig. 41 breaks into big domains oriented on the [010] direction as it is shown in Figure 42. Notice that, the domains are visible in both channels and the signal is even stronger in the parallel one. The width of the line is 7.2 μm and the domain size (vertical white zone) is $\sim$ 30 μm. These elongated domains in one direction suggest an anisotropy within the film plane. Time dependent magnetization has been observed before in Fe stripes grown on Cu (111) [21] where the remanent magnetization after saturating the sample decays slowly. However, the reasons why the single domain state is broken at lower iron thickness after some days is still unclear for us and may involve a weak contamination of the sample by residual gases of UHV chambers.

SPIN REORIENTATION TRANSITION, FE FILMS ($t_{Fe} >$ 11 ML)

Figure 43 shows a general view of the magnetic domain structure for a Fe wedge with thicknesses ranging from $\approx$ 11 to 20 monolayers from the left to the right. It is clear that the domain size increases with t_{Fe}. The histogram of polarization shows that there is a preferred orientation of the **M** that could be understood if an uniaxial magnetic anisotropy is present in the film. Notice that, in this case the radius of the SEMPA spin polarization is 3%, a larger value than that observed for the strip.

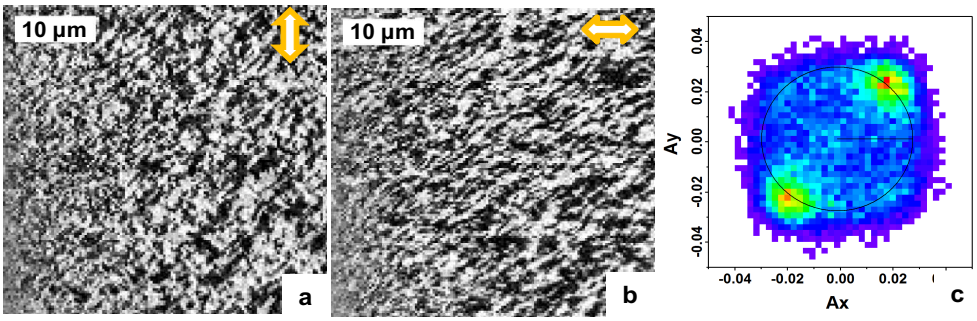

Figure 43: In plane magnetic domains of a Fe wedge. The thickness is increasing from the left to the right (from $\approx$ 11 ML to 20 ML). (a) Perpendicular and (b) parallel SEMPA magnetization components. (c) Histogram of the spin polarization.

Figure 44 shows the domain structure for a region near the transition from perpendicular to in-plane magnetization with t_{Fe} between $\approx$ 11-13 ML. The domains are forming entwined ribbons with **M** in antiparallel orientation between neighbor domains. The average domain size is 670 nm and 1350 nm for the vertical and horizontal component, respectively. The histogram of polarization suggests the presence of an uniaxial magnetic anisotropy. Remarkably, this finding could be explained as the result of the weakening of the perpendicular anisotropy and the generation of a canted domain structure with alternating in-plane components from the stripe domain structure; nevertheless magnetization measurements show that the spin reorientation transition is not mediated with intermediate orientation of **M**.

On the other hand, on the region with the uniaxial anisotropy, the close

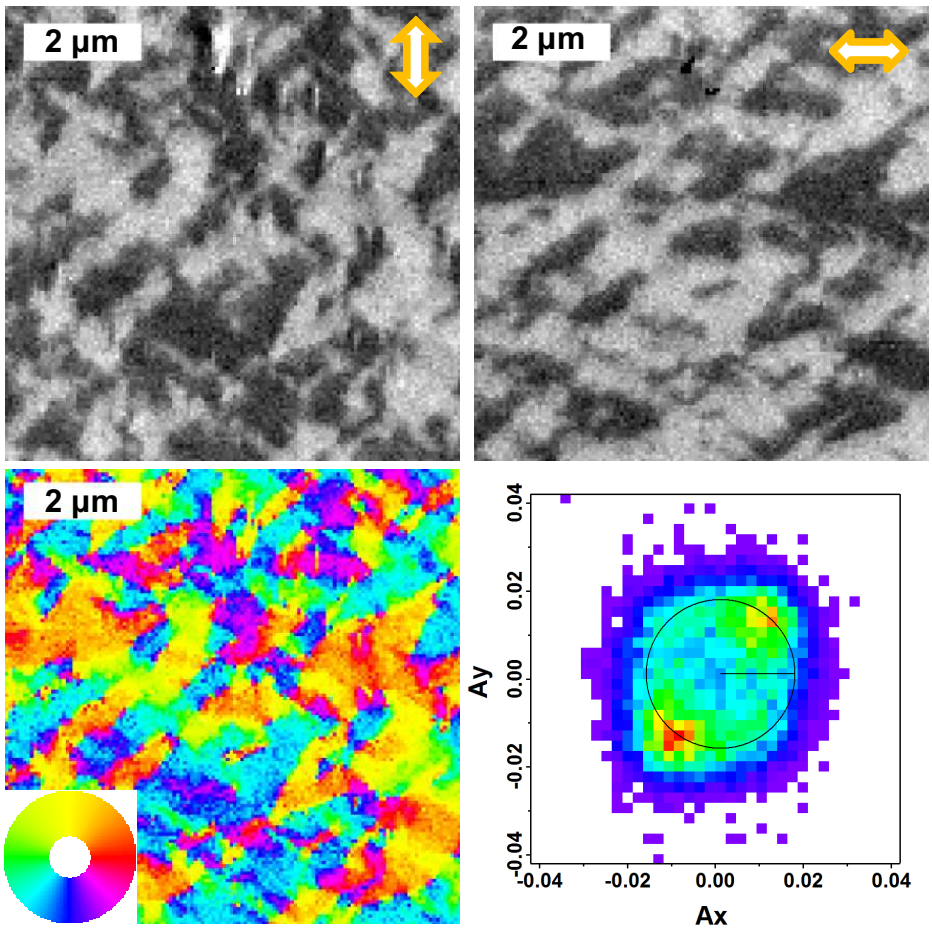

Figure 44: Domain pattern near the transition region at $t_{Fe} \approx$ 12-13 ML. The upper plots correspond with the vertical, on the left, and horizontal, on the right, polarization components. The lower plots are: the in-plane magnetization pattern, on the left, and the histogram of the spin polarization, on the right.

examination of the SEM images reveal a correlation between the structure and the magnetic images. Back-scattered electron, Fig. 45(a), and secondary electron images, Fig. 45(b) and (e), show areas with two different tones at the transition region where the fcc to bcc phase transformation takes place. Notice that the contrast is inverted in these images. The secondary electron image were collected with the in-lens detector detector(BSE) that shows differences in the work function (e.g., electronic variations) on the sample with high lateral resolution. The contrast in Fig. 45(b) was enhanced to highlight the shape of the areas with different contrast and establishes a correlation between the topographic and the magnetic images. A more detailed view of a portion of the last image is shown in Fig. 45(e) where the dark lines are forming 90 degrees

45 degrees with the horizontal, see arrows. The magnetic contrast in Fig. 45(f) and (g) follows the same orientation that the features observed in the SEM image, although the size of the magnetic domain is larger. This shows the strong relation between the crystallographic phases and the magnetic domain structure of Fe films on the transition region.

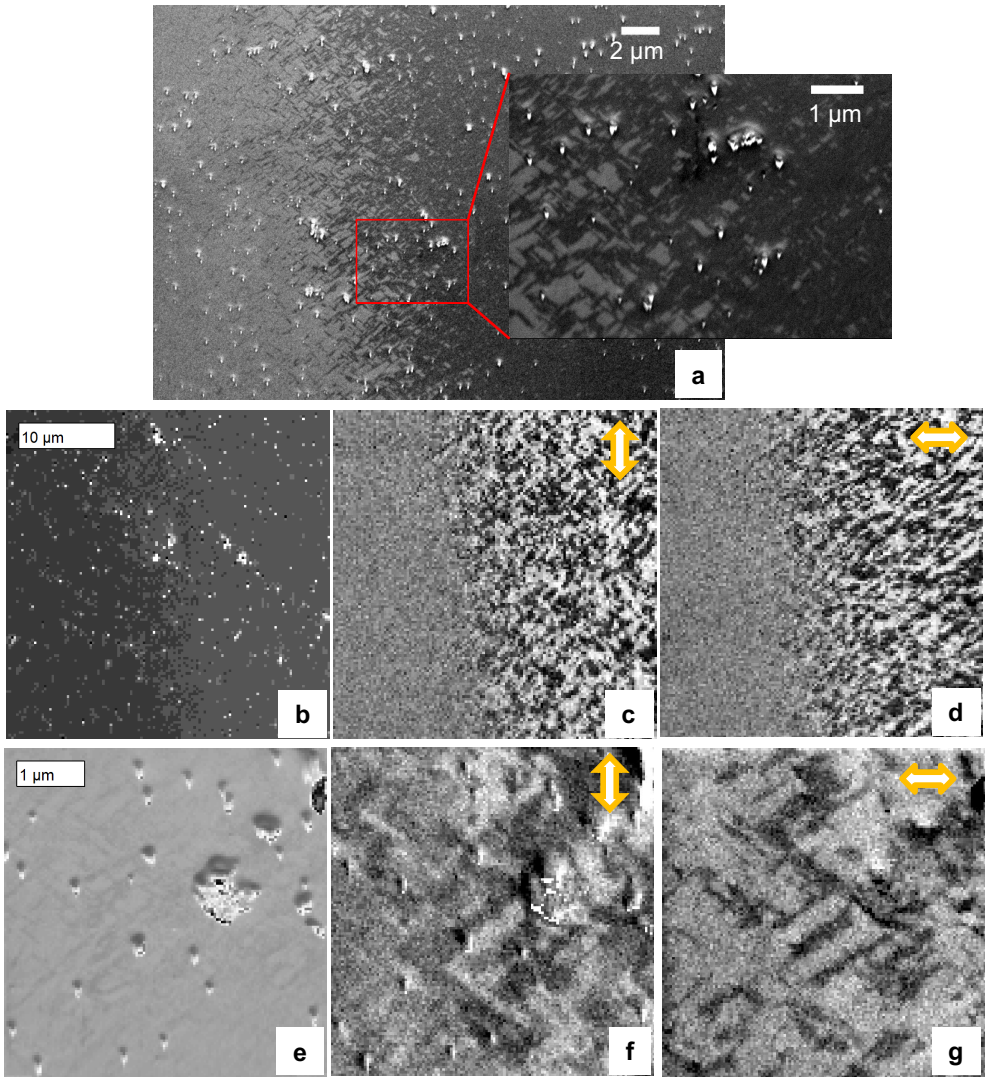

Figure 45: Contrast phases and magnetism of Fe films on Cu(100). (a) SEM image on the transition region using back-scattered electrons. (b) and (e) SEM images using secondary electrons. (c - d) and (f -g) magnetic domain microstructure in the same region as in (b) and (e), respectively.

Fourfold symmetry is observed in the SEMPA histogram when t_{Fe} increases, as it is shown for $t_{Fe} \approx$ 14-15 ML in Fig. 46. In this case the domains follow a preferential alignment at around 45 degrees with the horizontal line

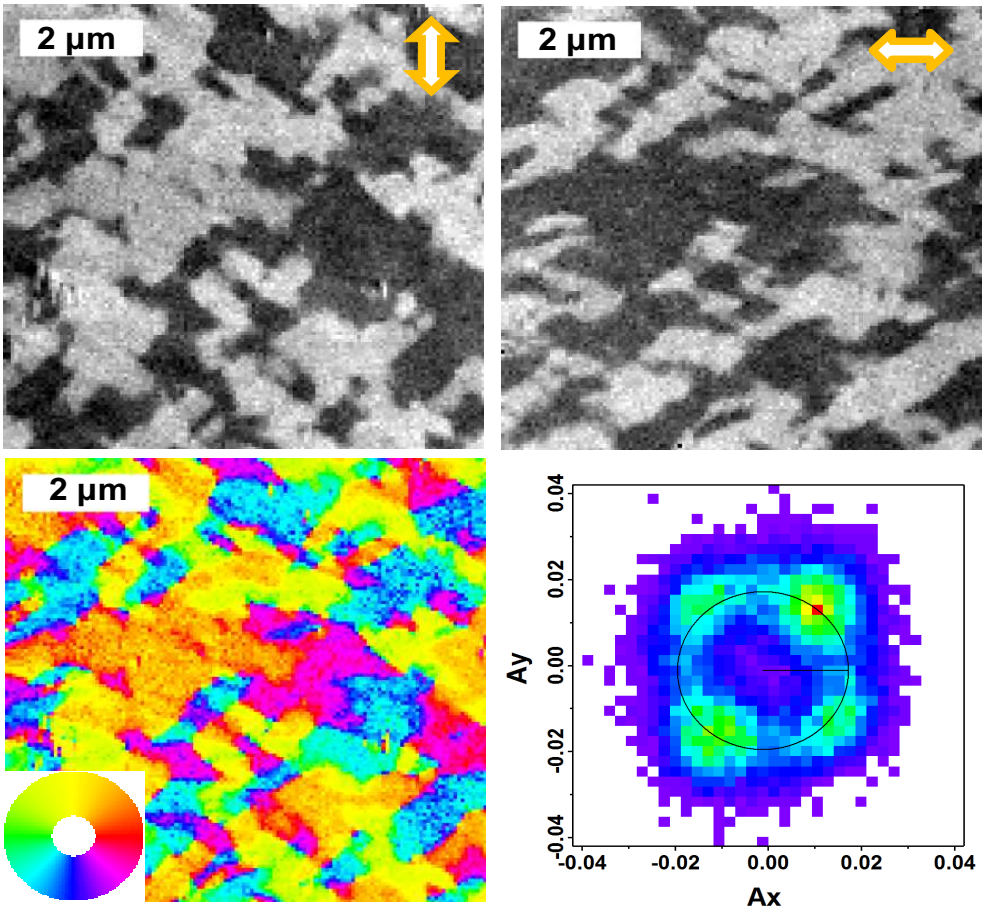

Figure 46: In-plane Fe domains show fourfold symmetry at $t_{Fe} \approx$ 14-15 ML. The upper plots correspond with the vertical, on the left, and horizontal, on the right, polarization components. The lower plots are the in-plane magnetization pattern, on the left, and the histogram of the spin polarization, on the right.

that corresponds to the <110> Cu direction, and further, taking into account the crystallographic orientation of the Fe variants (Fig. 38), to the <111> or $<11\bar{2}>$ bcc Fe directions. The sign of the magnetocrystalline anisotropy constant ($K_1 > 0$) indicates that these directions are magnetically hard while the <100>direction is the one of minimal energy. The angles that form <100>Fe and <110> Cu directions are 55^o, and 35^o, depending on the variant considered (see Fig. 38). Therefore, another magnetic anisotropy looks to be present in iron film.

In addition, by evaluating the magnetic domain dimensions in Fig. 44 and Fig. 46, we note that the domain dimensions change their values with t_{Fe}. For the image taken at the position with thinner iron layer (Fig. 44), the typical values for the vertical and horizontal dimensions are 670 nm and 1350 nm,

respectively, while, for the thicker region (Fig. 46), the average sizes are 1600 nm and 670 nm for the vertical and horizontal components. The radius of spin polarization is $\approx 1.8\%$ in both cases.

MAGNETOELASTIC MODEL

To justify the use of the ME energy for this system we discuss the presence of residual strain in the Fe(110) layer. The occurrence of the orientation relationships between the Cu(001) and Fe(110) planes is obtained using the concept of invariant line than corresponds to a crystal line that remains unrotated and unstretched during a crystal transformation [10, 22]. For the Cu-Fe system the invariant line corresponds to <111> directions. Thus, along a <111> direction of the unit cell the atoms of Fe and Cu are aligned, see sketch Fig. 38.

This matching introduces a shear strain in the Fe layers along the <111> direction as is observed by the measurement of the angle between the two <111> direction located in the (110) plane done by grazing scattering of fast H and He atoms or ions [7] and LEED [11]. The strain becomes anisotropic in the Fe(110) unit cell and inside each variant but, from the point of view of the whole Fe film, it has a fourfold symmetry because the distortion in the bcc domains is linked to the Cu(100) plane. The misfit between Cu[110] and Fe [111] is 2.7%, meaning that a thin iron film will expand along this direction to adapt itself to the Cu lattice. The inverse magnetoelastic effect suggests that this [111] direction becomes a magnetically hard direction since the magnetoelastic stress is positive [21] (i.e., **M** moves to the compressed direction), as it is shown below. To describe the ME contribution to the total anisotropy energy e_{anis} in each crystallite forming the iron film, due to the strain, we start considering the ME energy for a cubic symmetry, given by:

$$\begin{aligned} e_{mel} &= B_1 \left[\left(\alpha_z^2 - \frac{1}{3} \right) \left(\epsilon_{zz} - \frac{\epsilon_{xx} + \epsilon_{yy}}{2} \right) + \frac{1}{2} \left(\alpha_x^2 - \alpha_y^2 \right) \left(\epsilon_{xx} - \epsilon_{yy} \right) \right] \\ &+ 2B_2 \left(\alpha_x \alpha_y \epsilon_{xy} + \alpha_y \alpha_z \epsilon_{yz} + \alpha_z \alpha_x \epsilon_{zx} \right) \end{aligned} \tag{14}$$

First term on Eq. 14 is equal to zero, while for a shear strain along the [111] direction $\epsilon_{xy} = \epsilon_{yz} = \epsilon_{zx} = \epsilon_0$. Then, the ME contribution to magnetic anisotropy energy can be written as:

$$e_{mel} = 2B_2 \epsilon_0 \left(\alpha_x \alpha_y + \alpha_y \alpha_z + \alpha_z \alpha_x \right) \tag{15}$$

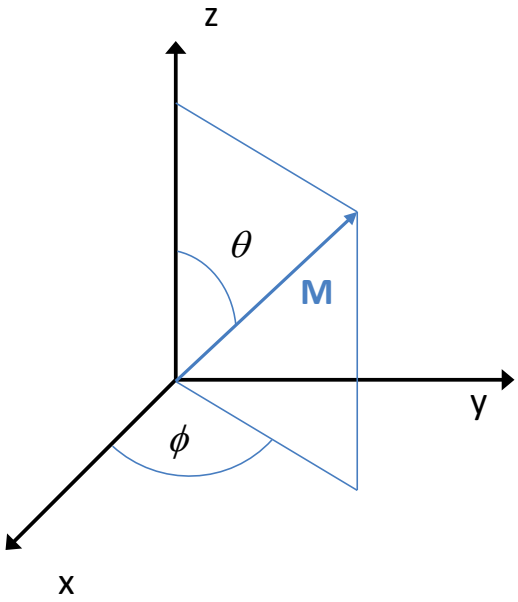

Figure 47: Cartesian coordinate axes and $(\bar{1}\bar{1}0)$ plane ($\phi = 45$ degrees). With this election the shear strain is applied along the [111] direction

For the (110) bcc film, **M** lays the film plane, and the angular dependence of e_{mel} can be obtained projecting e_{mel} to the film plane $(\bar{1}\bar{1}0)$ where **M** forms an angle θ with the [001] direction, see Fig. 47. Thus, the direction cosines of **M** are obtained by fixing $\phi = 45^o$:

$$\begin{aligned} \alpha_x &= \frac{\sqrt{2}}{2}\sin\theta \\ \alpha_y &= \frac{\sqrt{2}}{2}\sin\theta \\ \alpha_z &= \cos\theta \end{aligned} \tag{16}$$

Then, e_{mel} can be expressed as:

$$e_{mel} = 2B^{\epsilon,2}\epsilon_0\left(\frac{1}{2}\sin^2\theta + \frac{\sqrt{2}}{2}\sin 2\theta\right) \tag{17}$$

Figure 48 displays the angular dependence of $e_{mel}/2B_2\epsilon_0$, with $B_2\epsilon_0$ positive, showing a clear uniaxial character. The minima are found at $\theta \approx -57.5^o$ and 122.5^o, values that correspond to the $[11\bar{2}]$ directions, i.e., perpendicular to the invariant [111] axis, along which the distortions happen.

We now compare $2B^{\epsilon,2}\epsilon_0$ with K_1. For iron $K_1 = 5.2\times 10^{\,4}\mathrm{J/m^3}$, $B^{\epsilon,2}$= 7.6 $\times 10^6\mathrm{J/m^3}$ [25], therefore for values of $\epsilon_0 < 0.01$ a spin reorientation could be

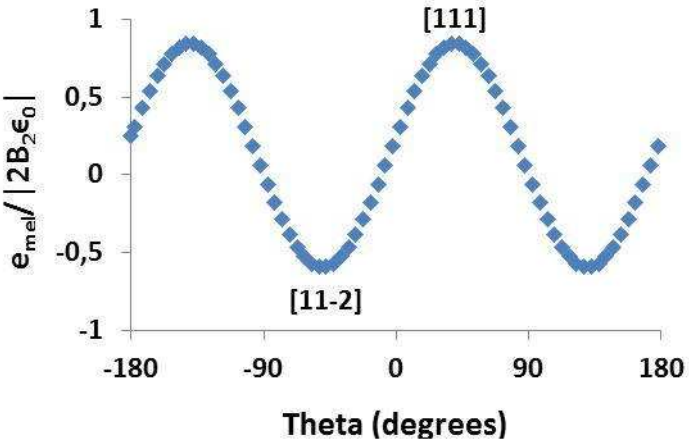

Figure 48: Normalized angular dependence of e_{mel}. An uniaxial character is shown with minima every 180 degrees.

expected since the e_{mel} can overcome e_{mc} for strains larger than 1%, a value, considering the misfit between Fe and Cu of 0.027, reasonable for this system.

So, the fourfold symmetry observed is due to the orientation of the bcc domains with respect to the cubic structure and the strain induced on the iron crystallites.

CONCLUSION

The existence of a magnetic strip at t_{Fe} between $\approx$ 1.6 and 2.3 ML could be explained due to small variations of the structural properties of the Fe films prepared in this work.

A magnetoelastic model was proposed to explain the fourfold symmetry observed at Fe thickness around 15 ML. At that thickness the crystallographic structure corresponds with four types of elongated bcc(110) domains with respect to the cubic structure.

References III

[1] M. T. Johnson, P. J. Bloemen, F. J. A den Broeder and J. J de Vries, Rep. Prog. Phys. 59, 1409 - 1458 (1996).

[2] P. Poulopoulos and K. Baberschke, J. Phys.:Condens. Matter. 11, 9495 - 9515 (1999).

[3] R. Allenspach et al, Phys. Rev. Lett. 69, 3385 (1992).

[4] D. P. Pappas et al, Phys. Rev. B 45, 8169(1992).

[5] C. Liu, E. R. Moog, and S. D. Bader, Phys. Rev. Lett. 60, 2422 (1988).

[6] Gabriel Bochi, Magnetic Anisotropy in Thin Films Ni/Cu(001) MIT PH.D Thesis Repository, 1995.

[7] T. Bernhard et al, Phys. Rev. Lett. 95, 067601 (2005).

[8] H L Meyerheim R. Popescu, D. Sander, J. Kirschner, O. Robach and S. Ferrer , Phys. Rev. B 71, 035409 (2005).

[9] Dongqi Li et al, Phys. Rev. Lett. 72, 3112 (1994).

[10] J. Thomassen, F. May, B. Feldmann, M. Wuttig and H. Ibach, Phys. Rev. Lett. 69, 3831 (1992).

[11] M. Wuttig, B. Feldmann, J. Thomassen, F. May, H. Zillgen, A. Brodde, H. Hannemann and H. Neddermer, Surf. Sci. 291, 14-28 (1993).

[12] S. Müller Phys. Rev. Lett. 74, 765 (1995).

[13] K, Heinz, S. Smuller, P. Bayer, Surf. Sci. 352, 942-950 (1996).

[14] F. Scheurer, R. Allenspach, P. Xhonneux, and E. Courtens, Phys. Rev. B 48, 9890 (1993).

[15] J. Giergiel, J. Kirschner, J. Landgraf, J. Shen and J. Woltersdorf, Surf. Sci. 310, 1-15 (1994).

[16] A. Schatz, S. Dunkhorst, S. Lingnau, U. von HÖrsten and W. Keune, Surf. Sci. 310, L595-L600 (1994).

[17] C. Liu, E. R. Moog, and S. D. Bader, J. Appl. Phys. 64, 5325 (1988).

[18] O. Portmann et al, Nature 422 701-704 (2003).

[19] M. Kato et al., Acta metall. Vol.37, No.3, 749-756 (1989).

[20] H. Magnan et al, Phys. Rev. Lett. 67, 859 (1991).

[21] J. Shen, R. Sjomski, M. Klaua, H. Jenniches, S. Sundar and J. Kirschner, Phys. Rev. B 56, 2340 (1997).

[22] M. Kato, S. Fukase, A. Sato and T. Mori, Acta metall. Vol.34, No.7, 1179-1188 (1986).

[23] R. O'Handley, Modern Magnetic Materials, Massachusetts Institute of Technology. Jhon Wisley & Sons (2000).

[24] R. C. O'Handley, Modern Magnetic Materials: Principles and Applications (John Wiley Sons, 2000).

[25] G. Wedler, J. Walz, A. Greuer, R. Koch, Phys. Rev. B 60, R11313 (1999).

[26] H. Jenniches et al, Phys. Rev. B 59, 1196 (1999).

[27] D. E. Fowler et al, Phys. Rev. B 53, 5563 (1996)

[28] J. Magn. Magn. Mat 31-34, 837-838 (1983).

[29] Zhen Tian, Dirk Sander, and Jürgen Kirschner Phys. Rev. B 7, 024432 (2009).

[30] M. Weinelt S. Schwarz, H. Baier, S. Müller, L. Hammer, K. Heinz, and Th. Fauster, Phys. Rev. B 63, 205413 (2001).

[31] B. Ujfalussy, L. Szunyogh, and P. Weinberger, Phys. Rev. B 54, 9883 (1996).

[32] L. Szunyogh, B. Ujfalussy, and P. Weinberger, Phys. Rev. B 55, 14 392 (1997).

Chapter IV

Structural and Magnetic Properties of Fe/Cu/Ni Films

Introduction

The study of ultrathin films on single-crystal substrates has contributed greatly towards the understanding of surface and interface magnetism. By properly choosing the substrate, film thickness, and growth conditions, different crystalline phases of a magnetic material can be formed [1, 2]. These systems are a very attractive field because of the strong correlation between small changes in the epitaxial film structure and magnetic properties [3].

The metastable fcc structures of Fe have been studied on different substrates. In particular, two ferromagnetic substrates with similar lattice parameters, fcc Co(001) and Ni(001) have been used. The interest is based on investigate how the magnetic moment of the substrates may influence the magnetic moment of the film. By using LEED identical surface unit cells of the three substrates were seen. Thus, it was found that the regions of different magnetic behavior of Fe for growth on Co or Ni nearly coincide with the regions of different crystal structure for Fe growth on Cu. This is strong evidence that Fe has the same growth mode on Cu(001), Co(001), and Ni(001) [1, 4].

While Fe films on Cu(001) are stretched in-plane since the Cu lattice parameter ($a_{Cu} = 3.62$ Å) is larger than that of fcc Fe ($a_{fcc-Fe} = 3.59$ Å), Fe films on Ni(001)($a_{Ni} = 3.52$ Å) are compressed in-plane, and therefore the details of the atomic structure and magnetic behavior are expected to be different in the two systems [3]. The surface anisotropy favors the perpendicular magnetization in Fe/Cu(001) films for thicknesses less than 2 nm [5]. On the other hand, Ni films with thicknesses between 2 and 12 nm have out-of- plane magnetization which arise from the face-centered-tetragonal (fct) distorted crystal structure of Ni on Cu(001). The combination of both Fe and Ni makes the coupled system an interesting case to study the relation between the structure, magnetism, and coupling phenomena of Fe/Ni bilayers on Cu(001) [6]. At present a few investigations have been done in this system regarding to structural and magnetic properties using experimental techniques such as: spin-polarized low-energy electron microscopy (SPLEEM) [6], magneto-optic Kerr effect(MOKE) [7], low energy electron diffraction (LEED) [3, 7], primary-beam diffraction modulated electron emission (PDMEE) [3, 4], photoemission electron microscopy (PEEM) [8, 9], x-ray magnetic circular dichroism (XMCD) [1]. As far as the magnetism concerns, most of the studies have been done at the

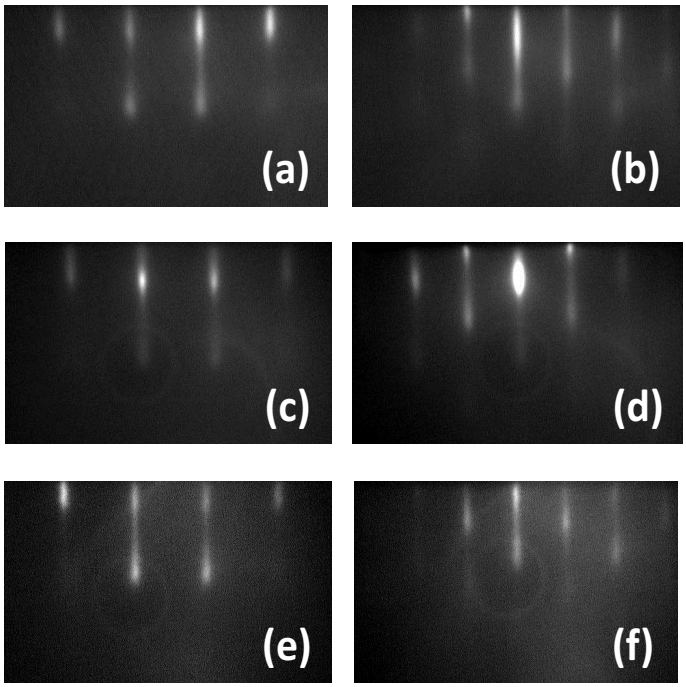

Figure 49: RHEED patterns: for the Cu buffer layer along the (a)[100] and (b)[110] directions, for the Ni layer along the (c) [100] and (d) [110] directions, and for the Cu capping layer along the (e) [100] and (f) [110] directions.

first spin-reorientation transition (SRT) of the Ni system, i.e., around Ni thicknesses of 2 nm in combination with Fe layer thicknesses less than 2 nm. To the best of our knowledge, however, no investigation on the effect of Fe layers on top of the Cu/Ni/Cu/Si system for Ni layers thicknesses near the second SRT occurring at about 12 nm has been done so far.

In the present chapter, the structural and magnetic properties of Cu(5 nm) / Fe(t_{Fe}) / Cu(5 nm) / Ni(10 nm) / Cu(100 nm) / Si(001) multilayers with t_{Fe} = 1, 2 and 4 nm are presented. The growth was controlled *in situ* using reflexion high energy electron diffraction (RHEED) and the structural properties *ex situ* by x-ray reflectivity (XRR), x-ray diffraction (XRD) and high resolution transmission electron microscopy (HRTEM). On the other hand, the magnetic properties were measured by vibrating sample magnetometry (VSM), superconducting quantum interference device magnetometry (SQUID) and magnetic force microscopy (MFM).

Growth and in-situ characterization

Cu(5 nm)/t_{Fe}/Cu(5 nm)/Ni(10 nm)/Cu(100 nm) multilayers were grown by electron-beam evaporation and using a high temperature Knudsen cell on Si(100) substrates at room temperature in ultra high vacuum following a similar procedure as the described in chapter 1. The Fe layer thickness, t_{Fe}, ranged from 1 to 4 nm. The rates of evaporation were controlled by using a quartz crystal monitor and a flux monitor, for the electron beam evaporator and the effusion cell, respectively. Thus, the rates were 0.02 nm/s for nickel and copper, and 0.008 nm/s for the iron layer (e-cell). The pressure during deposition was not higher than 1×10^{-8} Torr. At the same time as the growth the samples were rotating 360^o at a constant velocity for, on one hand, to get a high homogeneity over the whole surface, and on the other hand, in order to study the full azimuthal dependence of the RHEED patterns.

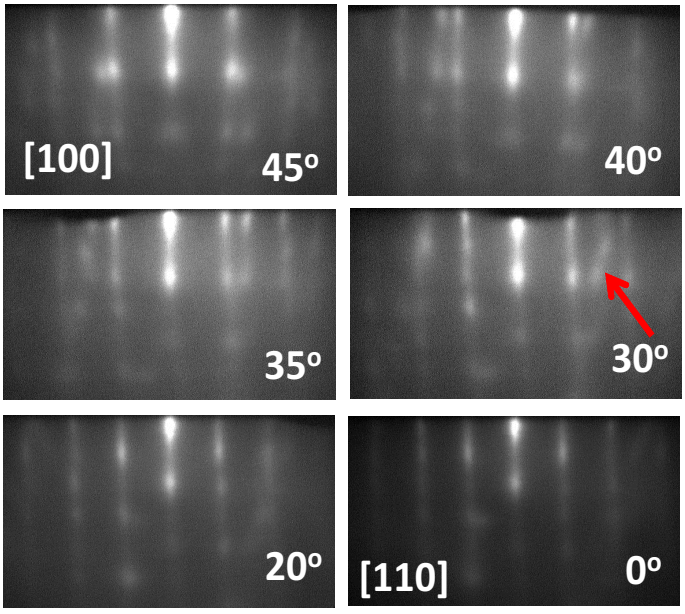

Figure 50: RHEED patterns taken for an iron layer with t_{Fe} = 2 nm along the angles and in between 45 to 0 degrees that correspond with the Cu [100] and Cu [110] azimuth directions, respectively.

Figure 49 shows the RHEED patterns taken at the [100] and [110] azimuth

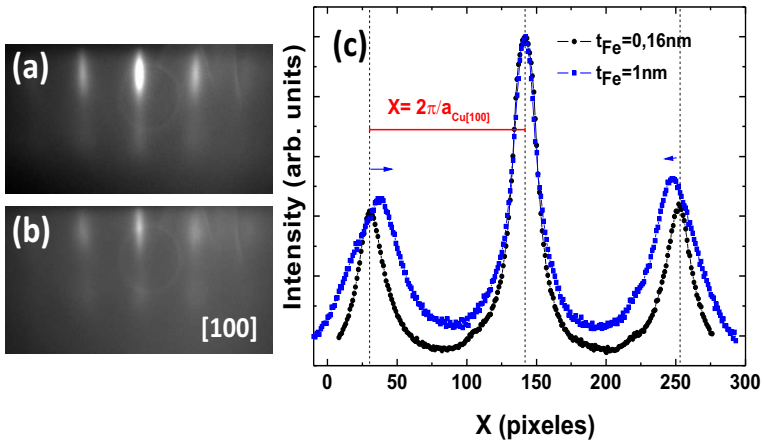

Figure 51: RHEED patterns taken for (a) $t_{Fe} = 0.16$ nm and (b) t_{Fe}= 1 nm. Profiles on (a) and (b) are shown in (c). The distance between two peaks is $2\pi/a_{Cu[100]}$

.

directions for copper buffer layer, the Ni film and the 5 nm thick Cu layer prior to the growth of the iron layer.

Figure 50 shows RHEED images taken along the [100] and [110] copper azimuth directions and, in between, at different angles for an iron film of 2 nm of thickness. Note that we have chosen the Cu[110] azimuth direction at 0 degrees. In comparison with the images in Fig. 49, the growth of an iron layer on top of the Cu/Ni/Cu system lead to unusual RHEED patterns. The relevant features in Fig. 50 are revealed from 30 to 45 degrees, where additional streaks appear indicating a different matching between the Fe and Cu/Ni/Cu crystal lattices. Notice that the streak at 30 degrees (marked with an arrow) is changing its position turning to the left on the pattern as the angle is increasing from 0 to 45 degrees. At 45 degrees the pattern displays a splitting of the main streaks suggesting that the misfit of the Fe lattice is present principally in the Cu [100] azimuth direction.

In order to study in detail the Fe growth processes dependent on the thickness, in steps of 0.16 nm during the preparation of a film with $t_{Fe} = 4$ nm, the evaporation was stopped and the whole angular variation of the RHEED pattern was recorded. Thus, the initial growth corresponds with a well ordered fcc surface with RHEED patterns that remain with the same structure and symmetries that the underlying Cu and Ni layers [see Fig. 51 (a)] being the ratio between the distances determined from the images that scan the [100] and [110] directions ≈ 1.41, a value that indicates the observation of a square Bravais lattice. Then, at about $t_{Fe} = 1$ nm, broad and diffuse streaks show up along the Cu[100] direction as it is shown in Fig. 51 (b). Here, we observe a variation of the in-plane lattice parameter on the [100] direction in

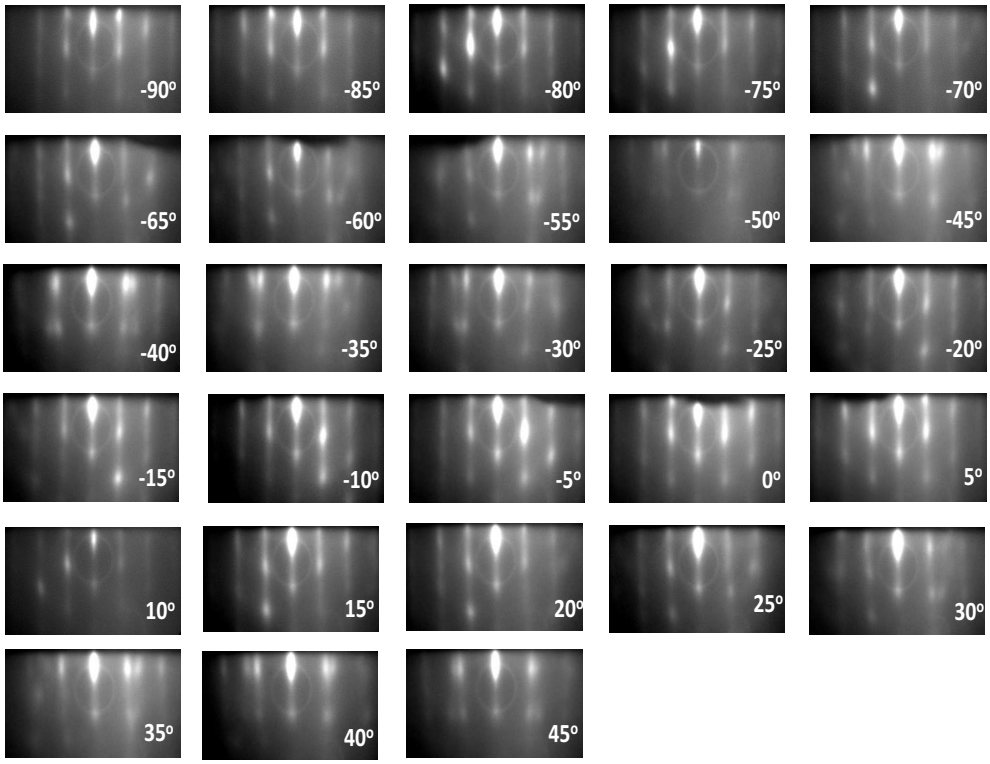

Figure 52: RHEED patterns dependent on the surface angle for a structure with $t_{Fe} = 2$ nm. 0 degrees corresponds with the Cu [110] azimuth direction.

which a_{Fe} is bigger than at the first steps of the growth (less than 0.8 nm), this can be seen by comparing the profiles taken on the last patterns as in Fig. 51 (c). Subsequently, the system keeps the same structure up to $t_{Fe} =$ 1.44 nm. For larger values of t_{Fe} the images become more complex suggesting the onset of the fcc to bcc phase transformation. As described, in Fig. 52 the RHEED images for $t_{Fe}=$ 2 nm in a complete angular dependence are shown. A fourfold symmetry of the crystal surface is observed with patterns that are reproducible each 90 degrees. By comparing these images with those showed in Fig. 50 for a film with an equivalent thickness but different time of growth, the presence of wide spots in the first one are indicating a surface rougher than that grown continuously, probably as a consequence of the stopping of the evaporation beam. In theory, the RHEED patterns consist of points resulting from the intersection of the Ewald sphere with the rods of the 2D reciprocal lattice. Due to the imperfection of the RHEED apparatus-angular and energy spread of the primary electron beam, and of the terraces of finite length, the RHEED patterns exhibit straight lines. Consequently, the better the qualities of the apparatus and the surface are, the shorter the length of the straight line on the RHEED patterns. Therefore, by comparing the images presented

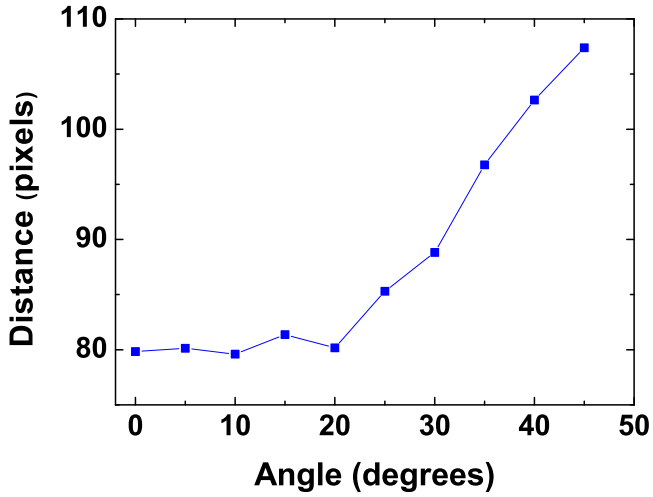

Figure 53: Variation of the in-plane lattice parameter with the angle on the surface for the RHEED patterns shown in Fig. 52.

in Figs. 49 and 50, longer streaks are observed in the last one revealing that the Fe capping layer is growing with a surface formed by structural domains or superstructures. Notice that all the RHEED images shown in this chapter have the same dimensions.

The distances between the streaks in the RHEED patterns (see Fig. 52) were measured in order to have an idea about the variation of the lattice parameter with the angle. Thus, as it is shown in the plot in Fig. 53, there is not variation of the in-plane lattice constant from 0 to 20 degrees, while at bigger angles it increases almost linearly. By taking as a reference the distance between the streaks in the Cu buffer layer (in Fig. 49) and assuming the value of the bulk Cu lattice parameter, we have calculated that the in-plane lattice constants of the Fe layer are: $a_{Fe[110]} = 4.99$ and $a_{Fe[100]} = 3.73$. These values demonstrate an in the plane expansion of the Fe fcc lattice ($a_{Fe,fcc} = 3.58$).

Finally, at $t_{Fe} = 4$ nm, the structure observed is basically the same although the images show off a tridimensional growth that is revealed for the presence of a spotty diffraction pattern (see Fig. 54). In addition, the splitting of the streaks on the Cu[100] azimuth direction displayed before is getting more and more defined with a variation of the angles in between as it is shown in Fig. 54 (b). Thus, we found that the tilt angle of the bifurcations with respect to the vertical are ≈ 6 degrees in both cases, at $t_{Fe} = 2$ and 4 nm. These results are consistent with the expected epitaxial relationships for similar systems [2]. The RHEED observations can be explained by taking into account the invariant line condition for a bcc(110) film grown on a fcc(100) substrate and state the optimum matching between two crystal planes at an interface is achieved when there is at least one direction along which the two

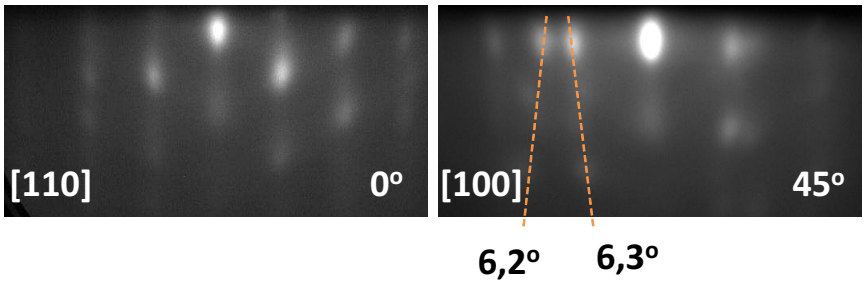

Figure 54: RHEED patterns of an iron film with 4 nm of thickness. The images were taken along the (a) Cu[110] and (b) Cu[100] azimuth.

crystals match perfectly on the interface [10]. Therefore, not variation is noted along the Cu[110] azimuth direction and thus, we can conclude this is the invariant-line direction.

After the Fe growth the sample was covered with 5 nm of Cu in order to protect it from the oxidation. The RHEED patterns at this step correspond with remanent rough surface that mainly follows the Fe surface lattice.

EX-SITU CHARACTERIZATION

Structural properties

X-ray reflectivity (XRR) and X-ray diffraction experiments were carried out by using a HRXRD Bruker D8 Advance with the K_α radiation of the Cu (λ = 1.54056 Å). The XRR patterns were simulated with LEPTOS program so that the thicknesses and the roughness of the films were obtained.

X-ray reflectivity measurements were done immediately after removing the samples from high vacuum, in order to determine the Fe layer thicknesses as it is shown in Fig. 55. For comparison, the reflectivity pattern for a Cu(5 nm) / Ni(10 nm) / Cu(100 nm) multilayer and the fit performed are presented in Fig. 55(a). In this case, the amplitude of the oscillations is reduced at 2 degrees, indicating an increase of the roughness at the interfaces. The thicknesses for the simulation are well correlated with the thicknesses expected. In Fig. 55 (b) a small variation in the periodicity of the oscillations is observed between $\approx$ 1.6 and 2.4 degrees due to the presence of a thinner iron layer. In Figs. 55 (c) and (d) two oscillation frequencies are revealed as a result of the increasing

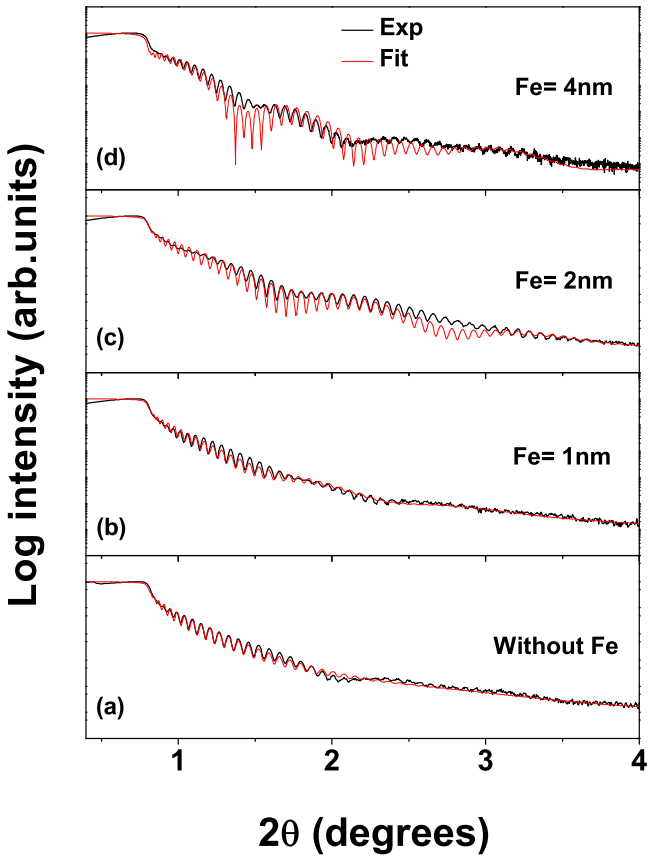

Figure 55: Experimental and simulated x-ray reflectivity spectra of Cu/t_{Fe}/Cu/Ni/Cu multilayers with t_{Fe} ranging from 0 to 4 nm.

Fe thickness, giving rise to a *bilayer* behavior, i.e., the Fe and Ni/Cu layers. These oscillation frequencies are not observed in Ni/Cu layer due to the small difference of their electronic densities. At $t_{Fe} = 2$ nm, the oscillations are extended up to ≈ 3.5, degrees showing that the roughness at the surface is reduced. This result confirms the RHEED diffraction patterns, where long structural coherence on the surface is shown. Also, there is a good adjustment of the oscillations between the experiment and the fit. Nevertheless, at 2.5 degrees the curve was not well followed by the simulation probably due to the presence of additional structural domains on the surface that were not introduce in the fitting program. When the thickness is increased at $t_{Fe} = 4$ nm, the bilayer oscillations are better defined and the roughness is higher than at $t_{Fe} = 2$ nm, here the presence of additional crystal structures is clear. In general, the reflectivity observations are in agreement with the results reported from RHEED.

Symmetrical θ - 2θ x-ray scans as a function of the Fe thicknesses are shown

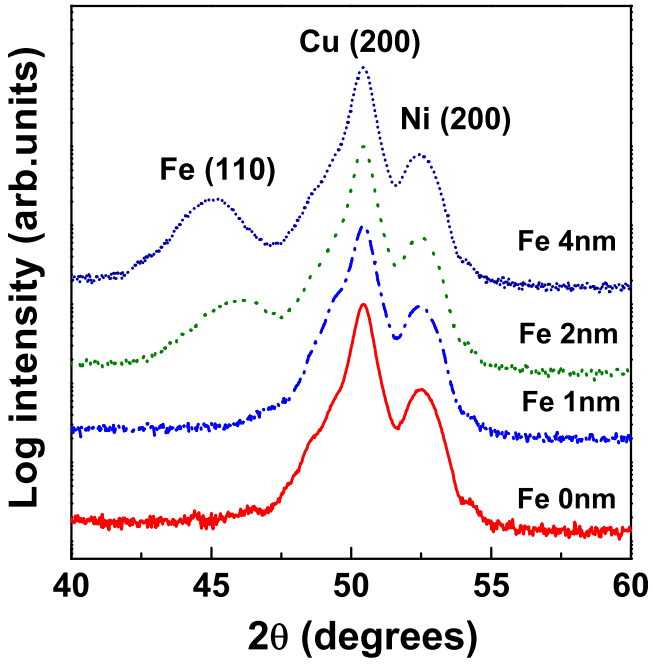

Figure 56: X-ray diffraction scans as a function of the Fe layer thickness for a Cu/Fe/Cu/Ni/Cu structure. For comparison the diffraction pattern for a sample without Fe is presented.

in Fig. 56. The presence of the 200 reflection from the Ni film near the [200] Bragg peak from the Cu buffer layer confirms its epitaxial growth. Thus, the out-of-the plane lattice parameter is $a_{Ni} = 3.48$ Åand corresponds with a strain $\epsilon_{\perp}$= -1.136%. The Fe peak is observed at t_{Fe}= 2 and 4 nm. Notice that the 2θ position of the peak is changing with the thickness, thus as t_{Fe} increases the lattice parameter is going towards the bulk Fe bcc (110) value ($a_{Fe-bcc[110]} =$ 4.058). From the XRD patterns, at $t_{Fe} = 2$ nm, $a_{Fe,\perp} = 3.9446$ giving a strain value of $\epsilon_{\perp} = -2.81\%$, and at $t_{Fe} = 4$ nm, $a_{Fe,\perp} = 4.018$ giving a strain value of $\epsilon_{\perp} = -0.98\%$, with respect $a_{Fe-bulk}$. These results show that at $t_{Fe} = 2$ nm the lattice is expanded in-plane to adapt itself to the Cu/Ni/Cu structure and as a result the perpendicular parameter is compressed, reveling that the Fe lattice is an intermediate region between a fcc and a bcc structure. While at t_{Fe}= 4 nm the crystal structure is governed by the bcc(110) lattice, at $t_{Fe} = 1$ nm, we note the lack of an iron peak indicating that for this thicknesses the fcc(100) lattice grows epitaxially on the Cu/Ni/Cu structure and its contribution to the diffraction pattern can be overlapped by the Cu(200) peak.

In order to complement the diffraction techniques that average the volume of the sample, a nanostructural characterization of a Cu(100 nm) / Ni(10 nm)/ Cu(5 nm) / Fe(2 nm) / Cu(5 nm) structure has been carried out by means

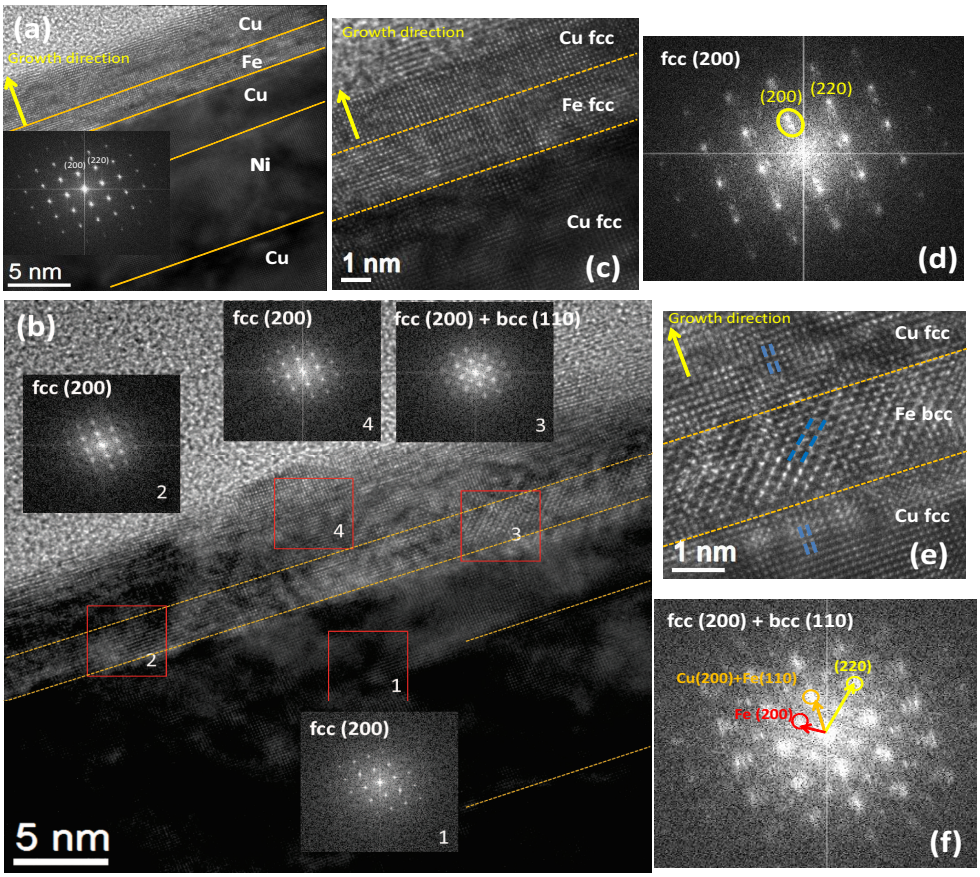

Figure 57: HRTEM images of a Cu(100 nm)/Ni(10 nm)/Cu(5 nm)/Fe(2 nm)/Cu(5 nm) multilayer. (a) Low magnification cross-sectional image of the full system and its corresponding FFT pattern. (b) FFT patterns for different regions on the multilayer as can be identify by the numbers. (c) High resolution image for a Fe(200)‖Cu(200) area. (e) High resolution image for a Fe(110)‖Cu(200) area. (d) and (f) FFT patterns for the regions shown in (c) and (d), respectively.

of High Resolution Transmission Electron Microscopy (HRTEM) using a FEI-Titan Cube microscope equipped with a CETCOR Cs- objective corrector and operated at 300 kV (point to point resolution of 0.08 nm). The Fast Fourier Transform (FFT) images were obtained by means Digital Micrograph software. Figure 57 (a) shows a low magnification cross- sectional image of the Cu/Fe/Cu/Ni/Cu region of the structure. The inset shows the FFT of the full image with diffraction spots that correspond with the {200} and {110} family of planes of the epitaxial fcc Cu/Ni/Cu structure. The incident electron beam is along the Cu[200] direction. FFT images were made on different regions on the multilayer as it is presented in Fig. 57 (b). Note that the numbers are indicating a zone and its corresponding FFT pattern. The diffraction images

on the copper and nickel layers reveal a square (200) zone axis. Along the Fe layer the presence of areas with different features is observed. In Figs. 57 (c) and (d) high-magnification cross-sectional images on these areas are shown with the respective FFT patterns in Figs. 57(e) and (f). In Fig. 57 (c) the Fe atomic planes follow the Cu ones and the interface between the Fe and Cu cover layer is not seen, meaning a high quality matching of the interfaces. In Fig. 57 (e) the Fe atomic planes are rotated 45 degrees with respect to the Cu seed layer, and then, the Cu planes recover the original orientation. In addition, well defined interfaces are observed. A diffraction pattern corresponding with a fcc (200) structure is observed in Fig. 57 (d), where elongated and double spots indicate that the Fe lattice is expanded along the growth direction. On the other hand, the analysis of the FFT pattern in Fig. 57 (f) confirms the coexistence of fcc with bcc crystallites of the family of planes {200} and {110}, respectively.

The observation of this structure supports the presence of fcc and bcc crystallites for iron showing that both structures happen simultaneously on a Cu/Ni/Cu structure. Therefore, the high-magnification images resolve that the Fe grows as bcc(110)‖Cu(200) and fcc(200)‖Cu(200) grains. The bcc grains nucleate through the complete iron thickness up to the copper substrate layer, although for thinner films the iron grows forming a single fcc phase. The result is a growth mode in which a self-assembled double epitaxial structure is formed by the nucleation of bcc (110) grains in strained epitaxial (100) fcc blocks.

Magnetic Properties

Figure 58 displays the hysteresis loops with the magnetic field H applied parallel and perpendicular to the film plane for different Fe thicknesses. In Fig. 58(a) the magnetization curves for a sample with and without Fe (Ni film) are compared. The 10 nm thick nickel film exhibits out of plane magnetization, being the remanent magnetization $M_r \approx 0.9\ M_s$. The addition of iron reduces the remanence of the out of the plane loop so that for: t_{Fe}= 1 nm, $M_r \approx 0.80\ M_s$; t_{Fe}= 2 nm, $M_r \approx 0.22 M_s$; and finally, for $t_{Fe} = 4$ nm, $M_r \approx 0.3 M_s$, while the saturation magnetization is increasing in such a way that for $t_{Fe} = 1$ nm, M_s=0.14 memu; for $t_{Fe} = 2$ nm, $M_s = 0.22$ memu; and for $t_{Fe} = 4$ nm, $M_s = 0.33$ memu; this dependence with the Fe thickness is shown in Fig. 59. Note that the easy axis of magnetization changes to be in the film plane, this is in agreement with the strong effect of the dipolar anisotropy of the Fe layer.

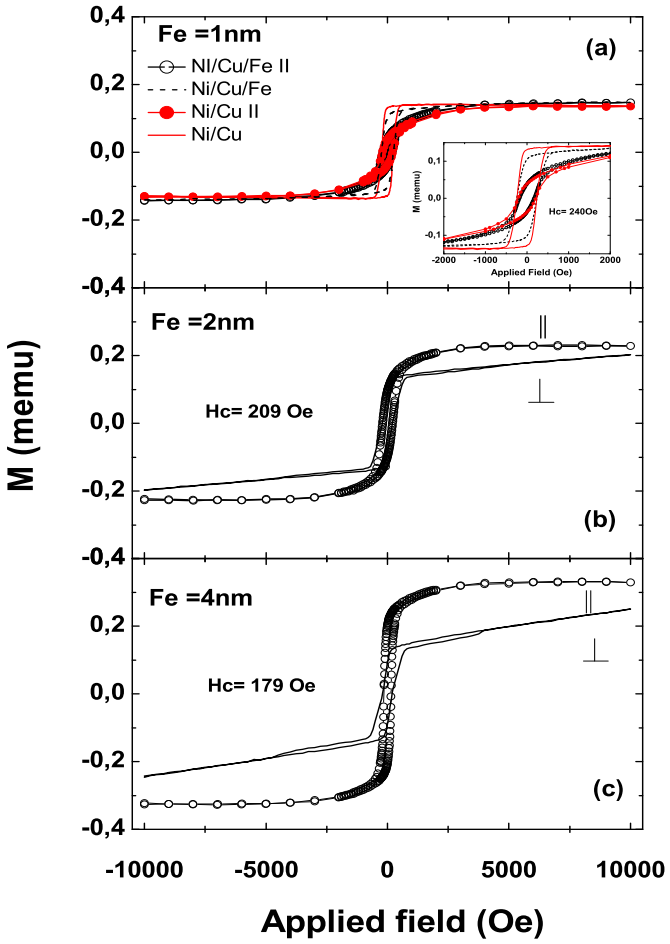

Figure 58: In-plane and perpendicular magnetization loops for Cu/t_{Fe}/Cu/Ni/Cu multilayers with t_{Fe} ranging from 0 to 4 nm. In (a) the curves for a sample with $t_{Fe} = 1$ nm are compared with those of a sample without Fe. (b) for $t_{Fe} = 2$ nm and (c) for $t_{Fe} = 4$ nm.

The presence of iron is noticed also because the B-H loops requires a field close to the anisotropy field (4πM) to reach saturation, as far as the perpendicular loop concerns. Thus, while for the structure with $t_{Fe} = 4$ nm, the saturation is almost completed for $H = 2 \times 10^4$ Gauss, a field value close to the anisotropy field deduced from a magnetostatic anisotropy ($4\pi M \approx 2.2 \times 10^4$ Gauss), for the structure with $t_{Fe} = 2$ nm, the saturation decreases significantly down to 1.2×10^4 Gauss, as it was found from the measurement of the hysteresis loops at 10 K (See Fig. 60). On the other hand, the coercive fields, Hc, of the in-plane and out-of-plane hysteresis loops are identical and their value reduce with the Fe layer thickness, so that: for $t_{Fe} = 0$ and 1 nm, Hc= 240 Oe, for $t_{Fe} = 2$ nm, Hc= 209 Oe and for $t_{Fe} = 4$ nm, Hc= 179 Oe. These

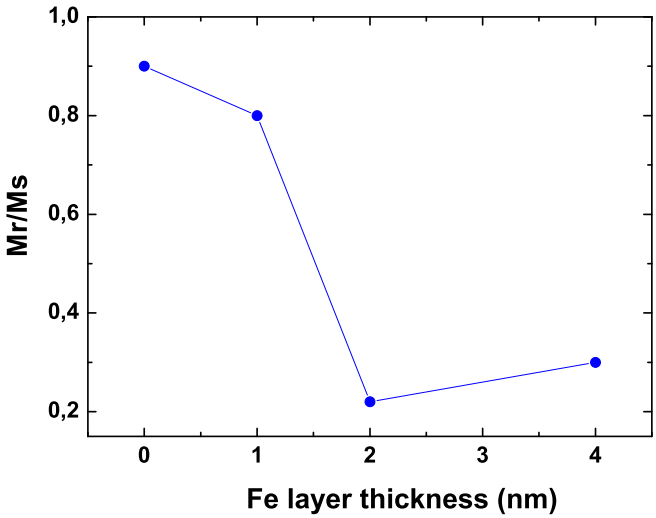

Figure 59: Dependence of the normalized magnetization for different Fe layer thicknesses.

t_{Fe} (nm)	M_r/M_s	M_s(memu)	**Hc** (Oe)	**d** (nm)
0	0.9	0.14	240	600
1	0.8	0.14	240	400
2	0.2	0.22	209	260
4	0.3	0.33	179	180

Table 3: Summary of magnetic parameters of Cu/Fe/Cu/Ni/Cu//Si(100) multilayers.

experimental values are shown in Table 3. Another observation is that in-plane magnetic measurements as a function of the angle show the lack of an in-plane anisotropy.

Figure 67 shows MFM images taken on the films without iron, Fig. 67 (a), and with t_{Fe} = 1 Fig. 67(b), 2 Fig. 67(c) and 4 nm Fig. 67(d). The domain pattern for the nickel film indicates that the magnetization is held to a perpendicular direction in agreement with the magnetometry measurements. The contrast appears due to magnetization pointing into and out of the plane. The domain size, d, of the nickel film is calculated by averaging several domains and it is found to be about 600 nm, a value similar to that found in a previous work [12].

The samples with t_{Fe} = 1, 2 and 4 nm also show a domain structure with perpendicular orientation in which there are some areas with intermediate contrast. These finding can be explained if there are small regions with effective

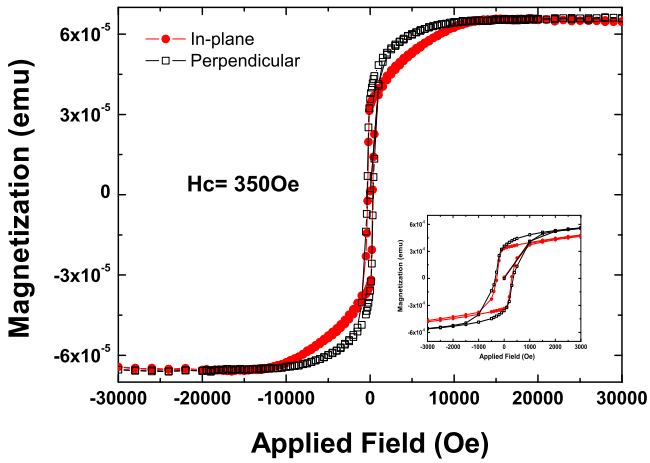

Figure 60: In-plane and Out-of-plane magnetization loops for a Cu (5 nm)/Fe (2 nm)/Cu (5 nm)/Ni (10 nm)/Cu (100 nm) structure. The measurements were performed at 10 K using a SQUID magnetometer.

in- plane magnetization, thus, the magnetic anisotropy in one of the films could favor the parallel magnetization. In addition, the MFM images reveal a decreasing of the average domain size as t_{Fe} increases, with d about 400 nm for the structure with t_{Fe}= 1 nm, 260 nm for t_{Fe} = 2 nm and 180 for t_{Fe}= 4 nm. Therefore, the domain pattern suggests first, that the iron film induces a decrement of the magnetostatic energy of the Fe/Cu/Ni structure and, as a result, more domain walls can be included in the nickel film and, secondly, that the iron layer adapts itself to the nickel magnetic orientation.

The magnetostatic coupling expression has been formulated for multilayers with perpendicular anisotropy and coupled stripe domain structures with domain walls alignment along the blocks [13, 14], and for films with antiferromagnetic coupling that can induce the coexistence of areas with parallel and antiparallel alignment of the magnetization [15]. In those works, the magnetic blocks have the same thickness and their separation is constant. In this work, the total magnetostatic energy density for multilayers with blocks of different materials and thicknesses is presented. So, the total magnetostatic energy density of the system, E_M, can be written as:

$$E_M = E_{M,0} + E_{M,i} + E_w \tag{18}$$

$E_{M,0}$ is the magnetostatic intralayer energy due to the energy per unit volume per film due to the self-interaction of each magnetic layer.

$$E_{M,0} = \frac{16 M_{Ni}^2 d}{\pi^2 t_{Ni}} \sum_{n=1,3,5,\ldots} \frac{1}{n^3} \left(1 - exp(-k_n t_{Ni})\right) \tag{19}$$

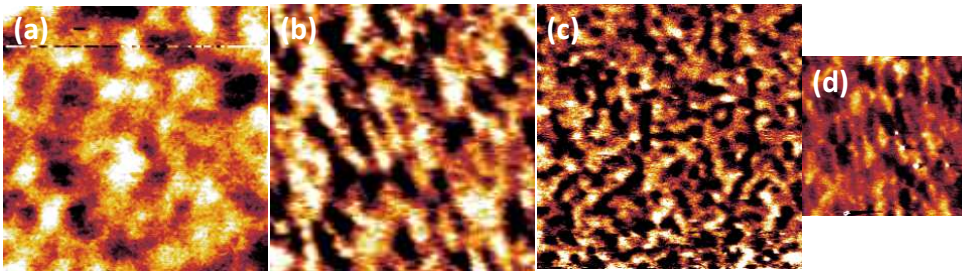

Figure 61: MFM images taken on Cu(5 nm)/t_{Fe}/Cu(5 nm)/Ni(10 nm)/Cu(100 nm) multilayers for: (a) t_{Fe}= 0, (b) t_{Fe}= 1 nm, (c) t_{Fe}= 2 nm and (d) t_{Fe}= 4 nm. In (a-c) the areas of the images are 5×5 μm^2 and, in (d), 3×3 μm^2.

$E_{M,i}$, is the magnetostatic interlayer which is due to the interaction between the layers.

$$E_{M,i} = -\frac{8M_{Ni}M_{Fe}d}{\pi^2 t_{Ni}} \sum_{n=1,3,5,\ldots} \frac{1}{n^3} exp(-k_n t_{Cu})[(1 - exp(-k_n t_{Ni})) \times (1 - exp(-k_n t_{Fe}))] \quad (20)$$

where E_w= $\frac{\sigma}{d}$ is the domain wall energy, d is the domain size, t_{Ni} and t_{Fe} are the thicknesses of the Ni and Fe films, respectively, M_{Ni} and M_{Fe} are the saturation magnetization for Ni and Fe, respectively, k_n= πn/d and σ is the domain wall energy per unit area.

This correction introduces a reduction of the magnetostatic energy in the film associated to the factor $k_n t_{Cu}$. For $k_n t_{Cu}$ small (d larger than t_{Cu}) the value of $exp(-k_n t_{Cu})$ is close to one, but if $k_n t_{Cu}$ is larger (d smaller than t_{Cu}), $exp(-k_n t_{Cu})$ tends to zero and the system behaves as a bunch of independent films. Thus, if the rest of physical parameters that control the domain wall remain constant, results in the reduction of the domain size [16, 17] by increasing the number of magnetic blocks, suggests the possibility of increasing the number of domain walls present in the film and therefore create media with higher density.

To quantify the effect of Fe layer on the total magnetostatic energy of the Cu/Fe/Cu/Ni/Cu system, we have plotted E_M as a function of the domain size as it is shown in Fig. 62. The mimima of the magnetostatic energy are more pronounced and appear at smaller d values as the Fe thickness increases, and as a result smaller magnetic domains are created. The domain sizes calculated are in excellent agreement with the values measured by MFM.

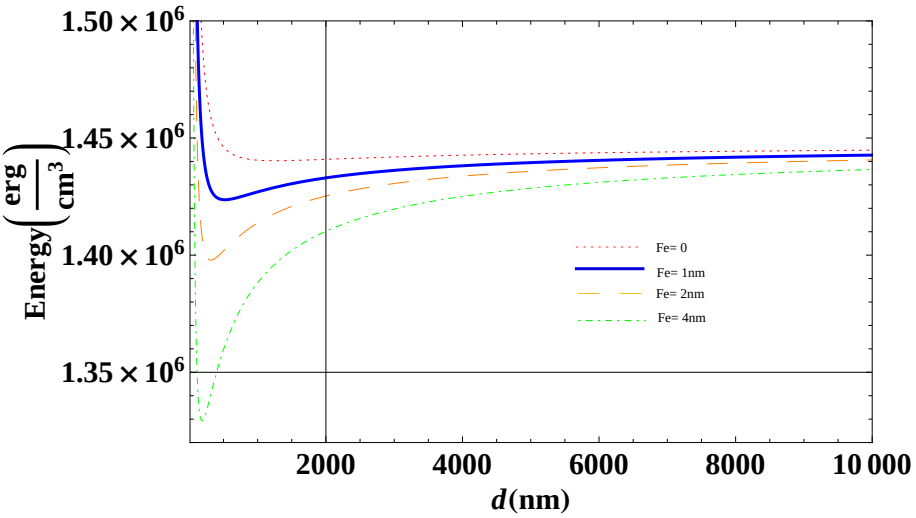

Figure 62: Plot of the total magnetostatic energy for different values of the Fe layer thicknesses as a function of the domain size.

DISCUSSION

The changes in the hysteresis loops for the Fe/Cu/Ni structure are somewhat unusual. The evident effects of the Fe layer on the hysteresis loops have shown that, in the whole range studied in this work, the Fe is ferromagnetic at room temperature, meaning that the Curie temperature of these Fe films is increased by the presence of the Ni layer. From a Fe thickness of 2 nm the easy axis of the magnetization now lies within the surface plane, although the out-the-plane hysteresis loop remains without strong changes revealing on this way that the magnetoelastic anisotropy that governs the Ni layer is still strong. Thus, the Fe layer probably affects the in-plane components of the domain walls in the Ni layer, pinning their movement in the perpendicular direction. On the other hand, the reduction of the coercive field means that the Fe capping layer reduces the amount of work required to flip the spins of the Ni layer. This could be due to differences in anisotropy energy in Fe and Ni layers.

CONCLUSIONS

RHEED, XRR, XRD and HRTEM experimental results have shown that the Fe growing on a Cu/Ni/Cu structure can be divided in three different cases. Firstly, down $t_{Fe} = 2$ nm where a Fe fcc(200) ∥ Cu/Ni/Cu fcc(200) epitaxial relationship was observed. Secondly, in between $t_{Fe} = 2$ and 3 nm where the coexistence between Fe fcc(200) and bcc(100) grains ∥Cu/Ni/Cu fcc(200) was demonstrated. Finally, for $t_{Fe} = 4$ nm or ticker, in which case the bcc structure is the dominant one according to the XRD patterns.

The effect of the Fe thicknesses on the perpendicular anisotropy of a Cu / Ni(10 nm) / Cu was studied. We found that the strong magnetostatic energy of the iron layer is unable to overlap the perpendicular anisotropy of the Ni layer due to the fact that the remanence magnetization does not change significantly. Nevertheless, as t_{Fe} increases the in-plane magnetization is favored. In the same way, perpendicular domains were shown with a reduction of the domain size that is explained because of the effect of the Fe layer on the total magnetostatic energy.

References IV

[1] W. L. O'Brien and B. P. Tonner, Phys. Rev. B **52**, 15332 (1996).

[2] R. Naik, C. Kota, J. S. Payson, and G. L. Dunifer, Phys. Rev. B **48**, 1008 (1993).

[3] P. Luches, G. C. Gazzadi, A. di Bona, L. Marassi, L. Pasquali, S. Valeri and S. Nannarone, Surf. Sci. 419, 207-215 (1999).

[4] G. C. Gazzadi, P. Luches, A. di Bona, L. Marassi, L. Pasquali, S. Valeri and S. Nannarone, Phys. Rev. B **61**, 2246 (2000).

[5] D. P. Pappas et al, Phys. Rev. B **45**, 8169 (1992).

[6] R. Ramchal, A. K. Schmid, M. Farle, and H. Poppa, Phys. Rev. B **69**, 214401-1 (2004).

[7] X. Liu, B. Schirmer, and M. Wuttig, Phys. Rev. B **65**, 224413 (2002).

[8] Y. Z. Wu, C. Won, A. Scholl, A. Doran, H. W. Zhao, X. F. Jin, and Z. Q. Qiu, Phys. Rev. Lett.**93**, 117205-1 (2004).

[9] J. Choi, J. Wu, C. Won, Y. Z. Wu, A. Scholl, A. Doran,T. Owens, and Z. Q. Qiu, Phys. Rev. Lett.**98**, 207205 (2007).

[10] M. Kato, S. Fukase, A. Sato, and T. Mori, Acta metall. Vol.34, No.7, 1179-1188 (1986).

[11] M. Kato, M. Wada, A. Sato, and T. Mori, Acta metall. Vol.37, No.3, 749-756 (1989).

[12] G. Bochi, H. J. Hug, D. I. Paul, B. Stiefel, a. Moser, I. Parashikov, H.-J. Güntherodt, and R. C. O'Handley, Phys. Rev. Lett. 75, 1839 (1995).

[13] A. Suna, J. Appl. Phys. **59**, 313 (1986).

[14] H. J. G. Draaisma and W. J. M. de Jonge, J. Appl. Phys. **62**, 3318 (1987).

[15] K. Janicka, J. D. Burton and E. Y. Tsymbal, J. Appl. Phys. **101**, 113921 (2007).

[16] N. S. Kiselev, I. E. Dragunov, V. Neu, U. K. Rler, and A. N. Bogdanov J. Appl. Phys. 103, 043907 (2008).

[17] M. Tekielak, R. Gieniusz, M. Kisielewski, P. Mazalski, A. Maziewski, V. Zablotskii, F. Stobiecki, B. Szymanski and R. Schafe J. Appl. Phys. 110, 043924 (2011).

Chapter V

Transverse Magnetization in Ni rings

Introduction

The strain state in a nanostructured material has become a fine tuning parameter to control physical properties as the exciton spectra in semiconductor ZnO microwires [1], the polarization in ferroelectric materials [2], the critical temperature in superconductors [3] or the order temperature in magnetic films [4]. Another fundamental property controlled by the strain state is the magnetic anisotropy through the inverse magnetoelastic (ME) effect: the strain state in the film is coupled to the magnetic lattice and the ME stress coefficients reflect the strength of the spin-orbit coupling. Strain dependence of the magnetic anisotropy energy has been observed in nickel films grown on copper [5–9], and other 3d metal films (Co/Au [10]), and alloys (like $Ni_{90}Fe_{10}$ [11]) as well as rare earth superlattices [12].

For materials with low magnetization values, which give rise to films with low magnetostatic energy, and cubic crystal structure that results in a feeble magnetocrystalline anisotropy, the contribution of the ME density energy e_{ME} can be particularly important if the residual strain components are 1% and the ME coupling coefficient is, at least, in the range of MPa. This scenario is found for Ni grown epitaxially on the (001) direction on top of Cu with a tetragonal distortion of the cubic lattice: the in-plane strain is isotropic (ε_{xx}=ε_{yy}= $\varepsilon_{\parallel}$) and the out of the plain strain proportional to the in-plane values: (ε_{zz}=$\varepsilon_{\perp} = -(2c_{12}/c_{11})\varepsilon_{\parallel}$), and all of them are around 1% for Ni films as thick as 10 nm [13]. The total anisotropy energy includes the ME term $e_{ME} = -B_1(\epsilon_{\parallel} - \epsilon_{\perp})cos^2\theta$ with B_1 being a bulk ME coefficient and M_s the saturation magnetization, with θ the angle between the film normal ([001] (crystallographic direction) and the magnetization vector.

A further step is the control of the magnetic anisotropy and domain configurations in magnetic elements with submicron lateral dimensions, as that is the scale for actual spintronic devices. Planar nanowires and nanorings have been investigated because of their potential use in domain-wall devices proposed for data storage [14] and logic applications [15]. Most reported work has been focused on elements with polycrystalline crystal structure, whose properties are dominated by shape anisotropy. The stable domain configurations are 180^o transverse or vortex-like domain walls (DW) depending on the element dimension [16]. The ring geometry presents two different stable states, usually called

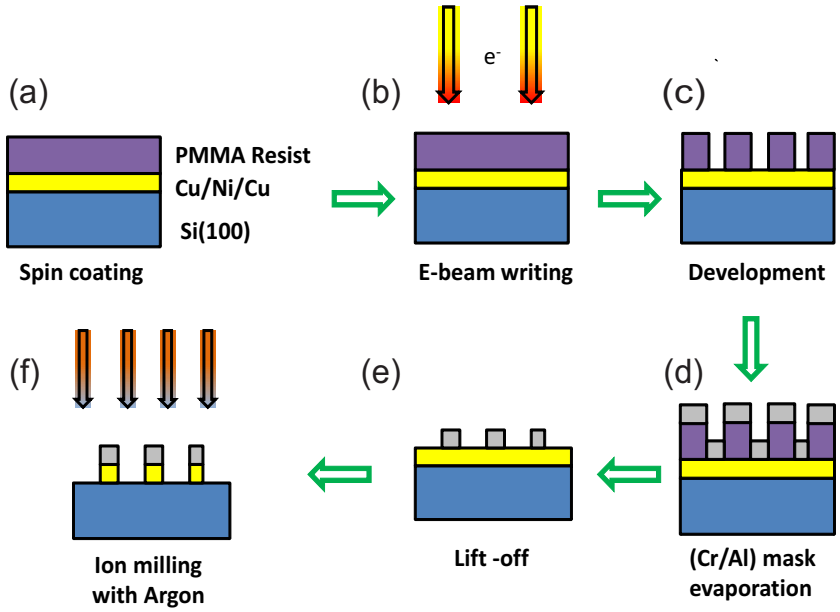

Figure 63: Schematic representation of the patterning of Cu/Ni/Cu/Si films by a subtractive process using electron beam lithography and lift-off techniques.

vortex and onion states, which can be easily reached by applying a magnetic field in the film plane [17]. However, materials with different domain states and DW geometries could offer advantages in spintronic applications, as is the case of metallic planar NWs with perpendicular magnetic anisotropy which exhibit enhanced spin-torque efficiency and higher thermal stability compared to those of NWs with in-plane anisotropy [18, 19]. Therefore, developing methods for tuning the magnetic anisotropy in nanomagnets may offer new opportunities for spintronic devices.

In this chapter we report the fabrication and observation of magnetic domain configurations that defy the magnetostatic anisotropy in magnetic nanorings made in epitaxial Cu/Ni/Cu films with a nickel film thickness in the range where the effective perpendicular anisotropy coefficient is ≈ 0 and magnetic configurations associated with in-plane magnetic anisotropies are expected. These rings were fabricated by subtractive processing of epitaxial Cu/Ni/Cu film using via electron beam lithography combined with ion beam etching using a metallic hard mask.

Electron beam lithography

Because the the elimination of the native oxide would damage a mask prepared directly on the substrate, patterned ring structures have to be fabricated by a subtractive process. The procedure used in this thesis includes electron beam (e-beam) lithography, e-beam evaporation of a hard mask, lift-off techniques and ion beam etching. A schematic representation of the patterned process is shown in Fig. 63. The Cu/Ni/Cu thin films were coated with a double layer, 120 and 270 nm, of polymethylmethacrylate (PMMA) resin with molecular weights, 50 kg/mol and 950 kg/mol respectively, baked separately for 10 minutes at 120^{o}C. Exposures were performed at 10 kV accelerating voltage using a beam current of $\approx$ 80 pA such that the delivered dose was 99 $\mu C/cm^2$. The exposed sample was developed with AR 600-56 developer for 30 s with a soft agitation followed by a quench in isopropyl alcohol for 30 seconds, both steps at room temperature. Figure 64(a) shows a SEM picture of a ring at this point in the process.

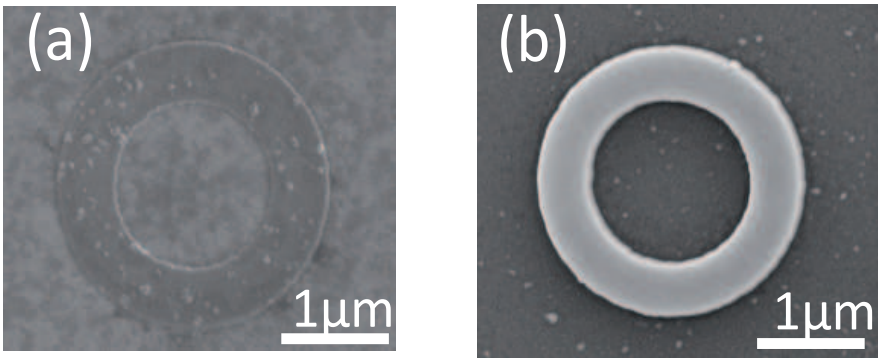

Figure 64: Scanning electron microscopy taken on a ring after (a)the lift-of and (b) ion beam etching steps.

After the development, in order to improve the sharpness of the rings and to protect the Ni layer during the ion beam etching step, a Cr(5nm)/Al(14nm) hard mask was evaporated. The bottom Cr block favors adhesion for the high sputtering yield layer of Al. Ion beam etching using Ar ions removes the Ni layer outside the hard mask. The Ar pressure was 4×10^{-4} mbar and the

milling rate about 10 nm/min. Processing the sample for 2 minutes produces structures like the ring shown in Fig. 64(b).

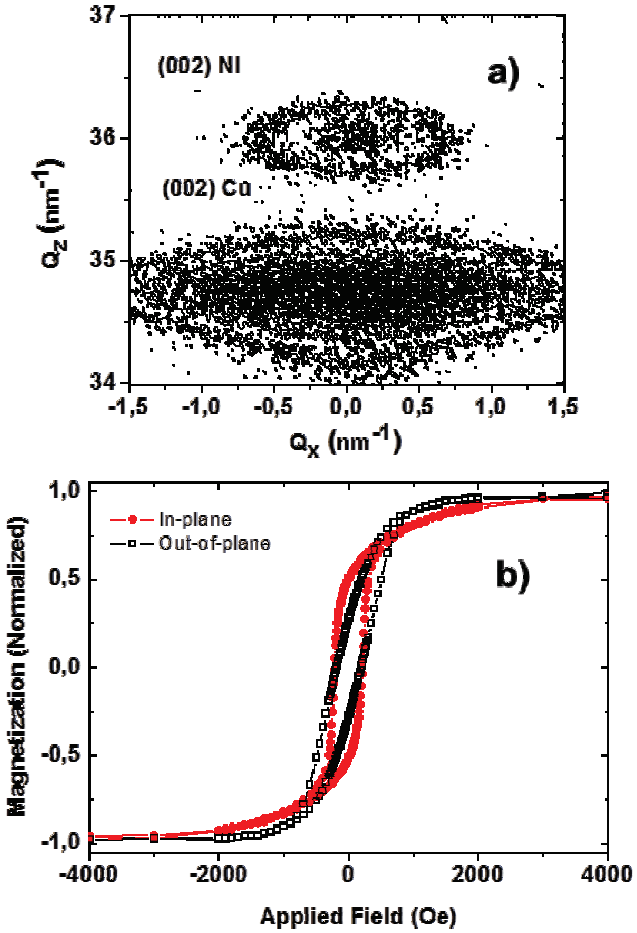

Figure 65: (a) Reciprocal space map in the vicinity of the symmetrical nickel and copper (002) reflection. (b) Hysteresis loops with H perpendicular to the the plane and in-plane for the Cu/Ni/Cu film.

The selected nickel film thickness is in the range where the net magnetic anisotropy undergoes reorientation and the easy direction for the magnetization is moving from out of the plane to the in-plane directions as t_{Ni} increases. In this range of thicknesses the ME stress contribution is compensated by the magnetostatic term. For the Ni film studied here the $\varepsilon_\perp$ is about 0.96% as can be calculated from the reciprocal space map taken around the (200) reflection, see Fig. 65(a). Therefore $B_1(\epsilon_\parallel - \epsilon_\perp) \approx 0.12$ MJ/m^3 while $(1/2)\mu_0 M^2 \approx 0.14$ MJ/m^3. This fact is also observed in the minor differences between the in-plane and out of the plane M-H loops measured by Vibrating Sample Mag-

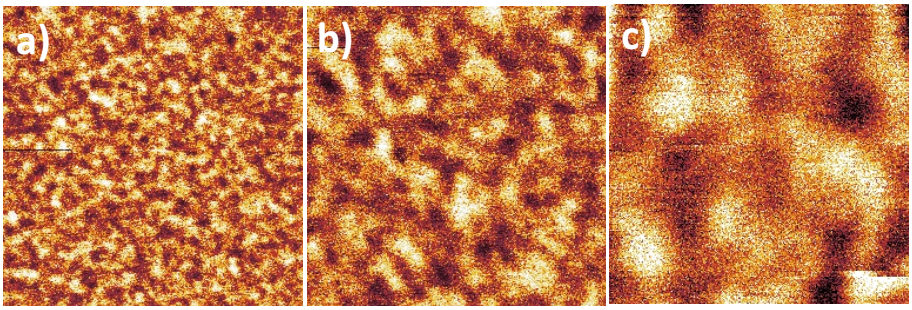

Figure 66: Magnetic force microscopy images of the unpatterned film. Size window is (a) 10 μm x 10 μm, (b) 5 μm x 5 μm and (c) 1.3 μm x 1.3 μm

netometry (VSM) see Fig. 65(b). The domain structure (see Fig. 66), measured by means of Magnetic Force Microscopy (MFM), shows domains with typical lateral dimension of $\approx$ 200 nm in accordance with previous works [20].

Magnetic Force Microscopy

The magnetic domain structure was measured by mean of Magnetic Force Microscopy using the tapping technique. Low moment magnetic tips were used to obtain the images shown in this chapter either at zero field after applying magnetic field in the film plane or with H applied in the plane diameter of 3 μm and line width of 250 nm.

Remanent state

Figure 67 taken at zero field after applying magnetic field in the film plane on a ring with an outer diameter of 3 μm and line width of 250 nm. This image condenses similar images observed for rings with the same diameter and line widths from 100 nm to 400 nm fabricated on films with thickness between 10 and 15 nm. Two main features are observed: first, that the magnetic contrast extends over distances exceeding the ring dimensions and, secondly, that along the radial direction it oscillates between two extreme values at positions around the edges of the ring and passes through zero at approximately the ring mean radius. This stay field is compatible with a transverse structure with the magnetization pointing along radial direction. A simple model supports the qualitative analysis of the MFM images: Fig 68 shows the calculation of the strength of the z component of the fringing field perpendicular to the plane

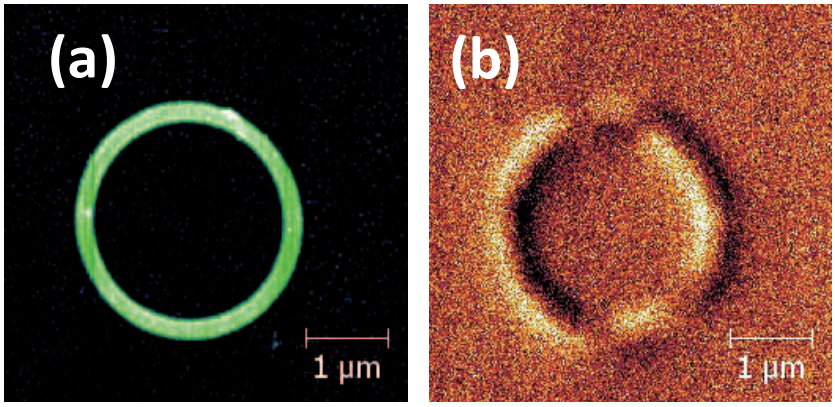

Figure 67: (a)Atomic force microscopy and (b) magnetic force microscopy images taken on a 3 μm diameter ring and line width of 250 nm.

H_z as function of y, the distance from the center of a infinite planar nanowire with uniform magnetization transverse to the wire axis [21] compared with H_z for the same wire with two domains with perpendicular, uniform $\mathbf{M}$ and negligible domain wall thickness. For both cases the stray field is zero at the center of the nanowire although the extreme values are located closer to the edges for the wire with $\mathbf{M}$ in the plane than for the wire with perpendicular domains. For the latter case, it is also noted that $H_z \approx 0$ away of the wire area while H_z decreases more slowly if $\mathbf{M}$ is in the plane as is observed in the MFM image.

Diameter and line width dependencies of the MFM images

Figure 69 shows AFM and MFM images for rings with $D = 3$ μm and W ranging from 1.3 μm to 250 nm. The images were taken after applying magnetic field perpendicularly to the sample. Rings with $W = 1.3$ μm and 1.2 μm [Fig. 69(a) and (b)] show, in the body of the ring a domain structure similar to that observed on the unpatterned film. A thin region at the outer edge of the ring show a domain structure that alternates dark and bright contrast. The last feature is enhanced as the W decreases and also appears at the inner edge ring for W = 1 μm, 800 nm and 550 nm [Figs. 69(c),(d) and (e)]. For $W =$ 430 nm, see Fig. 69(f), the contrast of the inner edge is correlated with the contrast at the external edge in such a way that bright and dark areas appear at opposite sides of the ring. For W = 280 nm and 250 nm [Figs. 69(g) and (h)] the different domain structure in the body of the ring disappear and the signal oscillates between bright and dark contrast along the radial direction. These features indicates that the ring magnetic configuration minimizes the magnetostatic energy by coupling the edge magnetization and alternating the sing of M at the edges as happens in domain stripes in thin films.

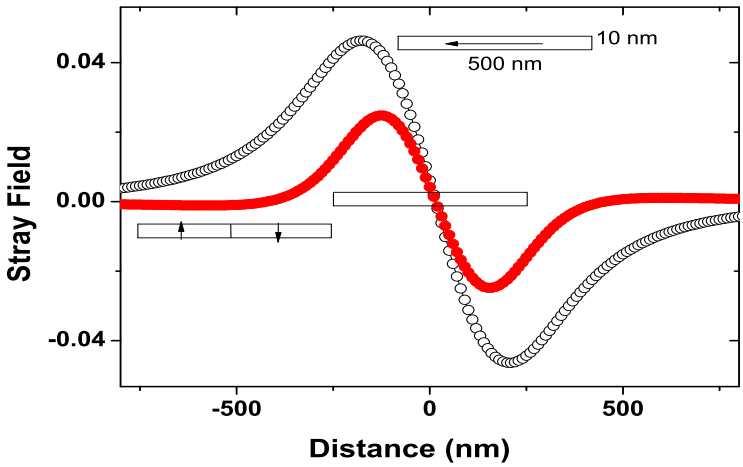

Figure 68: Vertical component H_z of the stray field at z = 225 nm as a function of the distance y transverse to the axis of an infinite rectangular wire with (a) uniform magnetization confined in the plane perpendicular to the wire axis and with two domains with M perpendicular to the plane. The wire is 500 nm wide and 10 nm thick.

A more detailed evolution of the domain structure in the ring width range where the inner domain structure disappear W < 400 nm is presented in Fig. 70 for rings with D = 2 μm. For the wider ring studied W = 460 nm, Fig. 70(a), changes in the extreme values of the contrast at the outer radius with a weaker magnetic contrast inside the ring is still observed. Decreasing W, in a series of rings with W decreasing in steps of $\approx$ 50 nm, it can be observed as the contrast due to opposite magnetic poles along both the outer and inner radius increases, becoming also opposite poles correlated between the edges and without magnetic structure between of the poles.

Magnetic Field Evolution

The dependence of the domain structure with the applied field is show in Fig. 71 for a ring with W = 200 nm, a value with contrast due to magnetic poles at the edges. The field was applied along the Ni[100] direction, the ring was saturated at negative field of -800 Oe and then H was changing up to positive values of H. At large field (see the image taken 400 Oe) a contrast changing from dark to bright along the field direction is observed. As H decreases and change its sign the continuous domain structure breaks and the radial unidirectional contrast oscillate with ϕ, see Fig. 71, for H between 110 Oe and 210 Oe. The images taken for H = 160 Oe and 195 Oe, show that the domain area with the opposite radial polarities are balanced out suggesting that around the coercive

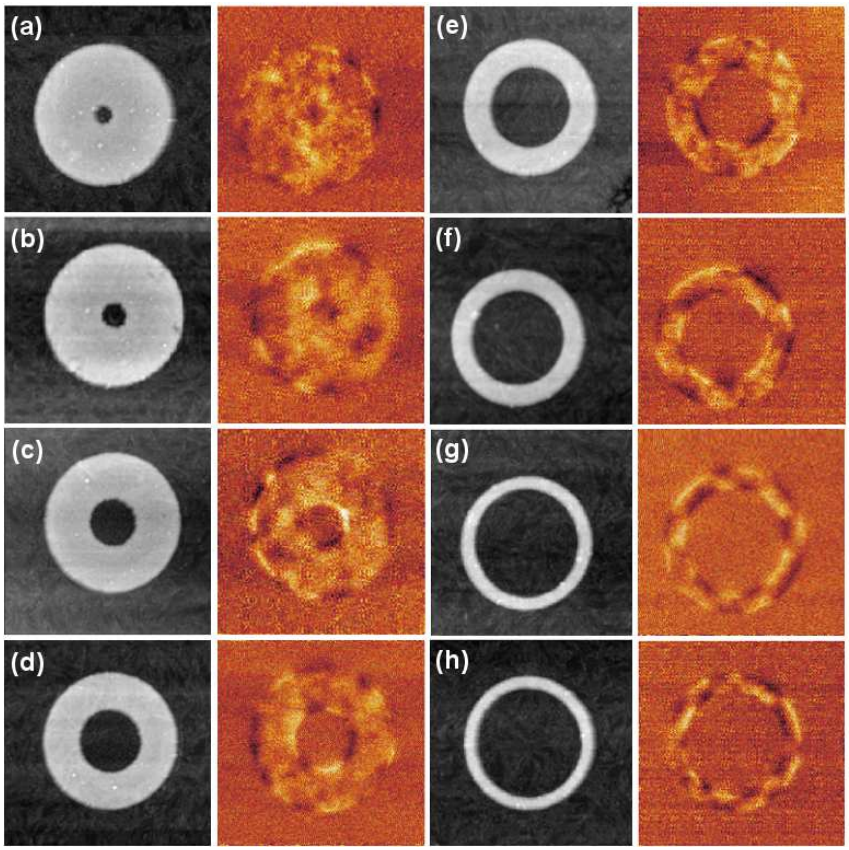

Figure 69: MFM images in remanence of Cu/Ni/Cu rings with $3\mu m$ external diameter. Different widths are shown: (a) 1300, (b) 1200, (c) 1000, (d) 800, (e) 550, (f) 430, (g) 280 and (h) 250 nm. AFM images are shown for each ring. A transverse magnetization component is observed in all cases. For wider rings the transverse domains are reveled on the outer radius and as the width is reducing, these domains are present on the inner radius too. As the width is decreasing the transverse magnetization is favored being the strongest component for rings with $\omega \approx D$.

field where the net ring magnetization is zero there is certain stability for that magnetic domain configuration. For H = 210 Oe, the area corresponding to domains with the same polarity that H increases and at 400 Oe extend over the whole ring. We note that the polarity of the contrast of the ring changes from bright-dark to dark-bright changing the field polarity, suggesting the tip magnetization is perpendicular to H and has an magnetic anisotropy value large enough to avoid a demagnetization of the M tip. Decreasing the field there a enhanced contrast along a <110> directions, for the images taken at H = -50 Oe and 0 Oe the [100], with a tend to nucleate domains along the $[\bar{1}10]$ the inversion process of M.

The thickness at which the internal domain structure vanish is in range

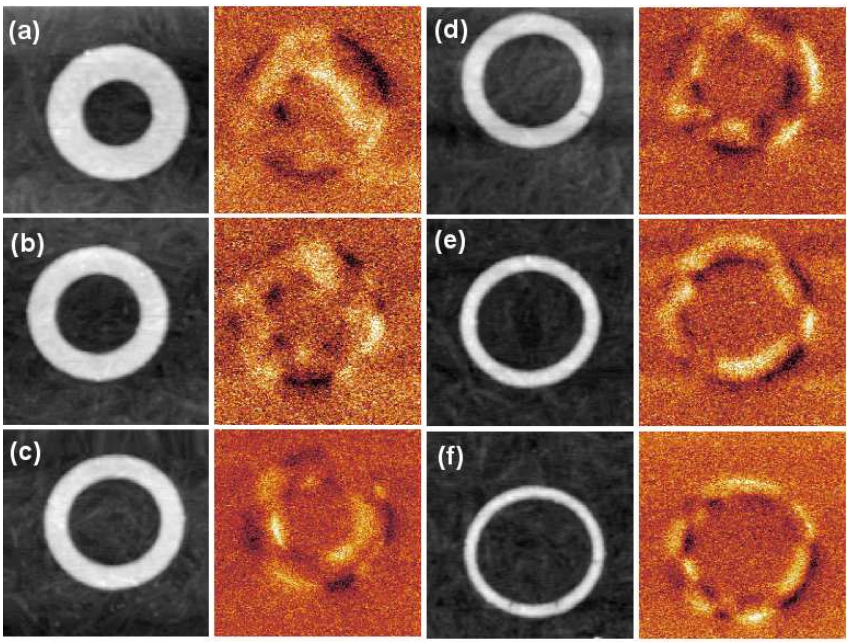

Figure 70: Topographic and magnetic images of Cu/Ni/Cu rings. The sample was image in remanence state after saturate with an out-of-the-plane applied magnetic field. The external diameter is 2 μm and the widths are (a) 460, (b) 380, (c) 320, (d) 270, (e) 210 and (f) 150 nm. Note that in all cases the magnetic signal is bigger than the topographic one. A transverse magnetization is observed is most of the widths. In the wider rings transverse domains are reveled on the outer radius as well as a internal domain structure that is not well defined. On the other hand, when ω is decreasing a transverse magnetization is favored with dark and bright alternating contrast along the ring distributed in such a way to reduce the magnetostatic energy.

between 400 nm to 300 nm. A value related to the domain width measured for unpatterned film. This fact suggest that below a critical width there is no room to the coexistence domain walls separating areas with different magnetization and the magnetization orientation nucleated at the edges is the dominant effect on the ring. Thus, assuming that the creation of a DW wall requires ≈ 2 times the size of the stripe in thin films, 2 x 200 nm = 400 nm, rings with W below that value should display, as is observed, a single domain structure along the radial direction. We also note that, although the MFM usually is not a quantitative technique it is observed by calculation of the stray field H_z, see Fig. 72, that a domain structure including domains with M perpendicular to the plane gives rises to a H_z more located at the magnetic area compared with a configuration with **M** in the film plane, as is observed comparing magnetic and topographic images.

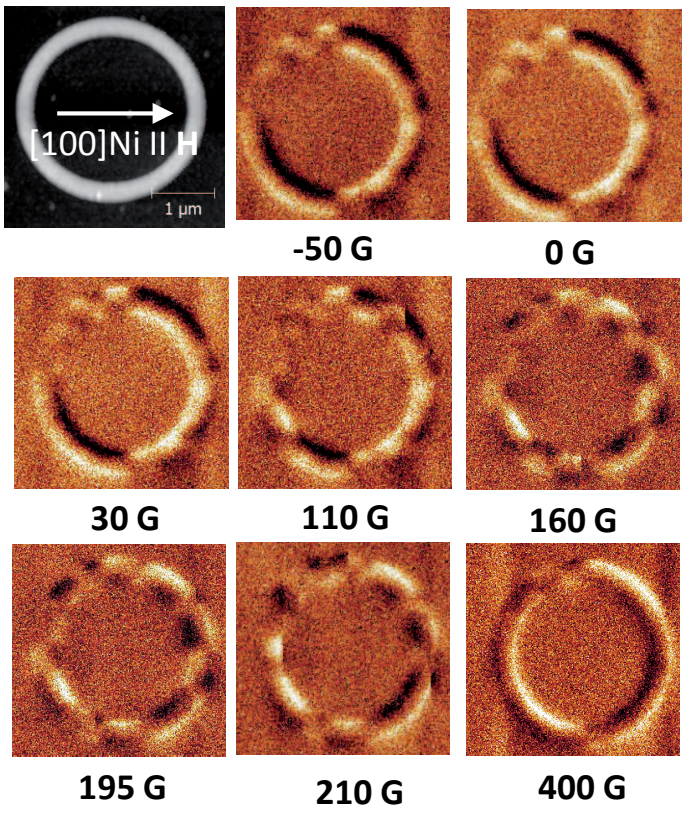

Figure 71: Images of the domain structure during the magnetization process in ring with D=3 μm and W = 200 nm. The field was applied along the Cu [001] in plane direction and the images were taken after saturation.

ANALYSIS

To elucidate the orientation of **M** we consider the energy contributions that play a role in the energy balance between the states with **M** lying along the radius or circumferentially. We analyze the magnetoelastic, the magnetostatic and the magnetocrystalline contributions to the total density energy as a function of the azimuthal angle ϕ and calculated the difference in energy between the state with **M** tangential to the ring minus the state with **M** along the radial direction $\Delta e_{anis}(\phi)$. The ring would exhibit magnetization along the radial direction if $\Delta e_{anis}(\phi) < 0$.

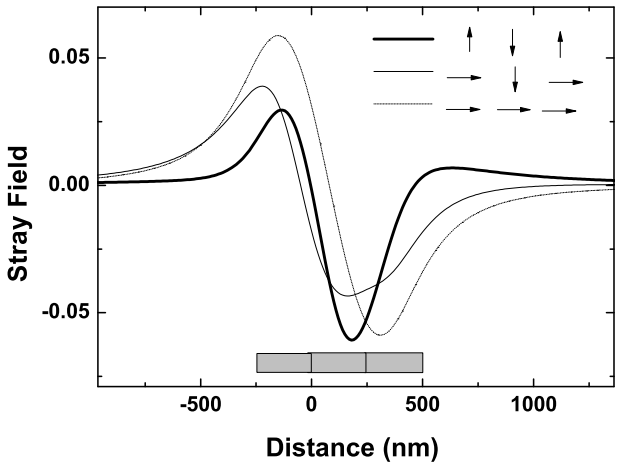

Figure 72: Stray field calculated for a segment formed by different combinations of in-plane and perpendicular domains that generate a field with qualitatively the same shape.

Magnetoelastic Energy

Previous works [22, 23] suggest the important role of the ME energy in determining the magnetic configuration in nanowires because of the presence of residual strain in the wires. We note that for Cu/Ni/Cu nanowires the sign of the anisotropic strain relaxation in combination with the sign of the ME stress coefficients favor a transverse ME anisotropy [22]. Here we analyze the ME contribution for a ring with a line width of 250 nm assuming an averaged in-plane anisotropic strain value comparable to that measured for an array of nanowires with similar film thickness and wire line width.

The general theory for the ME effects [24, 25] expresses the ME density of energy e_{mel} of the undistorted crystal as a series of products of tensor strain components and polynomials of the direction cosines of the magnetization related to the coordinate axes. For the Cartesian coordinate system e_{mel} can be written as:

$$\begin{aligned} e_{mel} &= B^{\gamma,2}\left[\left(\alpha_z^2-\frac{1}{3}\right)\left(\epsilon_{zz}-\frac{\epsilon_{xx}+\epsilon_{yy}}{2}\right)\right. \\ &+ \left.\frac{1}{2}\left(\alpha_x^2-\alpha_y^2\right)\left(\epsilon_{xx}-\epsilon_{yy}\right)\right] \\ &+ 2B^{\epsilon,2}\left(\alpha_x\alpha_y\epsilon_{xy}+\alpha_y\alpha_z\epsilon_{yz}+\alpha_z\alpha_x\epsilon_{zx}\right) \end{aligned} \quad (21)$$

The number of independent first-order ME coefficients is reduced to two ($B^{\gamma,2}$ and $B^{\epsilon,2}$ that correspond to the usual B_1 and B_2 ME coefficients [21]).

From Eq. (21) it can be deduced that different lattice deformations produce different magnetization states that are governed by the same ME coefficient. Thus, for the γ-terms, inside each square bracket strain polynomials proportional to $\alpha_z^2 - 1/3$ correspond to a tetragonal distortion $(a,a,a)\rightarrow(c,a',a')$ that induces a change in the orientation of the perpendicular component of $\mathbf{M}$, while the second strain terms, which are multiplied by $\alpha_x^2 - \alpha_y^2$, describe the contribution due to the breaking of the in-plane symmetry $(a,a)\rightarrow(a',b')$. The last contribution is fundamental in nanowires since the isotropic in-plane strain is broken by the patterning process.

It is more appropriate to describe the problem in the cylindrical coordinate system because it reflects the symmetry of the ring. The strain tensor components in the cylindrical reference basis can be obtained by performing the tensorial transformation for 2nd order tensors: $\epsilon_{ij} = a_{ik}\epsilon_{kl}a_{lj}$ where the subscripts stand for the tensor coordinates; i,j are assigned to Cartesian components (x, y, z) and k,l to the cylindrical system (r, ϕ, z). The a's correspond to the transformation tensor: $a_{11} = a_{22} = cos\phi$, $a_{12} = -sin\phi$, $a_{21} = sin\phi$, $a_{33} = 1$, $a_{13} = a_{31} = a_{23} = a_{32} = 0$, therefore:

$$\begin{aligned}
\epsilon_{xx} &= \epsilon_{rr}cos^2\phi + \epsilon_{\phi\phi}sin^2\phi - \epsilon_{r\phi}sin2\phi \\
\epsilon_{yy} &= \epsilon_{rr}sin^2\phi + \epsilon_{\phi\phi}cos^2\phi + \epsilon_{r\phi}sin2\phi \\
\epsilon_{zz} &= \epsilon_{zz} \\
\epsilon_{xy} &= (\epsilon_{rr} - \epsilon_{\phi\phi})\, sin\phi cos\phi + \epsilon_{r\phi}\left(cos^2\phi - cos^2\phi\right) \\
\epsilon_{yz} &= \epsilon_{rz}cos\phi - \epsilon_{\phi z}sin\phi \\
\epsilon_{zx} &= \epsilon_{rz}sin\phi + \epsilon_{\phi z}cos\phi
\end{aligned} \tag{22}$$

and for the cosines of the magnetization:

$$\begin{aligned}
\alpha_x &= \alpha_r cos\phi - \alpha_\phi sin\phi \\
\alpha_y &= \alpha_r sin\phi + \alpha_\phi cos\phi \\
\alpha_z &= \alpha_z
\end{aligned} \tag{23}$$

obtaining for e_{mel}

$$\begin{aligned} e_{mel} &= B_1 \left\{ \left(\alpha_z^2 - \frac{1}{3} \right) \left(\epsilon_{zz} - \frac{\epsilon_{rr} + \epsilon_{\phi\phi}}{2} \right) \right. \\ &+ \frac{1}{2} \left[\left(\alpha_r^2 - \alpha_\phi^2 \right) cos2\phi - 2\alpha_r \alpha_\phi sin2\phi \right] \\ &\left. \times \left[\left(\epsilon_{rr} - \epsilon_{\phi\phi} \right) cos2\phi - 2\epsilon_{r\phi} sin2\phi \right] \right\} \\ &+ 2B_2 \left\{ \left[\frac{1}{2} sin2\phi \left(\alpha_r^2 - \alpha_\phi^2 \right) + cos^2\phi \alpha_r \alpha_\phi \right] \right. \\ &\times \left[\frac{1}{2} \left(\epsilon_{rr} - \epsilon_{\phi\phi} \right) sin2\phi + \epsilon_{r\phi} cos2\phi \right] \\ &+ \epsilon_{rz} \left[\alpha_r sin2\phi + \alpha_\phi cos2\phi \right] \alpha_z \\ &\left. + \epsilon_{\phi z} \left[\alpha_r cos2\phi - \alpha_\phi sin2\phi \right] \alpha_z \right\} \end{aligned} \tag{24}$$

Therefore the difference in e_{mel} if $\mathbf{M}$ is tangent to the ring (α_r=0, α_ϕ=1) and aligned along the radius (α_r=1, α_ϕ=0) is :

$$\Delta e_{mel} = - \left(B_1 cos^2 2\phi + B_2 sin^2 2\phi \right) \left(\epsilon_{rr} - \epsilon_{\phi\phi} \right) \tag{25}$$

The magnitude of this contribution depends on the existence of an inequality between the radial ϵ_{rr} and the tangential strain $\epsilon_{\phi\phi}$. Notice that we have assumed that the shear strains are negligible. The presence of a combination of the two ME stresses multiplying the strain polynomial in Eq.(25) complicates the variation of the sign of this contribution with ϕ. This function oscillates between the values of B_1 and B_2 every $\pi/2$ and, thus, if the sign of the $B's$ is different, the sign of the ME contribution to Δe_{mel} would oscillate with ϕ. For nickel both ME stress coefficients are positive and the sign of angular dependence of Δe_{mel} does not change with ϕ, see Fig. 74.

Magnetostatic Energy

For the sake of simplicity we consider the case of a uniformly magnetized ring to estimate the magnetostatic energy e_{ms} because the calculation of the expression including the dependence of M with ϕ is extremely complicated and the uniform $\mathbf{M}$ case provides a simple analytical expression to calculate an upper limit to e_{ms}. That expression is given by $e_{ms} = D_{xx} \mu_o {M_s}^2/2$, where D_{xx} is he demagnetization factor for a ring with M along a fixed direction [16]:

$$\begin{aligned} D_{xx} = \frac{d}{2\pi(1-r)} \left[ln(8/d) - \frac{1}{2} + \frac{r}{r+1} ln(r) \right. \\ \left. -2\frac{1+r^2}{(1+r)^2} F\left(2\sqrt{\frac{r}{(1+r)}} \right) + 2E\left(2\sqrt{\frac{r}{(1+r)}} \right) \right] \end{aligned} \tag{26}$$

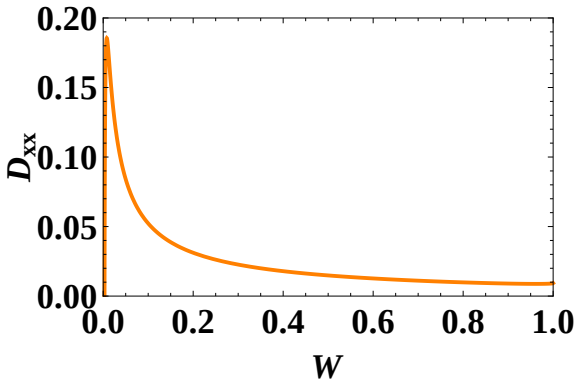

Figure 73: Calculation of the reduced demagnetization energy for D = 3 μm as a function of normalized ring line width.

here, D_{xx} defines the demagnetization factor for rings of outer radius R_o and line width ω with $t_{Ni} \ll \omega$, being $d = t_{Ni}/R_o$, $1 - r = \omega/R_o = W$ and, F and E are complete elliptic functions of the first and second kind, respectively. Fig. 73 shows the numerical solution of Eq. (26) for rings with R_0= 3 μm. Thus, if $\omega = 250nm$, D_{xx}= 0.036, and e_{ms}= 5.4 kJ/m^3.

There are no magnetic poles for a vortex state (α_r=0, α_ϕ=1) and the magnetostatic energy is zero, therefore Δe_{ms} takes the upper limit value of 5.4 kJ/m^3.

Magnetocrystalline Energy

The magnetocrystalline anisotropy for cubic crystals for the lowest order is expressed as: $e_{mc} = K_1(\alpha_x{}^2\alpha_y{}^2 + \alpha_y{}^2\alpha_z{}^2 + \alpha_z{}^2\alpha_x{}^2)$, becoming:

$$e_{mc} = K_1 \left[(\alpha_r cos\phi - \alpha_\phi sin\phi)^2(\alpha_r sin\phi + \alpha_\phi cos\phi)^2\right], \tag{27}$$

in cylindrical coordinates, using the Eqs.(23). From the point of view of the magnetocrystalline energy, there is a cost of keeping **M** along the radial direction that depends on ϕ and can be evaluated by putting α_r=1, α_ϕ=0 in Eq(27).

$$\Delta e_{mc} = \frac{1}{4}K_1 \left[1 - sin^2 2\phi\right] \tag{28}$$

Notice that this cost is zero for $\phi = \pi/4$ and maximum ($K_1/4$) for $\phi = 0$.

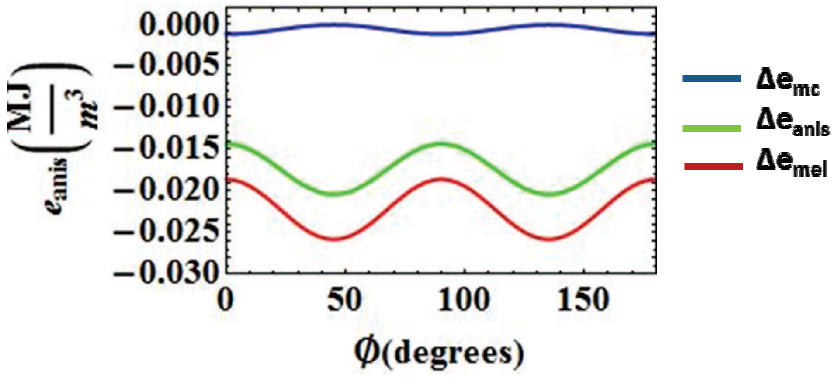

Figure 74: Angular dependence of $\Delta e_{anis}(\phi)$ for a ring with 3 μm diameter, ω= 250 nm width, and ϵ of 0.003. The $\Delta e(\phi)_{mel}$, $\Delta e(\phi)_{mc}$ and $\Delta e(\phi)_{ms}$ are also shown

DISCUSSION

The energy balance $\Delta e_{anis}(\phi)$ for a ring with ω = 250 nm and an averaged $(\epsilon_{rr} - \epsilon_{\phi\phi})$ of 0.003, a value in the range of the experimental data measured for wires with similar width and Ni thickness, is displayed in fig 74, taking B_1 = 6.9 MPa, B_2 = 8.9 MPa [26] and $K_1 = -4.5 \times 10^3 J/m^3$. $\Delta e_{anis}(\phi)$ is negative independently of ϕ, meaning that the radial orientation of **M** is favored over the tangential direction for the complete ring. It can be observed that $\Delta e_{mel}(\phi)$ is the largest contribution to $\Delta e_{anis}(\phi)$. The calculations show $\Delta e_{anis}(\phi)$ is kept at negative values even if $(\epsilon_{rr} - \epsilon_{\phi\phi})$ decreases to values as low as 0.001. Therefore the radial orientation of **M** observed in epitaxial rings can be attributed to the ME contribution.

Finite elements analysis

Now we discuss the profile of the micromagnetic structure of the thicker rings. We note that an anisotropy in the relaxation of the isotropic in plane strain of Ni film ($\approx 0.75\%$ for the film) is required to justify the radial anisotropy term. Also, the observation of a domain structure different inside the ring than at its edges suggest that $(\epsilon_{rr} - \epsilon_{\phi\phi})$ can change along the ring. To analyze this fact finite element analysis is carried out for the estimation of a strain relaxation in the trilayer Cu/Ni/Cu structure for rings with D and W parameters based on the initial stress of 1.95 GPa for the unpatterned Cu/Ni/Cu structure. The stress is introduced by setting the Ni layer to a a temperature at which the thermal expansion of nickel with respect to the copper is equivalent to the experimental in-plane strain. An example of the stress distribution for a ring with D = 1 μm and W = 500 nm is shown in Fig. 75. The image shows,

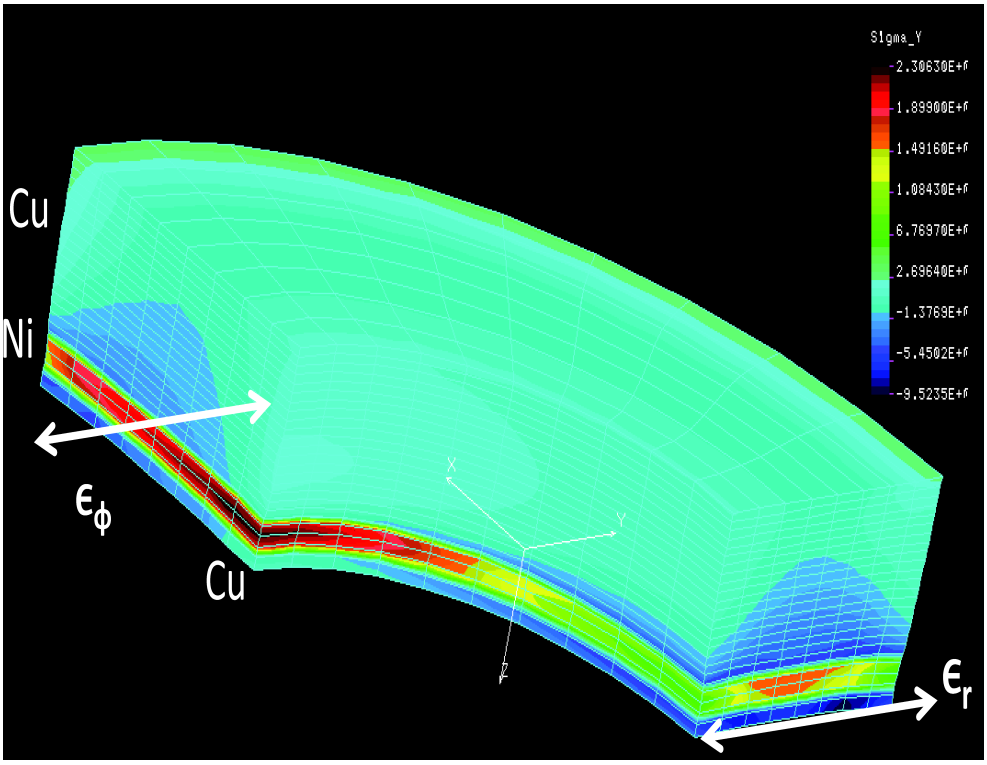

Figure 75: Snapshot of the finite element calculation of the σ_{xx} for a Cu(5)/Ni(14)/Cu(100) trilayer.

for a ring quarter, the stress along the x Cartesian coordinate, therefore it corresponds to the radial stress along the x axis and the tangential stress for the y axis. From the graph straightforward conclusions are observed: a) σ_{rr} is more relaxed at the edges of the ring that at the center; b) the $\sigma_{\phi\phi}$ is quite uniform although there is a slight relaxation a the inner ring area. As a result, the calculated $(\epsilon_{rr} - \epsilon_{\phi\phi})$ is maximum at the edges and minimum at the ring center. This strain dependence can be related to the dependence of the domain structure: transverse for edge areas closer to the ring edges and similar to the unpattern film for the inner area of the ring where, locally the strain relaxation is smaller and therefore $(\epsilon_{rr} - \epsilon_{\phi\phi}) \approx 0$ and the tetragonal distortion $[\epsilon_z - (1/2)(\epsilon_{rr} + \epsilon_{\phi\phi})]$ remains with a value comparable to the film value.

CONCLUSIONS

This work shows the relevance of the ME interaction in the control of the magnetic state in nanomagnets. For example, magnetic circuits made on epitaxial layers will include nanowires with the axes along different crystallographic directions, connected with circular segments. The orientation of the magnetization of those elements can be chosen through the election of the sign for the ME stress coefficients. Thus, materials with different sign of the B offer the possibility of combining elements with these transverse magnetic orientations with the usual longitudinal orientation of M enabling new configurations of domain walls to be created.

Epitaxial ring of Cu/Ni/Cu has been fabricated by e-beam and focused ion beam techniques is range of thicknesses where the effective magnetic anisotropy in the unpatterned film is ≈ 0. The micromagnetic structure show an unusual orientation of the magnetization along the radial direction of the ring. This effect is explained due to the ME anisotropy generated by an anisotropic relaxation of the epitaxial strain observed in the continuous film.

References V

[1] Liao, Zhi-Min and Wu, Han-Chun and Fu, Qiang and Fu, Xuewen and Zhu, Xinli and Xu, Jun and Shvets, Igor V. and Zhang, Zhuhua and Guo, Wanlin and Leprince-Wang, Yamin and Zhao, Qing and Wu, Xiaosong and Yu, a-Peng, Sci. Rep. **2**, 452 (2012).

[2] X. Marti, I. Fina, V. Skumryev, C. Ferrater, M. Varela, L. Fabrega, F. Sanchez, and J. Fontcuberta, Appl. Phys. Lett. **95**, 142903 (2009).

[3] S. Trommler, R. H¨uhne, K. Iida, P. Pahlke, S. Haindl, L. Schultz, and B. Holzapfel, New J. Phys. **12**, 103030 (2010).

[4] R. S. Beach, J. A. Borchers, A. Matheny, R. W. Erwin, M. B. Salamon, B. Everitt, K. Pettit, J. J. Rhyne, and C. P. Flynn, Phys. Rev. Lett. **70**, 3502 (1993).

[5] R. Jungblut, M. T. Johnson, J. aan de Stegge, A. Reinders, and F. J. A. den Broeder, J. Appl. Phys. **75**, 6424 (1994).

[6] B. Schulz and K. Baberschke, Phys. Rev. B **50**, 13467 (1994).

[7] F. Huang, M. T. Kief, G. J. Mankey, and R. F. Willis, Phys. Rev. B **49**, 3962 (1994).

[8] G. Bochi, C. A. Ballentine, H. E. Inglefield, C. V. Thompson, R. C. O'Handley, H. J. Hug, B. Stiefel, A. Moser, and H.-J. G¨untherodt, Phys. Rev. B **52**, 7311 (1995).

[9] K. Ha and R. C. O'Handley, J. Appl. Phys. **85**, 5282 (1999).

[10] A. Murayama, K. Hyomi, J. Eickmann, and C. M. Falco, Phys. Rev. B **60**, 15245 (1999).

[11] M. Ciria, K. Ha, D. Bono, and R. C. O'Handley, J. Appl. Phys. **91**, 8150 (2002).

[12] L. Benito, J. I. Arnaudas, M. Ciria, C. de la Fuente, A. del Moral, R. C. C. Ward, and M. R. Wells, Phys. Rev. B **70**, 052403 (2004).

[13] K. Ha, M. Ciria, R. C. O'Handley, P. W. Stephens, and S. Pagola, Phys. Rev. B **60**, 13780 (1999).

[14] S. S. P. Parkin, M. Hayashi, and L. Thomas, Science **320**, 190 (2008).

[15] D. A. Allwood, G. Xiong, C. C. Faulkner, D. Atkinson, D. Petit, and R. P. Cowburn, Science **309**, 1688 (2005).

[16] C. A. F. Vaz, C. Athanasiou, J. A. C. Bland, and G. Rowlands, Phys. Rev. B **73**, 054411 (2006).

[17] C. A. Ross, F. J. Castano, D. Morecroft, W. Jung, H. I. Smith, T. A. Moore, T. J. Hayward, J. A. C. Bland, T. J. Bromwich, and A. K. Petford-Long, J. Appl. Phys. **99**, 08S501 (2006).

[18] D. Ravelosona, D. Lacour, J. A. Katine, B. D. Terris, and C. Chappert, Phys. Rev. Lett. **95**, 117203 (2005).

[19] S.-W. Jung, W. Kim, T.-D. Lee, K.-J. Lee, and H.-W. Lee, Appl. Phys. Lett. **92**, 202508 (2008).

[20] S. Hameed, P. Talagala, R. Naik, L. E. Wenger, V. M. Naik, and R. Proksch, Phys. Rev. B **64**, 184406 (2001).

[21] R. C. O'Handley, Modern Magnetic Materials: Principles and Applications (John Wiley Sons, 2000).

[22] M. Ciria, F. J. Castaño, J. L. Diez-Ferrer, J. I. Arnaudas, B. G. Ng, R. C. O'Handley, and C. A. Ross, Phys. Rev. B **80**, 094417 (2009).

[23] D. Navas, C. Nam, D. Velazquez, and C. A. Ross, Phys. Rev. B **81**, 224439 (2010).

[24] E. Callen and H. B. Callen, Phys. Rev. **139**, A455 (1965).

[25] J. Rouchy and E. du Tremolet de Lacheisserie, Z. Physik B **36**, 67 (1979).

[26] E. W. Lee and M. A. Asgar, Proc. R. Soc. A **326**, 73 (1971).